University of Trieste

DEPARTMENT OF PHYSICS
Ph.D. degree in Physics

Simulation analysis: from Planck calibration towards an end-to-end simulator for instrument operations applied to the Euclid mission

Candidate:
Erik Romelli
Matricola PHD0400004

Supervisor:
Dott.sa Anna Gregorio

Tutor:
Dott. Michele Maris

Coordinator

XXIX Cycle

Clara sometimes asks me if I dream. "Of course I dream!", I tell her, "Everybody dreams". "But what do you dream about?", she'll ask. "The same thing everybody dreams about", I tell her. "I dream about where I'm going.". She always laughs at that. "But you're not going anywhere, you're just wandering about.". That's not true. Not anymore. I have a new destination. My journey is the same as yours, the same as anyone's. It's taken me so many years, so many lifetimes, but at last I know where I'm going. Where I've always been going. Home. The long way around.

The Day of the Doctor

Contents

Introduction

The Ph.D. project described in this work is based on two main activities. The first one is the analysis of Jupiter flux time-lines aimed at the inter-calibration between the Planck and WMAP mission, to properly calibrate the beam pattern and to study Jupiter atmosphere. The second is the implementation of a prototype end-to-end simulator, using the Euclid mission as a test case, designed to assess mission performance and support instrument operations.

The spectral energy distribution (SED) at millimetric wavelengths of planets is an important benchmark to inter-calibrate different CMB experiments, to properly calibrate the beam pattern and it is a source of information on the atmospheric structure of those bodies. Despite their importance, there is a lack of very accurate measures of SED for those bodies. Planck observed Mars, Jupiter, Saturn, Uranus and Neptune from three to eight times during the mission. In particular, Planck furnished a good measurement of the brightness temperature for Jupiter, with an accuracy better than half a percent. Jupiter flux analysis not only improved the SED results previously quoted in literature, but was also part of the Planck/LFI pipeline, due to its importance for the detector beam reconstruction and for the inter-calibration between Planck itself and its predecessor WMAP.

The analysis gives continuity to my involvement in the Planck LFI Data Processing Center (DPC) activities, and in general in the Planck mission, started during my MSc thesis [1]. This work, which contributed to Planck/LFI calibration activities and is reported in the Planck 2015 LFI Calibration Paper, concluded at the beginning of my second year of Ph.D. Since the Planck mission was at its conclusion as foreseen, I migrated to the Euclid mission which is still in its pre launch phases. The second part of my Ph.D. is aimed at developing a prototype of an End-to-End Simulator for the Euclid Mission.

End-to-End mission performance Simulators (E2ES) enable the generation of simulated output data for selected test scenarios to support the assessment of the mission performance. I have been involved in the design of a reference architecture of an E2ES aimed at supporting instrument operations and in the development of a prototype, providing basic functionalities. The Euclid Mission has been selected as test case.

The work is structured as follows: in Chapter 1 a brief introduction to Cosmology is given, with particuar attection to the cosmological probes which will be investigated by Euclid. Chapter 2 introduces the Euclid mission and its predecessors Herschel and Planck. Chapter 3 is focused on Jupiter flux analysis, while Chapter 4 gives an overview of E2E simulators requirements and characteristics. Chapter 5 describes the implemented prototype and its preliminary results, while Chapter 6 is focused on tests and further development of the prototype itself.

Chapter 1

Cosmological Probes

Over the past century, our view of the Universe has changed dramatically. Starting from the beginning of the 20th century, the formulation of Einstein's General Relativity, the discovery of the expansion of the Universe and the subsequent realisation that the Universe is very old, but had a beginning, are major triumphs, from the point of view of astrophysics, that have changed our view of humanity's place in the Universe. At the turn of the Millennium, further crucial observational progress, especially from space-based experiments, led to the emergence of the concordance cosmological model. This provides a remarkably accurate description of a wide range of independent observations through a fully self-consistent theoretical framework with a small number of parameters. However, it relies on two untested assumptions about the initial conditions of the Universe and the nature of gravity itself, as well as the existence of two dominant components whose nature is entirely unknown.

1.1 The ΛCDM model

Our understanding of Cosmology is that of a Universe evolving from a homogeneous state after the Big Bang to a hierarchical assembly of structures (galaxies, clusters and super-clusters) at our epoch. This view relies on two untested assumptions:

- The large scale Universe, *i.e.* on scales such that local fluctuations are negligible, is on average homogeneous and isotropic and has expanded in a near homogeneous way from a state of extremely high density and temperature;
- General Relativity (GR) is the correct theory of gravity on cosmological scales.

Starting from these assumptions, the ΛCDM (Lambda-Cold Dark Matter) model is the simplest parametrization of Big Bang cosmology. In this picture, the Universe contains a cosmological constant Λ, associated to Dark Energy (DE), and Cold Dark Matter (CDM). This model reasonably explains different observational evidences:

- The existence of the Cosmic Microwave Background (CMB) and the structure of its anisotropies;
- The large-scale structure in the distribution of galaxies;
- The abundances of light elements: H, D, He and Li;
- The accelerating expansion of the Universe, observing distant galaxies and supernovae.

In the ΛCDM model, the cosmological scenario of our Universe can be explained using only six indipendent parameters: the Hubble constant at present day[1] (H_0), the optical depth at reionization epoch (τ), the critical density of matter (Ω_M, considering both baryons and DM) and baryons (Ω_b), the primordial amplitude and spectral index of scalar perturbation (A_s and n_s). In Table 1.1 a summary of the independent parameters of ΛCDM model is reported. The values represent the most recent measure by the Planck space mission [2]. A brief description of each parameter follows.

Table 1.1: Cosmological parameters as measured by the Planck mission.

Parameter	**Value from Planck**	**Description**
H_0	67.8 ± 0.9	Hubble constant
τ	0.066 ± 0.016	Reionization optical depth
$\Omega_M h^2$	0.1415 ± 0.0019	Matter density (DM + baryons)
$\Omega_b h^2$	0.02226 ± 0.00023	Baryon density
n_s	0.9677 ± 0.006	Spectral index
$\ln(10^{10} A_s)$	3.062 ± 0.029	Primordial spectrum

Hubble constant: H_0

The Hubble constant describes the expansion rate of the Universe. The parameter is named after Edwin Hubble, who in 1929 observed a direct correlation between the proper distance to a galaxy and its recessional velocity. The so called Hubble law can be expressed as:

$$v = H_0 d \tag{1.1}$$

The Hubble constant can be used to estimate the age of the Universe via the Hubble time, which is the inverse of the Hubble constant:

$$t = \frac{1}{H_0} \tag{1.2}$$

The Hubble constant H_0 represents the present value or the so called Hubble parameter H, whose value is time dependent and can be expressed in terms of the expansion scale factor of the Universe.

Optical depth at reionization: τ

Reionization is the second of two major phase transitions of baryonic matter in the Universe.

[1] Quantities that depend on the value of H_0 are often expressed in terms of h, related to the Hubble constant by: $h = H_0/100$ kms^{-1}Mpc.

The first phase transition is recombination, nearly 380000 years after the Big Bang, when, due to the cooling of the Universe, the rate of recombination of electrons and protons to form neutral light elements (H, D, He and Li) becomes higher than the reionization rate. Before recombination, the Universe is opaque due to Thomson scattering of photons on free electrons, but it becomes increasingly transparent as more electrons and protons combines to form neutral atoms.

The second phase change occurs once structures start to collapse in the early Universe. As these structures form and start to radiate, hydrogen in the Universe reverts from being neutral, to once again being ionized. The parameter τ represents the Thomson scattering optical depth at reionization and is used to infer the epoch at which reionization occures.

Matter and baryon critical density: Ω_M and Ω_b

An important cosmological parameter is the density parameter Ω, which is used to express the density ρ of the Universe as a function of the critical density ρ_c:

$$\Omega = \frac{\rho}{\rho_c} \tag{1.3}$$

with the critical density, derived from Friedman equations, being:

$$\rho_c = \frac{3H^2}{8\pi G} \tag{1.4}$$

where G is the gravitational constant. As we can note, ρ_c depends on the Hubble parameter H, which means a time dependency. Since in the Universe we have different density contributions we can define a specific density parameter for each component. In this picture we consider the matter mass-energy density parameter Ω_M and the baryon density parameter Ω_b.

Spectral index and primordial spectral amplitude: n_s and A_s

In cosmology the evolution of structures is studied as the evolution of local density perturbations $\delta(\mathbf{x})$ in a homogenous and isotropic background, which has the mean density of the Universe $\overline{\rho}$, defined as:

$$\delta(\mathbf{x}) = \frac{\rho(\mathbf{x}) - \overline{\rho}}{\overline{\rho}} \tag{1.5}$$

We can imagine this perturbation as a superposition of plane waves which have the advantage that each wave evolves independently from the others[2].

[2]This is true until the evolution of density perturbations is linear, *i.e.* until $\delta < 1$.

This effectively means that we can represent the distribution as independent components in reciprocal space, in terms of the wavevector of each component $\mathbf{k}$ [3]:

$$\delta(\mathbf{x}) = \frac{1}{(2\pi)^3} \int \tilde{\delta}_{\mathbf{k}} e^{-i\mathbf{x}\cdot\mathbf{k}} d\mathbf{x} \tag{1.6}$$

It can be demonstrated that if the density perturbations are random Gaussian distributed [4], as the inflation model suggests, we can infer the statistical properties of the density perturbation field from its *power spectrum*:

$$P(\mathbf{k}) \equiv \langle |\tilde{\delta}_{\mathbf{k}}|^2 \rangle \tag{1.7}$$

The power spectrum $P(\mathbf{k})$ is commonly cast in the following form:

$$P(k) = A_s \left(\frac{k}{k_0} \right)^{n_s} - 1 \tag{1.8}$$

where A_s and n_s are respectively the amplitude and the spectral index of the power spectrum, while k_0 is a reference scale. If primordial perturbations are produced by inflation, the measure of A_s and n_s can constrain the inflationary model [5].

From the six parameters briefly discussed in this section, we can infer all the information on the composition, the origin and the evolution of our Universe. The most precise measure of the cosmological parameters of the ΛCDM model has been provided by the Planck space mission [2]. Planck observed the Cosmic Microwave Background (CMB) anisotropies during more than four years from May 2009 to October 2013, with an unprecedented combination of sensitivity, angular resolution and frequency coverage (see Section 2.1.2). The CMB is the thermal radiation left over from the time of recombination and it is fundamental to observational cosmology because it is the oldest light in the universe, dating to the epoch of recombination. The CMB has a thermal blackbody spectrum at a temperature of approximately 2.72548 K [6]. Its spatial distribution on the whole sky is not completely isotropic but it shows small anisotropies on the order of $\sim 10^{-5}$ K on different angular scales [7]. The analysis of these temperature anisotropies allows us to obtain useful information on the cosmological parameters and the formation of structures.

Thanks to Planck and its predecessors, today we know that just a little fraction of the Universe, less than a 5%, is composed by baryonic matter. As illustrated in Figure 1.1, the Universe has two major components whose origin is mostly unkown: Dark Matter, representing the 26.8% of the total composition of the Universe, and Dark Energy, which is the 68.3%. In the following sections we are going to focus on DM and DE and on how the Euclid mission will try to enlight our knowledge of these dark components.

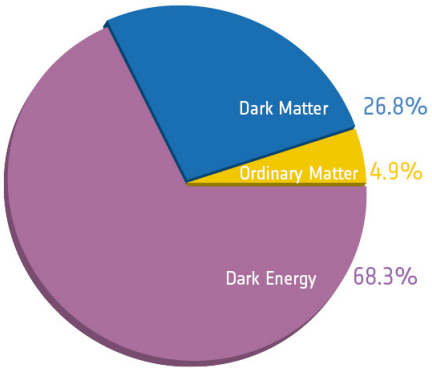

Figure 1.1: Pie chart of the composition of the Universe derived from Planck observations.
Source: http://spaceinimages.esa.int

1.2 Dark Matter

Of the two dark ingredients of the concordance model, DM is the most familiar. Evidence for its existence goes back to 1933, when Fritz Zwicky realised that the dynamical mass of the Coma cluster exceeded that expected from the luminosities of its member galaxies, suggesting a dominant non-luminous component. Later on, further support came from the measurements of flat rotation curves in spiral galaxies. In Figure 1.2 the discrepancy between observed galaxy rotation curves and the theoretical prediction, assuming a centrally dominated mass associated with the observed luminous material, is shown. The discrepancy between the two curves is explained assuming the existence of a dark matter halo surrounding the galaxy.

Similar studies have been made on the velocity dispersion of stellar population in elliptical galaxy or, equivalently, of galaxies in a cluster. These analyses allow us to infer the kinetic energy and, assuming the structure in viral equilibrium, the mass of the object. Comparing this to total luminosity allows us to make conclusions on the amount of DM in the structure.

Another evidence of DM existence comes from gravitational lensing. The detailed description of this phenomenon is left to Section 1.5, since it represents one of the main cosmological probes that Euclid will investigate. Gravitational lensing observation of the Bullet cluster, for instance, reveals separation of visible matter and DM halo, which were individually located using X-ray observations and lensing techniques. This is why the Bullet cluster is often cited as one of the best astrophysical evidences for DM existence and provides one of the best current evidence of its nature. Evidences from Bullet cluster observations, show that DM behaves as a collisionless fluid, *i.e.* a fluid in which interaction cross-section between particles is so low that collisions between particles have no significant effect on the system. The Bullet cluster is the result of a merging between two smaller clusters. As we can see in Figure 1.3, the gas component in this collision

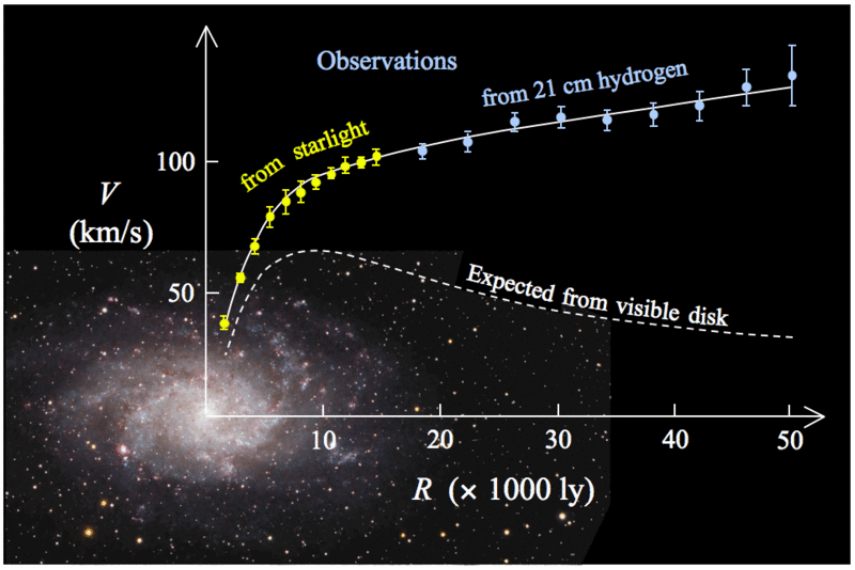

Figure 1.2: Rotation curve of the spiral galaxy M33 (yellow and blue points with errorbars) and the predicted one from distribution of the visible matter (white line).
Source: Corbelli and Salucci, 1999 [8].

Figure 1.3: Composite image of X-ray (pink) and weak gravitational lensing (blue) of the Bullet cluster.
Source: http://apod.nasa.gov

(in pink), made of collisional baryonic matter, was slowed by a drag force. In contrast, the DM component (in blue) was not slowed by the impact, because it does not interact directly with itself or the gas except through gravity.

A collisionless nature of DM is suggested also from a theoretical point of view. If we consider the Universe before the recombination epoch, what we have is a plasma in which photons and baryons are strongly coupled by Thomson scattering. The mean free path of a photon in such an environment is:

$$\lambda = \frac{1}{\sigma_T n_e} \tag{1.9}$$

with σ_T the Thomson cross section and n_e the electron number density of the plasma. Since $\lambda \neq 0$, photons can diffuse from high density to low density regions damping the perturbations in the photon-baryon plasma density distribution. Considering the motion of a photon to be a random walk with a mean step length λ, the mean number of steps a photon takes over a time t is $N = ct/\lambda$. It then follows from kinetic theory that:

$$\lambda_d = \left(\frac{N}{3}\right)^{\frac{1}{2}} \lambda \tag{1.10}$$

where λ_d is the scale at which the damping is important. From this damping length we can infer the minimum mass that a perturbation shall have to survive the damping:

$$M_d = \frac{\pi}{6}\overline{\rho}\lambda_d^3 \tag{1.11}$$

At recombination we obtain $M_d \sim 10^{12} M_\odot$ [4]. Any structure with a mass smaller than M_d cannot survive the damping at recombination and cannot be seen at present day. That means that at present day we should not be able to observe objects smaller than $\sim$ ten galaxies. This phenomenon is called *silk damping* and suggests us that we need something contributing to the gravity potential well to help the perturbations in their collapse; this contribution must come from a collisionless component in order not to be affected by the same damping.

A similar reasoning helps in understanding why the standard cosmological model assumes a cold DM component. Studying the dynamical evolution of a density perturbation of a collisionless fluid, we can find a certain length scale λ_{fs} under which each perturbation is damped. This effect, owing to the random motions of the collisionless particles, is called *free streaming* damping. What happens physically is that, because of their large random velocities and collisionless nature, particles diffuse, leading to damping of the density perturbations. The proper length scale below which free streaming damping becomes important is of the order vt, where t is the age of the Universe, and v is the typical particle velocity at t. In analogy at the silk damping, we can infer the mass at free streaming scale:

$$M_{fs} = \frac{\pi}{6}\overline{\rho}\lambda_{fs}^3 \tag{1.12}$$

The free streaming length scale depends on the velocity dispersion of the particle population. The higher the velocity dispersion, the greater its free streaming length. To have small structures surviving the free streaming damping we need particles with relatively low velocity dispersion. Since neutrinos are very weakly interacting and electrically neutral, one can assume (for the Occam's razor) that DM can be made by neutrinos alone. If we believe in this assumption, we obtain $M_{fs} \sim 10^{15} M_{\odot}$ [4], obtaining that the smallest possible structure that can survive the free streaming is of the order of a cluster of galaxies. To have a M_{fs} of the order of the mass of a galaxy, we need slower particles, with low kinetic energy, which means, in this sense, "cold". To reproduce the structures that we observe, our model must have a contribution of some kind of collisionless cold component, that we call Cold Dark Matter (CDM).

1.3 Dark Energy

Dark Energy is the second dark ingredient of the concordance cosmological model. As far as we know it is a component that is causing the expansion of the Universe to accelerate. It represents one of the biggest puzzles in modern physics because current theories cannot explain its magnitude or its origin. In the standard cosmological model, DE is associated with the cosmological constant Λ and can be interpreted as the vacuum energy of empty space. If this is the case, its observed value is not consistent with current theories: in the context of a quantum-field theory, the value of a cosmological constant should be, considering experimental bounds from particle physics, at least 10^{60} times larger than what observed [9]. This is the largest discrepancy between theory and observation ever encountered in modern physics. It implies that either the cosmological constant is not the correct description of DE or that we must consider a radical change in our most fundamental theories of physics, such as quantum mechanics and GR. Both these scenarios leave the possibility open for more exotic models.

The cosmological constant Λ was introduced for the first time by Einstein in 1917, as an additional component opposing to gravity in his field equation. Einstein's field equation:

$$R_{\mu\nu} - \frac{1}{2} g_{\mu\nu} R + \Lambda g_{\mu\nu} = \frac{8\pi G}{c^4} T_{\mu\nu} \tag{1.13}$$

tells us that changing the mass-energy density distribution of the universe, represented by the *stress-energy* tensor $T_{\mu\nu}$, affects the geometry of the Universe: its metric $g_{\mu\nu}$ and curvature Ricci $R_{\mu\nu}$ tensors[3]. The cosmological constant Λ enters as a component opposing gravity in order to obtain a static Universe solution. With Hubble's discovery of the expansion of the Universe, the assumption of a static Universe failed, and Λ seemed to be an unecessary term in the equation. In 1998, thanks to the Hubble Space Telescope (HST) observations, two independent projects, the *Supernova Cosmology Project*[4] and the *High-Z Supernova*

[3] In the equation R is the Ricci scalar curvature defined as the trace of the Ricci tensor.
[4] http://supernova.lbl.gov/

Search Team[5], simultaneously obtained results suggesting an acceleration in the expansion of the universe by using distant type Ia supernovae as standard candles (see Figure 1.4). This discover suggests the presence of some sort of component in the Universe which causes the acceleration. This component is commonly associated to the cosmological constant term in Einstein field equation.

The cosmological constant Λ has the same effect as an intrinsic energy density of the vacuum and can be associated to an energy density distribution ρ_Λ. Any component of our Universe is related to pressure thanks to the equation of state:

$$p = w\rho c^2 \tag{1.14}$$

where w is called Zel'dovich parameter. After some algebra, it can be shown that:

$$\rho \sim a^{-3(1+w)} \tag{1.15}$$

with a being the scale factor, relating the proper distance between a pair of objects in an expanding Universe. We know that $\rho_m \sim a^{-3}$ for non relativistic matter and $\rho_r \sim a^{-4}$ for relativistic matter and radiation. It follows that $w = 0$ and $w = 1/3$ for non relativistic matter and radiation respectively, accordingly to our knowledge of thermodynamics. A cosmological constant implies a constant density distribution, *i.e.* $\rho \sim a^0$, which means that $w = -1$. From the equation of state 1.14, we can see that the cosmological constant opposes the contribution of gravity, acting as a fluid with negative pressure. A pure cosmological constant contribution implies $w = -1$; any deviation from this value implies a dynamical DE contribution, as it is treated in Section 1.4

1.4 Key questions

Determining the nature of DE and DM represents a huge breakthrough in our understanding of the majority of the mass-energy content of the Universe. Substantial progress has been made by dedicated space missions, such as Planck, that have measured the CMB temperature fluctuations with high precision. This kind of measure represents, for istance, a formidable confirmation of the CDM scenario for structure formation. Unfortunately, a number of fundamental questions still remains unanswered. For example, the analysis of the relative heights of the peaks in CMB power spectrum rules out a baryonic origin for the DM, but cannot provide us more information about the nature of DM. Similarly, the CMB power spectrum provides strong evidence that DE exists, but it cannot tell us anything substantial on its actual nature.

In this scenario, the goal of Euclid is to try to deepen our knowledge about the nature of the dark components of the Universe, thanks to a unique combination

[5]https://www.cfa.harvard.edu/supernova/home.html

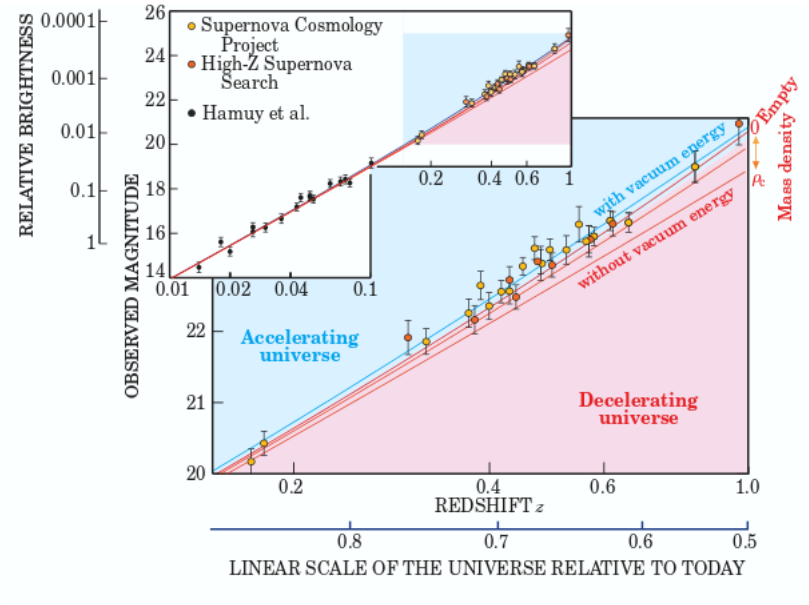

Figure 1.4: Data involve the measurement of the redshifts of the distant supernovae. The observed magnitudes are plotted against the redshift parameter z. Above $z \sim 0.1$ data start to diverge from the Hubble law, suggesting an acceleration in the expansion of the Universe.
Source: Perlmutter, 2003 [10]

of its two primary probes, namely weak gravitational lensing and Baryonic Acoustic Oscillations (see Section 1.5). This combination is not only meant to allow the experiment to reach unprecedented statistical precision, but provides a crucial crosscheck of systematic effects, which become dominant at these levels of sensitivity. The Euclid mission is oriented to address the following key questions about the dark side of the Universe:

- **Dynamical Dark Energy**: is DE simply a cosmological constant, or is it a field that evolves dynamically with the expansion of the Universe?
- **Modification of Gravity**: is the apparent acceleration a manifestation of a breakdown of GR on the largest scales, or a failure of the cosmological assumptions of homogeneity and isotropy?
- **Dark Matter**: what is DM? What constraints can we put on DM particle cross-section and mass?
- **Initial Conditions**: what is the power spectrum of primordial density fluctuations? Is our prediction of a Gaussian probability distribution of these fluctuation correct?

We now explain in more detail each of the primary science goals. The following explanation is summarised in Table 1.2.

Dynamical Dark Energy

As shown in section 1.3, a pure cosmological constant contribution can be characterized by an equation of state with Zel'dovich parameter $w = -1$. Any deviation from this value implies a dynamical evolution of the DE component. A key goal of Euclid is to place tight observational bounds on any such deviation. We can model the dynamical evolution of DE assuming a functional form for w as a function of the scale factor a. The functional form of $w(a)$ is unknown, but to first order it can be approximated by a constant term plus one that captures the dynamical nature of the dark energy:

$$w(a) = w_0 + w_a(a_0 - a) \tag{1.16}$$

Being $a_0 = 1$ at present day, equation 1.16 becomes: $w(a) = w_0 + w_a(1 - a)$. This parameterisation is commonly used to define the DE Figure of Merit (FoM) as the reciprocal ratio of the product of the 1 σ error on these parameters:

$$\text{FoM} = \frac{1}{\Delta w_0 \times \Delta w_a} \tag{1.17}$$

where a larger FoM implies a more precise measurement of the DE properties. The idea behind this kind of measure is to compare two models of DE: a cosmological constant and a model in which the two parameters w_0 and w_a vary within a reasonable range. For very small variations the cosmological constant model would be favoured, while for very large deviations the two-parameter model would be considered the most accurate description of DE behaviour. This is quantified using a Bayesian evidence calculation which shows that if the FoM ¿ 400, data are consistent with a cosmological constant model. An experiment less precise than Euclid will not have enough statistical power to decisively favour a cosmological constant over the more complex alternative, and thus could not determine the nature of dark energy [9].

Modified gravity

An alternative exciting (and exotic) possibility to explain cosmic acceleration is that Einstein's theory of GR, and thus our understanding of gravity, needs to be revised on cosmological scales. Models that modify GR in a generic way change both the expansion history and the evolution of the perturbations, and thus the growth of structure in the Universe. In the simplest models, the deviation from GR can be captured as a change in the growth of structure with respect to canonical dark energy models. This is often expressed parametrising the rate of growth of a matter density fluctuation as follows:

$$f(z) = \Omega_m^{\gamma}(z) \tag{1.18}$$

where z is the *redshift* parameter (see Appendix A). For the ΛCDM model, the best fit is obtained for $\gamma = 0.55$. Any deviation from this value indicates a breakdown of GR. One of the goals of Euclid is to measure the exponent γ, thus testing GR, with a 1 σ uncertainty of 0.02.

Dark Matter

We already mentioned in Section 1.2 that DM behaves like a collission-less fluid and must have a relatively low velocity dispersion. These two characteristics translate into the fact that DM must have a low self-interaction cross section and a relatively high mass. Euclid will measure the density profiles of DM halos and the matter power spectrum with very high precision, improving constraints on the DM self-interaction cross section by three orders of magnitude over current limits and putting a lower limit on the DM mass of 2 keV. While the Large Hadron Collider (LHC) at CERN and direct detection experiments aim to probe DM particles directly, Euclid will test their macroscopic distribution in galaxies and clusters. This provides an important consistency check on their properties.

Initial Conditions

It is commonly accepted that the large-scale structure of the Universe arises from quantum fluctuations that grew to cosmological scales during inflation, the initial exponential expansion of the Universe in its early ages (*i.e.* less than 10^{-35} s after the Big Bang). This early period has been proposed for the first time by Alan Guth in 1981 to solve a number of problems in Big Bang cosmology, and could be related to the physics of DE. Simple models of inflation predict a primordial power spectrum that is nearly scale invariant with power law spectral index n_s close to unity. In more complicated models a running spectral index, depending on scale is foreseen. Euclid will measure the spectral index and its scale dependence with a precision similar to that of Planck, which provided the most accurate measure of the cosmological parameters up to now (see also Section 1.1). The characterisation of the primordial power spectrum provides an important test of inflation models.

Even the simplest inflationary models predict small deviations from a Gaussian probability distribution for the primordial density fluctuations, more sophisticated models predict higher levels of non-Gaussian fluctuations. A non linear evolution of the perturbations leads to a potential of the form [11]:

$$\Phi = \phi_g + f_{NL}\phi_g^2 \tag{1.19}$$

The parameter f_{NL} gives the amplitude of the quadratic term and it is often used to quantify non-Gaussianity. The goal of Euclid is to measure f_{NL}, improving measures inferred from CMB observation by Planck. Planck is expected to determine f_{NL} to an accuracy of ~ 5, while Euclid is aimed to determine f_{NL}

to an accuracy of ~ 2.

Table 1.2: An illustrative summary of the key parameterisations discussed throughout this thesis for each of the four primary science goals of Euclid.

Goal	**Parameters**	**Parameter detail**
Dynamical Dark Energy	w_0 and w_a	Assuming Λ, $w_0 = -1$ and $w_a = 0$. Any deviation would demonstrate DE behaves as a dynamical field
Modification of Gravity	γ	$\gamma = 0.55$ is the best fit of the ΛCDM model. Any deviation implies a deviation from GR
Dark Matter	σ_X and m_X	ΛCDM is based on cold collisionless behaviour of DM. σ_X and m_X represent the self-interaction cross section and mass of a generic particle X
Initial Conditions	f_{NL}	$f_{NL} = 0$ implies a Gaussian random field of primordial perturbation. Any deviation implies non-Gaussianity. f_{NL} quantifies the amplitude of this deviation

1.5 Cosmological probes

We may sum up the scientific goals of Euclid described so far in two main categories: mapping the expansion history of the Universe and the growth of the Universe large scale structure. To do so, Euclid will investigate two independent cosmological probes:

- **Weak Gravitational Lensing**: Weak Lensing (WL) is a method to map the DM and study DE by measuring the distortions of galaxy images by mass inhomogeneities along the line-of-sight.
- **Baryonic Acoustic Oscillation**: Baryonic Acoustic Oscillation (BAO) are wiggle patterns, imprinted in the clustering of galaxies, which provide a standard ruler to measure the expansion in the Universe and DE.

BAO are useful for cosmology since they can be used as a standard ruler. The physical size s of the ruler is known, and the measurement of its angular size on the sky constrains $d_A(z)$, the *angular diameter* distance, provides a direct

measurement of the expansion history. Euclid will also make measurements of the Hubble parameter $H(z)$. The combination of these two measurements is used to determine the curvature at different redshifts to test for changes in geometry over cosmological time scales. WL also constrains the expansion history. The amount of distortion caused by any gravitational lensing is directly dependent on the observer-lens-source geometry. On cosmological scales this means that WL is dependent on the geometry of Universe through a combination of angular diameter distances $d_A(z)$, to the weakly lensed galaxies. The correlation function of the WL signal contains this geometric information.

WL directly probes the total (dark plus luminous) matter power spectrum, as photons are sensitive to the integrated gravitational effect of all the mass along the path, while they travel towards us. By determining the DM distribution at different redshifts, WL maps will directly measure the growth rate of structure. Euclid will also provide an unprecedented measurement of galaxy clustering over the maximum possible range of separations given by the full sky, exploiting BAO signature at different scales.

Euclid will allow researchers to extract a number of ancillary measurements, which will further constrain cosmological models. Before a brief description of these additional cosmological probes, we give a theoretical introduction to the two main Euclid cosmological probes.

1.5.1 Weak Gravitational Lensing

The propagation of light in arbitrary curved spacetimes is in general a complicated theoretical problem. However, for almost all cases of relevance to gravitational lensing, we can assume that the matter inhomogeneities which cause the lensing are local perturbations: light travels from the source to a point close to the lens through unperturbed spacetime, it is deflected and travels again through unperturbed spacetime to the observer. To study light deflection close to the lens, we can assume a locally flat spacetime which is weakly perturbed by the Newtonian gravitational potential of the mass distribution constituting the lens. This approach is legitimate if the Newtonian potential Φ is weak, $\mid \Phi \mid \ll c^2$, and if the peculiar velocity v of the lens is small, $v \ll c$. These conditions are satisfied in all cases of astrophysical interest. The effect of spacetime curvature on the light paths can be expressed in terms of an effective index of refraction n, which is given by:

$$n = 1 - \frac{2\phi}{c^2} \tag{1.20}$$

The basic setup for a simplified gravitational lens scenario, involving a point source and a point lens, is displayed in Figure 1.5. For a point-like lens, there will always be at least two images S_1 and S_2 of the source. The corresponding angles and angular diameter distances are indicated:

- D_L: angular-diameter distance from observer to lens;

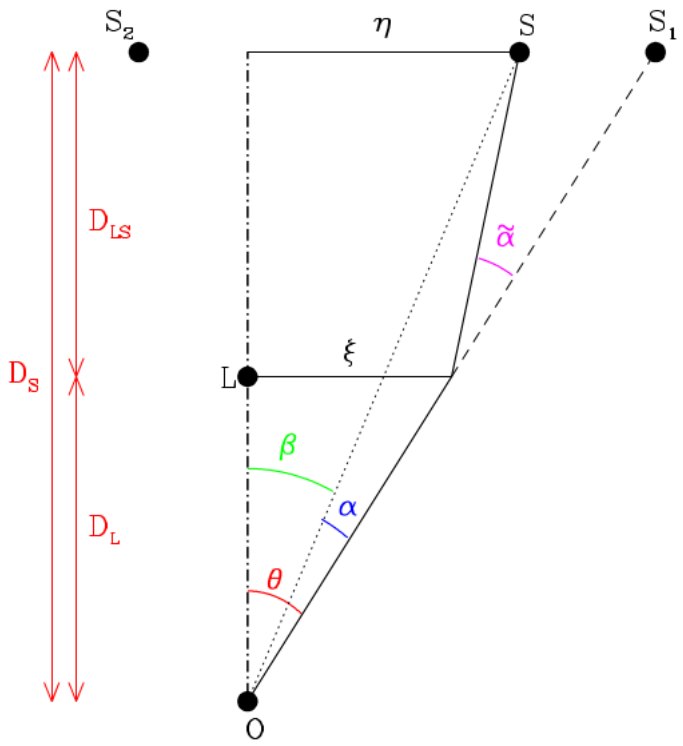

Figure 1.5: Common lensing configuration, involving the lens L, the source S and the observer O. Because of gravitational lensing, the image of the source will appear at S_1 and S_2. The distances D_L , D_S and D_{LS} are the angular-diameter distances from the observer to the lens, from the observer to the source, and from the lens to the source, respectively.
Source: Wambsganss, 1998. [12]

- D_S: angular-diameter distance from observer to source;
- D_{LS}: angular-diameter distance from lens to source;

In this scheme the origin is chosen at the observer. From the diagram it can be seen that (for θ, β and $\tilde{\alpha} \ll 1$)[6] the following relation holds:

$$\theta D_S = \beta D_S + \tilde{\alpha} D_{LS} \tag{1.21}$$

With the definition of the reduced deflection angle $\alpha(\theta) = (D_{LS}/D_S)\tilde{\alpha}(\theta)$, this can be expressed as:

$$\beta = \theta - \alpha(\theta) \tag{1.22}$$

[6]This condition is fulfilled in practically all astrophisical relevant siyuations.

This relation between the positions of images and source can be derived for a non-symmetric mass distribution as well. In that case, all angles are vector-valued. The two-dimensional lens equation then reads:

$$\vec{\beta} = \vec{\theta} - \vec{\alpha}(\vec{\theta}) \tag{1.23}$$

In the vicinity of an arbitrary point, the lens mapping as shown in equation 1.23 can be described by its Jacobian matrix:

$$\mathcal{A} = \frac{\partial \vec{\beta}}{\partial \vec{\theta}} = \left(\delta_{ij} - \frac{\partial^2 \psi(\vec{\theta})}{\partial \theta_i \partial \theta_j} \right) \tag{1.24}$$

in which we expressed the deflection angle as the gradient of an effective two-dimensional scalar potential ϕ: $\vec{\nabla}_\theta \phi = \vec{\alpha}$, where:

$$\phi(\vec{\theta}) = \frac{D_{LS}}{D_S D_L} \frac{2}{c^2} \int \Phi(\vec{r}) dz \tag{1.25}$$

and $\Phi(\vec{r})$ is the Newtonian potential of the lens [13]. If we define:

$$\psi_i j = \frac{\partial^2 \psi}{\partial \theta_i \partial \theta_j} \tag{1.26}$$

we can introduce two parameters: the convergence κ:

$$\kappa = \frac{1}{2}(\psi_{11} + \psi_{22}) \tag{1.27}$$

and the *shear* γ:

$$\begin{aligned} \gamma_1(\vec{\theta}) &= \frac{1}{2}(\psi_{11} + \psi_{22}) = \gamma(\vec{\theta}) \cos[2\varphi(\vec{\theta})] \\ \gamma_2(\vec{\theta}) &= \psi_{12} = -\psi_{21} = \gamma(\vec{\theta}) \sin[2\varphi(\vec{\theta})] \end{aligned} \tag{1.28}$$

In equation 1.28 we defined an angle φ which reflects the direction of the shear-inducing tidal force relative to the coordinate system. The Jacobian matrix can be written:

$$\mathcal{A} = (1 - \kappa) \begin{pmatrix} 1 & 0 \\ 0 & 1 \end{pmatrix} - \gamma \begin{pmatrix} \cos 2\varphi & \sin 2\varphi \\ \sin 2\varphi & -\cos 2\varphi \end{pmatrix} \tag{1.29}$$

From this expression, we see that convergence causes a local isotropic magnification of angular size, while shear produces anisotropy in the mapping. Both the

convergence and the shear are linear combination of the second derivative of the effictive potenzial ψ, which depends on the Newtonian potential of the lens. It follows that the bigger the lens effect, the higher the values of κ and γ. If we deal with small values of convergence and shear we speak about Weak Lensing.

Weak Lensing deals with effects of light deflection that cannot be measured individually, but rather in a statistical way only. It represent the most common astrophysical situation: in principle, weak lensing acts along each line of sight in the Universe, since each photon path is affected by matter inhomogeneities along or near its path. Only when averaging over a whole ensemble of images it is possible to measure the shape distortion, since the weak lensing, due to mass distributions on large angular size, acts as the coherent deformation of the shapes of extended background sources [14]. In the simplest scenario we can assume that the major axes of the background galaxies are intrinsically randomly oriented. To quantitatively reconstruct the surface mass distribution of an extended object, such as a galaxy cluster, the WL signal can be used thanks to a reconstruction method developed by Kaiser and Squires [15]. This method relies on the fact that the convergence $\kappa(\theta)$ and the shear $\gamma(\theta)$ are linear combinations of the second derivative of the effective lensing potential $\psi(\theta)$. After Fourier transform the expression for the convergence and the shear one obtains linear relations between the transformed components $\tilde{\kappa}$ and $\tilde{\gamma}$. Solving for $\tilde{\kappa}$ and inverse Fourier transforming gives an estimate for the convergence κ. The original Kaiser-Squires method has been improved, extended and generalized by various authors subsequently to take into account more complicated scenarios.

1.5.2 Baryonic Acoustic Oscillation

Before recombination the Universe consisted of a hot plasma of photons and baryons which were tightly coupled via Thomson scattering. The competing forces of radiation pressure and gravity set up oscillations in the plasma, the so called *Baryonic Acoustic Oscillations* (BAO). If we consider a spherical density perturbation, in this tightly coupled baryon-photon fluid it will propagate outwards as an acoustic wave with a speed [16]:

$$c_s = \frac{c}{\sqrt{3(1+R)}} \tag{1.30}$$

where $R \equiv 3\rho_b/4\rho_\gamma$, with ρ_b and ρ_γ the baryon and photon density respectively. At recombination the Universe becomes neutral and baryons and photons can decouple. The baryon wave stalls while the photons freely propagate away forming what we now observe as the CMB. The characteristic radius of the spherical shell formed when the baryon wave stalled is usually close to the sound horizon s, the distance a sound wave can propagate in the photon-baryon fluid by the time of decoupling:

$$s = a(t) \int_0^{t_{rec}} \frac{c_s dt'}{a(t')} \tag{1.31}$$

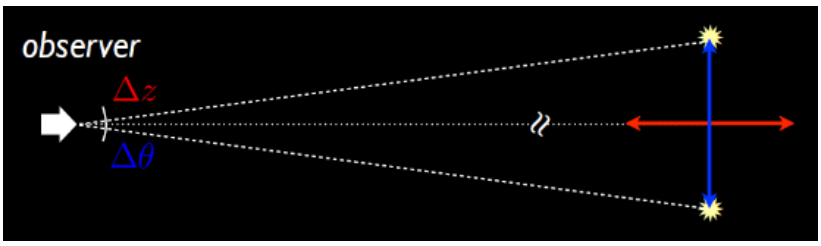

Figure 1.6: The radial length of an object is given by $c\Delta z/H(z)$, where Δz is the difference in redshift between the front and back of the object, while the transverse size of the object is $d_A(z)\Delta\theta(1+z)$ and $\Delta\theta$ is its angular size. *Source*: http://www.iac.es

It can be shown that the sound horizon depends on baryon and dark matter densities [17]. The CMB strongly constrains the dark matter and baryon densities at decoupling and hence the sound horizon, making this scale an excellent *standard ruler*. Using BAO as a standard ruler we can provide a measurement of the angular diameter distance as a function of redshift, considering the characteristic scale $s_\perp$, tangential to the line of sight:

$$d_A(z) = \frac{s_\perp}{\Delta\theta(1+z)} \tag{1.32}$$

The standard ruler can also be used on the line of sight to measure the Hubble parameter, considering the characteristic scale $s_\parallel$:

$$H(z) = \frac{c\Delta z}{s_\parallel} \tag{1.33}$$

This is illustrated in Figure 1.6. The radial length of an object is given by equation 1.33, while the transverse size is given by equation 1.32. The combination of radial and transverse distance measurements is used to determine the curvature at different redshifts to test for changes in geometry over cosmological time scales.

1.5.3 Additional cosmological probes

In addition to its two primary cosmological probes, Euclid will investigate a number of ancillary probes in order to extract further measurements to constrain the cosmological parameters. A brief description of the main secondary probes follows:

- **Clusters of galaxies**: extreme positive peaks of the matter density field are traced by galaxy clusters and provide complementary information, nearly indipendent from that of the primary cosmological probes. The cluster population bears the imprints of the statistical distribution of initial

fluctuations, their subsequent growth and the dynamics of the collapse of DM halos. For that reason clusters are an excellent probe of the growth of structure in the Universe.

- **DM density profiles**: Numerical simulations of CDM dominated universes make strong predictions about the average density profiles of collapsed structures. On galaxy scales these predictions are difficult to test because most observations probe regions where the gravitational potential is baryon dominated. Clusters of galaxies are better targets, allowing us to probe a physical regime where the fraction of baryons trace the CDM in a simple way.

- **Complementing ESA Planck data**: Constraints on cosmological parameters are significantly tightened when Euclid measurements are combined with the Planck observations of the cosmic microwave background. Euclid data themselves also enable new science using the Planck observations, by providing information on the matter distribution in front of the surface of last scattering.

1.6 Goal of this work

The measures Euclid will perform on the cosmological probes described so far require specific instrumental characteristics. WL requires a high image quality on sub-arcsec scales for the galaxy shape measurements, and photometry at visible and infrared (IR) wavelengths to measure the photometric distances of each lensed galaxy. BAO requires near-infrared (NIR) spectroscopic capabilities to measure accurate redshifts of galaxies. Both probes require a very high degree of system stability to minimise systematic effects.

A space mission requires a good and stable simulation environment, which shall enable the generation of simulated output data and support the assessment of: performance of the mission on the basis of simulated data for selected test scenarios; impact of individual error sources on the output of an ideal system, both separately and simultaneously; performance of the retrieval algorithms and of their associated assumptions.

These premises lead to the core activity of my Ph.D. project: the implementation of a prototype end-to-end simulator, using the Euclid mission as a test case, designed to assess mission performance and support instrument operations.

Before being involved in this activity, I focused on the first part of this work, describing the analysis of Jupiter flux time-lines aimed at the inter-calibration between the Planck and WMAP mission, to properly calibrate the beam pattern and to study Jupiter atmosphere.

Jupiter flux analysis improved results previously quoted in literature and is part of the Planck/LFI pipeline, due to its importance for the detector beam reconstruction and for the inter-calibration between Planck itself and its predecessor WMAP. Furthermore, Jupiter flux analysis was also an important test bench

for the second part of this Ph.D. project, aimed at developing and End-to-End simulator for the Euclid mission.

End-to-End mission performance Simulators (E2ES) enable the generation of simulated output data for selected test scenarios to support the assessment of the mission performance. In the second activity, I have been involved in the design of a reference architecture of an E2ES aimed at supporting instrument operations and in the development of a prototype, providing basic functionalities.

Scope of this work is to describe these two main activities.

Chapter 2

Euclid Mission Overview

EUCLID is a medium class ("M-class") mission and is part of the European Space Agency (ESA) "Cosmic Vision" (2015–2025) scientific program. Euclid is a mission to map the geometry of the dark Universe. The mission will investigate the distance-redshift relationship and the evolution of cosmic structures by measuring shapes and redshifts of galaxies and clusters of galaxies out to redshifts ~ 2, or equivalently to a look-back time of 10 billion years. The methods employed exploit the phenomenon of gravitational lensing and measurement of Baryonic Acoustic Oscillations (see Section 1.5). In order to achieve its scientific goals, Euclid comprises a 1.2 m diameter telescope and two scientific instruments: a visible-wavelength camera (VIS) and a near-infrared camera and spectrometer (NISP).

Euclid will be launched on a Soyuz rocket from the European launch base of Kourou, in French Guayana. After the launch it will be placed in a Lissajous path of large amplitude (about 1 million kilometres) around the Sun-Earth Lagrangian point L2. During its mission, which will last at least 6 years, Euclid will observe about 15000 $\deg^2$, nearly a third of the extragalactic sky, i.e. the sky facing away from the Milky Way. The survey will be complemented by additional observations, about 10 times deeper, pointing towards two different fields, located closed to the ecliptic poles and covering 20 $\deg^2$ each. These deeper fields will be not only used to produce scientific data, but also as calibration fields and to monitor the telescope and instrument performance stability.

With its wide sky coverage and its catalogues of billions of sources, the scientific contribution of Euclid and the value of data collected by the mission goes beyond the scope of cosmology. The database provided by the Euclid mission will give to the worldwide astronomical community a huge amount of sources and targets to be investigated by future missions both on ground (E-ELT, SKA) and in space (JWST).

2.1 Euclid Predecessors

Part of the ESA's Cosmic Vision (2015-2025) scientific program, the Euclid mission is meant to advance and complement the work done by the already mentioned Planck and the Herschel Space Observatory. Herschel and Planck were launched with an Ariane 5 rocket vector form the European launch base of Kourou (French Guyana) at 13:12 UT of the 14 th of May 2009. Both the satellites, after the launch, were placed in orbit around the Lagrangian point L2 of the Sun-Earth system, at ~ 1.5 millions km from Earth in the opposite direction with respect to the Sun, in two different Lissajous orbits. Here, we briefly describe Herschel and Planck spacecrafts and instruments.

2.1.1 Herschel

The Herschel Space Observatory is a space observatory built and operated by ESA. Originally known as FIRST (Far In-fraRed Submillimetre Telescope)

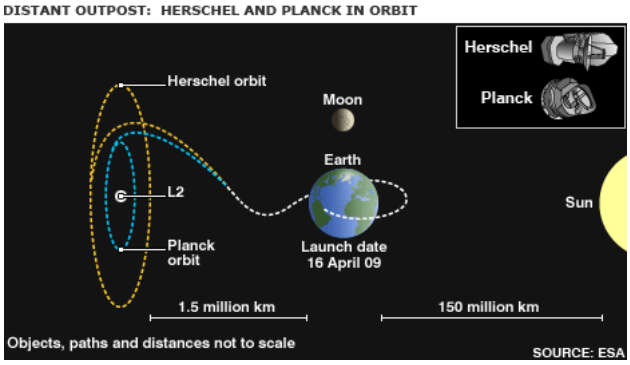

Figure 2.1: Planck and Herschel in their Lissajous orbits around the Lagrangian point L2 of the Sun-Earth system.
Source: http://www.esa.int

its name was officially changed in the year 2000 in recognition of the 200th anniversary of the discovery of infrared radiation by William Herschel in 1800. Herschel covered a spectral region closed to ground-based astronomy: the range from about 55 to 672 μm. As an observatory mission, its time was distributed among the community instead of being used for a large-scale survey. It was also a consumables-limited mission since its useful life depended on the lifetime of the helium in the dewar that was used to cool the instruments. The Herschel spacecraft lifetime was expected to be in the range from 3.5 to 4 years from launch. The end of mission was declared on the 29th of April 2013, just over 2 weeks short of completing 4 years in space.

Many aspects of the Herschel Space Observatory have been revolutionary. Carrying a single 3.5 m mirror, it represents the largest dedicated infrared telescope ever to be launched into space. For the astronomer this has converted into high sensitivity and a spatial resolution a factor of ~ 6 better than any previous far-IR telescope launched into space. This makes Herschel a pathfinder mission in the far-IR.

The Herschel Space Observatory spacecraft (see Figure 2.2) is composed by a primary mirror accompanied by three science instruments: two cameras and imaging spectrometers (PACS and SPIRE) and a very high resolution spectrometer (HIFI). Together, these instruments cover approximately a wavelength interval from 55 to 672 μm. The detectors in these instruments are cooled to temperatures close to absolute zero by a sophisticated cryogenic system. Below, a brief description of the on-board instrumentation of Herschel:

- The *Heterodyne Instrument for the Far Infrared* (HIFI) is an high resolution spectrometer, designed to observe and identify individual molecular species and study their motion, temperature, and other physical properties. This is fundamental to the study of comets, planetary atmospheres, star formation and the development of distant and nearby galaxies. HIFI could produce high-resolution spectra, covering two bands (157-212 μm and 240-625 μm).

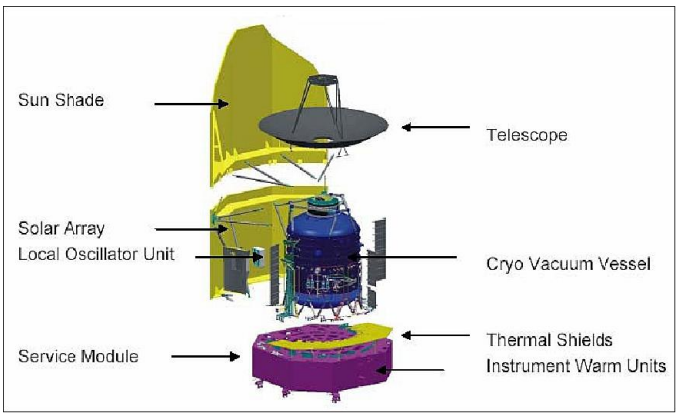

Figure 2.2: Schematic view of the Herschel spacecraft and its major components . *Source*: https://directory.eoportal.org

HIFI was designed and built by a consortium led by SRON[1] (Groningen, the Netherlands);

- The *Photoconductor Array Camera and Spectometer* (PACS) consists of a colour camera and an imaging spectrometer, covering the wavelength range from 55 to 210 μm. The PACS spectrometer has a lower resolution than that of HIFI, but it is suited to see young galaxies and the gas clouds from which stars form. PACS operates either as a photometer or as a spectrometer, using either its bolometer or its photoconductor array detectors. It was designed and built by a consortium led by the *Max Planck Institute for Extraterrestrial Physics* (Garching, Germany);
- The *Spectral and Photometric Imaging REceiver* (SPIRE), covering the wavelength range from 194 to 672 μm. Like PACS, it consists of a colour camera and an imaging spectrometer, and it covers a complementary range of wavelengths. It is designed to study the star formation history of the Universe. SPIRE performs photometry in three bands simultaneously, centred on 250, 350 and 500 μm. It can also be operated as an imaging spectrometer. It was designed and built by a consortium led by Cardiff University (Cardiff, UK).

Herschel's three instruments were complementary: each instrument was designed to study gas and dust, but at different temperatures and states. Thanks to the large range of wavelengths covered, they were be able to witness the entire process of star formation from the earliest stages of condensation.

2.1.2 Planck

The ESA mission Planck is a space-based mission designed to the study of the CMB. It represents the third generation in CMB experiments and it is the

[1]Netherlands Institute for Space Research

European successor of the American satellite WMAP. The goal of the mission was to measure the temperature fluctuations of the CMB on the whole sky, with an unprecedented combination of sensitivity, angular resolution and frequency coverage. Planck has a temperature sensibility of the order of $\Delta T/T \sim 10^{-6}$, an angular resolution $\theta \sim 5'$ and covers a frequency range from 30 to 857 GHz. Planck represents a significant test for theories about the formation of structures and provides, up to now, the most solid proof on the ΛCDM cosmological model and the most precise measure of its parameters. The Planck satellite ended its operations on the 23rd of October 2013.

Data from Planck have allowed cosmologists to set very tight constraints on many parameters of the standard model, including the Hubble constant (H_0), which describes the expansion rate of the Universe today, the densities of baryonic matter, dark matter and dark energy (Ω_b, Ω_M, Ω_Λ). The study of the power spectrum of CMB fluctuations has a central role understanding the evolution of cosmic structures on different scales.

The Planck spacecraft (see Figure 2.3) is made up of two major components, the payload module and the service module. The payload module comprises a Gregorian off-axis aplanatic telescope ,equipped with primary (diameter 1.5 m) and secondary mirrors that collect microwave radiation and direct it onto the focal plane, where the scientific instrumentation is placed. The service module is an octagonally shaped bus and contains the systems needed to operate the spacecraft and those parts of the instruments that do not require cooling. Planck mounts two scientific instruments:

- The *High Frequency Instrument* (HFI), provided by the *HFI Consortium*, led by IAS[2] (Orsay, France). HFI is a detector system based on bolometers technology covering six frequency bands from 100 to 857 GHz and working at a temperature of 0.1 K. This instrument finished its observations on the 14th of January 2012, having exhausted the cryogenic fluid necessary for its operation;
- The *Low Frequency Instrument* (LFI), provided by the *LFI Consortium*, led by IASF[3]-INAF[4] (Bologna, Italy). LFI is a detector system based on radiometers technology covering three frequency bands from 30 to 70 GHz. This instrument worked until the end of the mission.

Planck/HFI was designed around 52 bolometers. Twenty Spider-Web Bolometers (SWBs), sensitive to total power, and the remaining 32 units arranged in pairs of orthogonally-oriented Polarisation-Sensitive Bolometers (PSBs). Two more dark bolometers, not optically coupled with the telescope, monitor the thermal noise. The Planck/HFI horns are positioned at the centre of the focal plane, where the optical quality is good enough for the high frequencies. The curvature of detector rows compensates for the distortion of images by the telescope [18]. In Figure 2.4 (panel **(a)**) it can be seen how Planck/HFI detectors

[2]Institut d'Astrophysique Spatial
[3]Istituto di Astrofisica Spaziale e Fisica cosmica
[4]Istituto Nazionale di AstroFisica

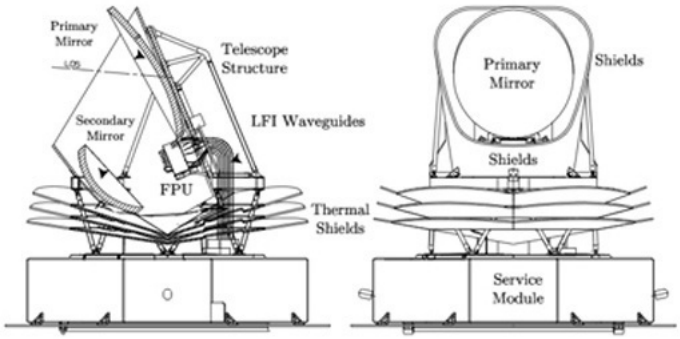

Figure 2.3: Planck spacecraft lateral (left) and frontal (right) sections. *Source*: Planck blue book [19]

are distributed on the focal plane, covering six frequencies: 100, 143, 217, 353, 545 and 857 GHz.

The Planck/LFI optical layout is composed of an array of 11 corrugated feed horns. Planck/LFI horns are placed in the external part of the focal plane, surrounding Planck/HFI. Each horn is coupled to a pair of radiometers by an Orthomode Transducer (OMT), splitting the incoming electromagnetic wave into two orthogonal, linearly polarized components. Thus, the LFI observed the sky with 11 pairs of beams associated with the 22 pseudo-correlation radiometers.

The Planck/LFI beam pattern is shown in Figure 2.4 (panel **(b)**). Beams from 18 to 23 are in the V–band (nominally from 63 to 77 GHz); we refer to them as 70 GHz. Beams from 24 to 26 are in the Q–band (from 39.6 to 48.4 GHz); we refer to them as 44 GHz. Beams 27 and 28 are in the Ka-band (from 27 to 33 GHz); we refer to them as 30 GHz.

Planck observing strategy was studied to perform a full sky observation in about six months. The spacecraft spun around its spin axis at ~ 1 revolutions per minute (rpm), with the optical axis tilted by 85° respect to the spin axis, which was always kept in anti-solar direction. To completely cover the whole celestial sphere, including the polar zones, the position of the spin axis on the ecliptic was not fixed, but made a cycloidal motion, anti-clockwise as seen from the Sun, with an amplitude of $\sim 7.5°$. Thanks to this strategy different regions of the celestial sphere are scanned multiple times, allowing a certain level of redundancy in order to minimize systematic effects.

2.2 Euclid Spacecraft

The Euclid spacecraft, Figure 2.5, has a launch mass of around 2100 kg and it consists of a cylinder about 4.5 m height with a diameter of 3.1 m. It is composed by two major assemblies:

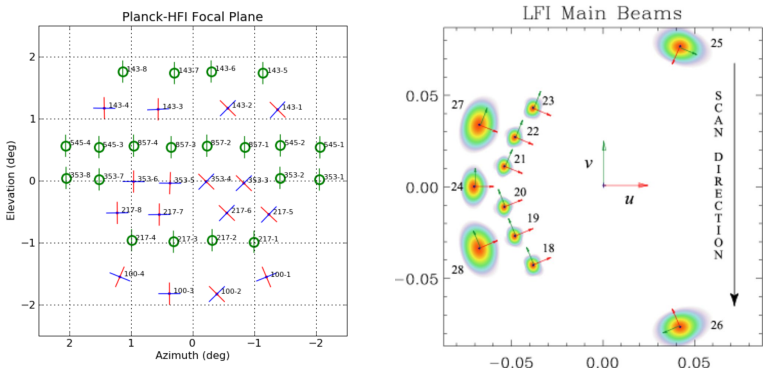

(a) *Focal plane of HFI.* **(b)** *Focal plane of LFI.*

Figure 2.4: Focal plane of the HFI and LFI instruments. HFI bolometers are placed at the center of the focal plane, surrounded by LFI radiometers. Note that the scan detection for HFI in this picture is from left to right, *i.e.* the LFI focal plane is shown rotated by 90° with respect to HFI.
HFI Source: Planck Explanatory Supplement [18]
LFI Source: Bersanelli et al., 2010 [20]

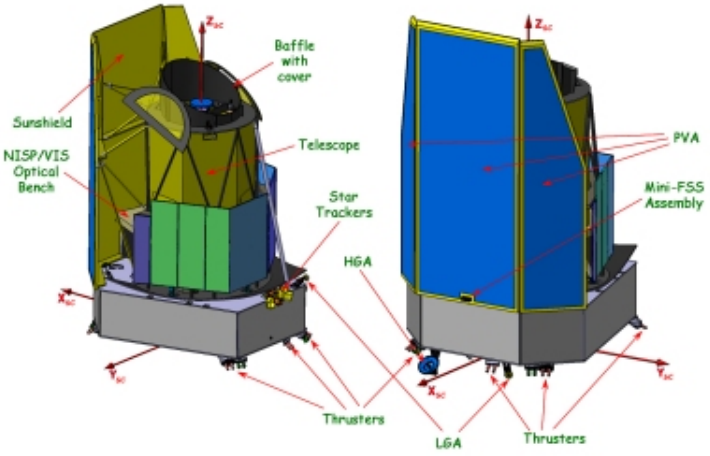

Figure 2.5: Schematic representation of the Euclid spacecraft and its components.
Source: http://sci.esa.int/euclid/

- The service module: it hosts most of the spacecraft subsystems that are needed to operate the payload, including telemetry, power, thermal control, and attitude and orbit control (AOCS).
- The payload module: it houses the telescope, the focal plane components of the instruments and some of the data processing electronics;

The service module, whose design is derived from Herschel, provides the attitude control of the satellite. To meet the high precision imaging requirements,

the Euclid AOCS provides an extremely stable pointing with a dispersion of less than 35 milli-arcseconds per visual exposure. At those accuracies, a high thermal stability is also required to protect the telescope assembly from optical misalignments. Euclid thermal stabilization is provided both via passive and active systems. The structural/thermal architecture is designed with the aim to provide a high degree of thermal isolation to the payload module as well as high thermal stability. The sunshield provides the main thermal barrier with respect to the solar heat load. Power is generated by a solar array body-mounted on the sunshield panels and stored by a Lithium-Ion battery.

The service module provides also communications: low gain antennas in the X-band (8.0-12.0 GHz) are used to support the telecommanding of the satellite and the transfer of real time housekeeping data. The nominal downlink science data, together with stored housekeeping data, is performed by K-band (20-40 GHz) at a maximum data volume of 850 Gbit/day. To store the large data volume that will be accumulated during observations, Euclid has a mass memory of at least 2.6 Tbit.

The Euclid payload consists of a 1.2 m aperture telescope with two instruments: the visual imager (VIS), equipped with one single broad band filter covering the wavelength range from 550 to 900 nm, and the near-infrared spectrometer and photometer (NISP), covering the wavelength range from 900 to 2000 nm.VIS provides high quality images to carry out the weak lensing galaxy shear measurements. NISP allows both photometric and spectroscopic redshift measures: it performs imaging photometry to provide near-IR photometric measurements and carries out slitless spectroscopy. Both instruments share a large common field of view of 0.79×1.16 deg^2. An overview of the Euclid optical scheme is given in Figure 2.6. A dichroic beam-splitter is located at the telescope exit pupil for separating the VIS and NISP optical channels with the reflected output from the dichroic beam-splitter going to the VIS instrument and the transmitted output to NISP. To meet scientific performance objectives, the telescope and payload module have to operate at a reduced temperature. To minimise dark current noise, the maximum telescope temperature was determined to be ~ 240 K.

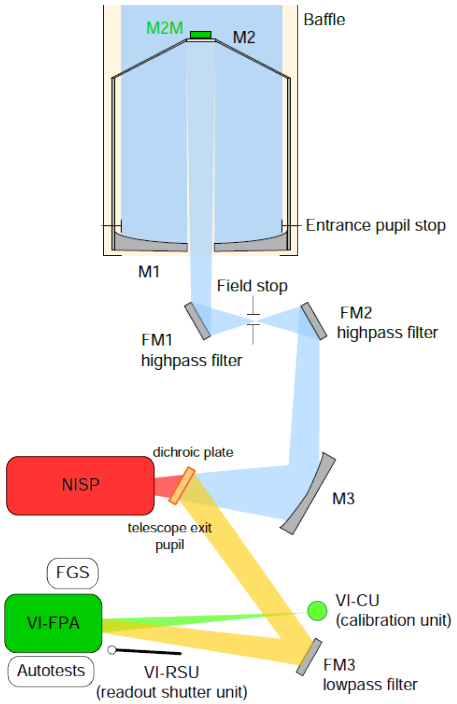

Figure 2.6: Optical scheme of the Euclid payload. Light is collected by a 1.2 m aperture telecope and divided by a dichroic plate in two channels, feeding the two instruments VIS and NISP.
Source: http://www.euclid-ec.org/

2.2.1 VIS

The Visual Imager (VIS), shown in Figure 2.7, operating in the $550-900$ nm, provides high quality images to carry out the weak lensing galaxy shear measurements. By combining 4 exposures with a total of 2240 sec, VIS will reach a magnitude limit of 24.5 for sources with an angular size of ~ 0.3 arcsec. The image sampling is 0.1 arcsec. VIS will provide deep imaging with a tightly controlled and stable Point Spread Function (PSF) over a wide survey area of 15000 deg^2 to measure the cosmic shear from nearly 1.5 billion galaxies to high levels of accuracy. VIS channel characteristics are summarized in Table 2.1.

The instrument is an assembly of different units:

- Focal Plane Assembly (VI-FPA): composed of two main parts (figure 2.8), the detector subassembly and the electronics subassembly. The detector subassembly is the 6×6 CCD matrix composing the visible focal plane array. The electronics subassembly, electrically linked to the detector one by the CCD harnesses, consists of the Read-Out Electronics (ROE) and associated Power Supply Units (RPSU) associated with the CCDs plus a

Table 2.1: VIS channel characteristics.

Capability	Visual imaging
Spectral Band	$550 - 900$ nm
System PSF size	< 0.18 arcsec (FWHM @ 800nm)
System PSF ellipticity	$< 15\%$
Sensitivity	> 24.5 mag
Field of View	> 0.5 deg^2
Survey Area	15000 deg^2
CCD pixel sampling	0.1 arcsec

mechanical support structure.

- Shutter: The shutter (VI-RSU): prevents direct light from falling onto the CCDs during the closed phase while allowing the fine guidance sensors to be exposed to light continuously. During the open phase it must avoid any interference with the light beams.
- Calibration Unit Design (VI-CU): it allows flat fields of the focal plane array to be obtained. The concept of the unit is based on an integrating sphere: the inner optical surfaces of the sphere are coated with a material with an high reflectivity over the wavelength of interest for the VIS instrument (from 600 to 900 nm). Two optical ports are foreseen, one for the illuminating sources and another one for the output light which illuminates the VI-FPA. The CU will be driven by the VI-PMCU.
- Control and Data Processing Unit (VI-CDPU): responsible for the following main activities:
  - Telemetry and telecommand exchange;
  - Instrument commanding;
  - Instrument monitoring and control;
  - Synchronisation of all the instrument activities:
  - Data acquisition, pre-processing and formatting.
- Power and Mechanism Control Unit (VI-PMCU): it encompasses all the functions required to control VIS mechanisms as well as the calibration sources.

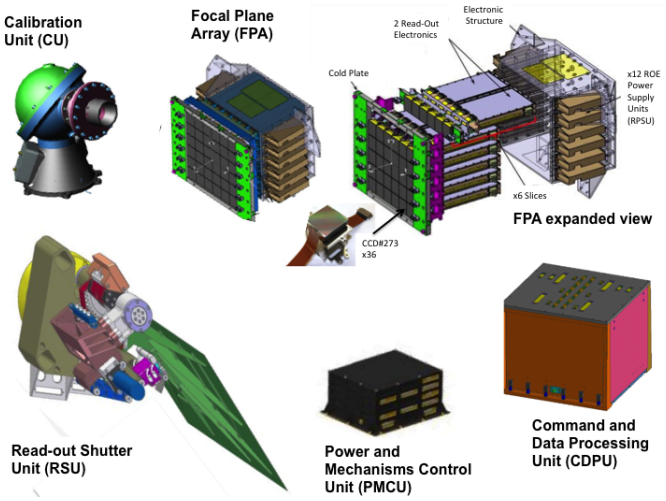

Figure 2.7: Overview of the subsystems composing the VIS instrument. From the upper-left, clockwise: VIS Calibration Unit, VIS Focal Plane and an expanded view of the Focal Plane Array, the Command and Data Porcessing Unit boxes, the Power and Mechanisms Control Unit and the VIS Shutter Unit.
Source: http://www.euclid-ec.org/

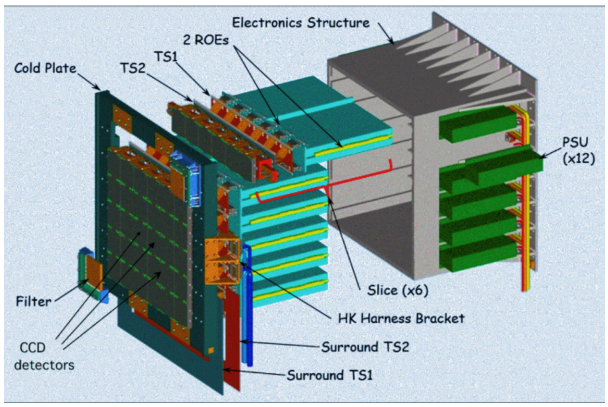

Figure 2.8: An expanded view of the focal plane assembly (VI-FPA) of the VIS instrument. VI-FPA consists of the detector subassembly, the 6×6 CCD matrix composing the visible focal plane array, and the electronics subassembly, electrically linked to the detector one by the CCD harnesses, consisting of the Read-Out Electronics (ROE) and associated Power Supply Units (RPSU) associated with the CCDs plus a mechanical support structure.
Source: Cropper et al., 2014 [25].

2.2.2 NISP

The NISP Instrument (see Figure 2.9) is a near-infrared spectrometer and photometer operating in the $0.9 - 2.0$ μm range. It has two main observing modes: the photometric mode (NISP-P), for the acquisition of images with

broad band filters, and the spectroscopic mode (NISP-S), for the acquisition of slitless dispersed images on the detectors. NISP role is to measure the redshift of galaxies.

The NISP focal plane is composed of a matrix of 4×4 detectors covering a field of view of 0.55 deg^2 share with 0.3 arcsecond pixels. The photometric channel is equipped with 3 broad-band filters (Y, J and H) covering the wavelength range from 920 to 2000 nm. The spectroscopic channel is equipped with 4 different near infrared grisms, in order to perform slitless spectroscopy, with a spectral resolution $R \sim 250$, in two bands: two "red" grisms, covering the $1450 - 2000$ nm wavelength range, and two "blue" grisms, in the wavelength range $1100 - 1450$ nm. The channel is a slitless spectrometer, so confusion between the spectra from different sources is a critical issue. To help distinguish between different sources, the channel includes two identical grism elements for each band. These are mounted with a 90 deg rotation between their lines, so that the spectrometer's dispersion direction can be changed to help distinguish overlapping spectra. The channel will be sensitive enough to detect a $3 \cdot 10^{-16}$ erg cm^{-2} s^{-1} line flux at 1600 nm wavelength [26]. NISP channel characteristics are summarized in Table 2.2.

Table 2.2: NISP channel characteristics.

Capability	near-IR photometry	near-IR spectroscopy
Spectral Band	$920 - 2000$ nm	$1100 - 2000$ nm
Spectral Resolution		$R \sim 250$
Sensitivity	> 24.0 mag	$3 \cdot 10^{-16}$ erg cm^{-2} s^{-1}
Field of View	> 0.5 deg^2	> 0.5 deg^2
Survey Area	15000 deg^2	15000 deg^2
Detector pixel sampling	0.3 arcsec	0.3 arcsec

The instrument is composed of different units, organized in three main assemblies [26] [9]:

- The Opto-Mechanical Assembly (NI-OMA), composed of the mechanical structure and its thermal control and the optical elements. It comprises the Grism Wheel Assembly (NI-GWA), holding the four dispersing elements for the spectroscopic mode, the Filter Wheel Assembly (NI-FWA), holding the three filters for the photometric mode, and the Calibration Unit (NI-CU), injecting calibration signal in the optical beam for calibration purposes.
- The Detector System Assembly (NI-DS), composed of The Focal Plane Array (NI-FPA) and the Sensor Chip System (NI-SCS). The NI-DS assembly comprises the 16 NISP detectors and provides detection of the near IR signal in photometric and spectroscopic mode.
- The Warm Electronic Assembly (NI-WE), composed of the Instrument Data Processing Unit (NI-DPU), the Detector Control Unit (NI-DCU) and the Instrumental Control Unit (NI-ICU). The NI-DPU provides data compression and packeting as well as the interface to S/C Mass Memory

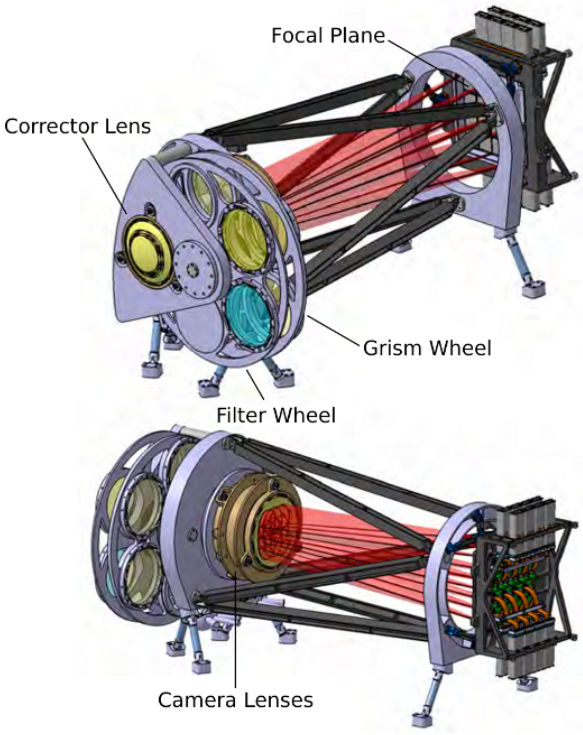

Figure 2.9: The The Near-Infrared Spectrometer and Photometer.
Source: http://www.mpia.de

and to the NI-DCU, NI-DCU provides the data and command interface to NI-DS, while the NI-ICU controls the instrument, powers and controls mechanisms, providing instrument thermal control, and the command interface with NI-DPU and NI-DCU.

2.3 Observing Strategy

Euclid is designed to survey the sky in a "step-and-stare" mode, meaning that the spacecraft will point toward a designated field on the sky, perform a nominal sequence of observations that includes visible imaging mode, near infrared photometry imaging mode and near-infrared spectroscopic mode. On a daily basis, Euclid observes strips, *i.e.* observations of adjacent sky fields along a great circle of constant ecliptic longitude b.

The observation sequence of a field is composed of four frames having a common area of 0.55 deg^2, observed with a dither step in-between. During each frame VIS and NISP carry out exposures of the sky simultaneously. At the end of the last frame, a slew towards the next field is performed. An example of the

operational time sequence of one frame is shown in Figure 2.10). VIS observes with an integration time of 565 s. NISP Spectroscopy integration time is of 565 s, followed by NISP photometric measurements with the following integration times: 121 s in the Y band, 116 s in J and 81 s in the H band. In the first 585 s both VIS and NISP take data for WL and spectra, then, since filter wheel rotation causes image disturbing vibration, VIS has its shutter closed during the remaining exposures taken for near-IR imaging.

For the imaging channels, dithering is required to fill the gaps between the detectors, and to ensure that the field is completely covered. The dithering strategy also mitigates the impact of defects and cosmic rays on science data. The time necessary to carry out a dither or a field-to-field slew depends on the attitude and orbit control system design. The pointing displacements during the dithers have been optimised to the following [9]:

- Dither 1: $\Delta X = 100$"; $\Delta Y = 50$"
- Dither 2: $\Delta X = 100$"; $\Delta Y = 0$"
- Dither 3: $\Delta X = 100$"; $\Delta Y = 0$"

being ΔX and ΔY the displacements along the two axis from one dither to the other, assuming the reference pointing as dither 0. In the case of NISP spectroscopy, the four dithers are used to obtain slitless spectra in two adjacent wavelength intervals with three grism rotations to minimise source confusion due to overlapping spectra. Exposures are taken with the dispersion rotated by 90° in dither 1, 180° in dither 2 and again by 90° in dither 3.

The main survey is the Wide Survey (WS), which covers $\sim$ 15000 deg^2 of extragalactic sky, the regions covering $|b| > 30$ deg. The survey strategy is determined by the following elements:

- **Stability**: by design, the Solar Aspect Angle (SAA), the angle between the satellite boresight and the satellite-Sun direction, is allowed to vary between 90 and 120 deg. SAA variations can cause a relevant degradation of the image quality. The survey strategy aims at minimising SAA variations over the entire survey in order to secure the quality of the input raw data.
- **Sky background**: a strong source of background light is the Zodiacal Light, due to light scattered by zodiacal dust particles. This emission has a smooth distribution and is highest in the ecliptic plane and decreases towards the ecliptic poles. The shortest Euclid wavelengths are affected the most by zodiacal light. The survey strategy gives a higher priority to regions at higher ecliptic latitudes.
- **Galactic extinction**: dust in the Galaxy causes extinction of the light of galaxies. Galactic extinction has been mapped down to arcminute scales using infrared data from preavious missions (IRAS, WMAP and Planck). These maps will be used to select the best areas on the sky in terms of low extinction.

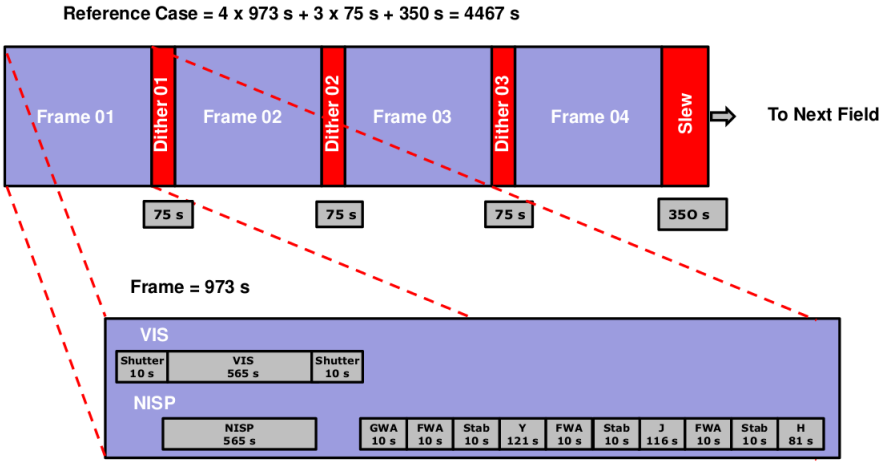

Figure 2.10: Example of a schematic timeline of an observation sequence of one field. Each frame (blue) starts with a simultaneous VIS and NIS exposure, followed by three NISP photometric exposures. The three dither-to-dither slews and the field-to-field slew are marked in red. Time allocations for the VIS shutter and the filter wheel movements are indicated in the gray boxes
Source: Euclid Red Book [9].

- **Exposure time**: the exposure times described in this section are tuned to reach the mission requirements of a detection limit of 10 sigma extended source at 24.5 mag, emission lines flux limit at $3 \cdot 10^{-16}$ erg cm^{-1} s^{-1} and have near-IR imaging in Y, J and H at 24.0 mag.

Euclid is designed to perform also a Deep Survey (DS), built by repeatedly observing the same area on the sky in the WS observing mode. The DS covers at least two separate fields in the northern and southern celestial hemisphere, each of 20 deg^2. Due to viewing constraints, sky areas can only be visited regularly by Euclid if they are situated at high ecliptic latitude, where visibility is highest. The field orientation is different at different epochs due to the satellite's annual motion around the Sun. This is an advantage because different orientations are needed to mitigate confusion due to overlapping spectra and to achieve accurate photometric inter-calibrations over large areas.

Chapter 3

Jupiter Analysis

The spectral energy distribution (SED) at millimetric wavelengths of planets is an important benchmark to intercalibrate different CMB experiments, to properly calibrate the beam pattern and it is a source of information on the atmospheric structure of those bodies. Despite their importance, there is a lack of very accurate measures of SED for those bodies. Planck/LFI observed Mars, Jupiter, Saturn, Uranus and Neptune from three to eight times during the mission. In particular, Planck provided a good measurement of the Jupiter brightness temperature, with an accuracy better than half percent [24], improving the results currently quoted in literature, providing mesurements at the nominal Planck/LFI frequencies. These measurements, together with WMAP results, populate the microwave spectrum of Jupiter, shown in Figure 3.2, in the frequebncy range from 22 to 90 GHz.

Jupiter flux analysis is an important part of the Planck/LFI calibration procedure. Furthermore, we are interested in the intercalibration between Planck and WMAP data. This can be achieved by comparing our results on the Jupiter spectral analysis to the results of the same analysis performed on WMAP. A complete description of the different analysis procedures is given, together with the main results and lessons learned.

This analysis, described in Section 3.2, represents my contrubution to the Planck/LFI calibration pipeline and it is propaedeutic to the main topic of this work in several aspects. High precision measurements, which are the goal both of Planck and Euclid, represent a complex problem, in which several details have to be taken into account. It is required a good knowledge of scientific objectives, as well as of the observational scenario, the instrumental setup and the data processing and calibration procedures. The simulation pipeline presented in the next part of this work inherits the expertise made during the analysis of Jupiter, not only from the point of view of the structure of the pipeline, but also technically (software tools and I/O interfaces).

3.0.1 Planck Calibration

Accurate calibration is crucial to ensure reliable cosmological and astrophysical results from the Planck mission. Internally consistent photometric calibration of the nine Planck frequency channels is essential for component separation, where the CMB from the varoius Galactic and extra-galactic foreground emission processes are disentangled [21][22]. Furthermore, a solid absolute calibration is needed to compare and combine Planck data with results from other experiments, most notably with WMAP.

Dealing with Planck/HFI [23], the bolometer signal measured is proportional to the small variation in the incoming power from the sky. To express the measurement in sky temperature units, the gain of each detector must be determined, considering a known source in the sky. For the Planck/HFI low frequency channels (100 to 353 GHz), the CMB dipole is used as a primary calibrator. This signal fills the entire detector beam and is almost insensitive to the beam profile and only marginally affected by pointing errors. Moreover, it is stronger in signal than CMB anisotropies by a factor of about 10, but not bright

enough to cause non-linearities in the detectors. Furthermore it has the same electromagnetic spectrum as the anisotropies. At higher frequencies (545 and 857 GHz), calibration is performed on planets.

Planck/LFI photometric calibration consists in the conversion of the voltages measured by the radiometers into a set of thermodynamic temperatures. First order calibration is made via the dipole anisotropy which is not a cosmological feature and is due to the relative motion of the observer with respect to the CMB. The dipole D is given by [24]:

$$D(\mathbf{x}, t) = T_{CMB} \left(\frac{1}{\gamma(t)(1 - \beta(t)\mathbf{x})} - 1 \right) \tag{3.1}$$

where T_{CMB} is the CMB monopole temperature ($\simeq 2.725$ K), $\beta = \mathbf{v}/c$ is the spacecraft velocity, and $\gamma = (1-\beta^2)^{-1/2}$. The output voltage of each Planck/LFI radiometer is modeled as [24]:

$$V(t) = G(t)[B * (T_{Sky} + D)](t) + N \tag{3.2}$$

where G is the antenna gain of the radiometer (measured in VK^{-1}), B is the detection beam response, D is the CMB dipole signal thermodynamic temperature (including relativistic corrections), T_{Sky} is the overall temperature of the sky apart from D (CMB anisotropies, diffuse Galactic emission and other foregrounds) and N is a noise term. The $*$ operator represents a convolution over the 4π sphere. The goal of the calibration pipeline is to infer the value of the calibration constant G of each radiometer, which is used to convert the voltage V into a thermodynamic temperature.

3.1 Jupiter brightness temperature and Planck calibration

As described before, Planck/LFI radiometers do not directly detect a temperature signal, but a voltage. A conversion constant G is needed in order to calibrate the scientific timelines to physical units (K_{CMB}) [27]. Calibration is made exploiting the dipole, which, in principle, is the same for each experiment and indipendent cross-calibration sources are needed in order to inter-calibrate different CMB experiments, such as Planck itself and WMAP. Planets provide a useful calibration cross-check; in particular, the measurement of the brightness temperature of Jupiter is a very good way to assess the accuracy of the calibration, as Jupiter is a remarkably bright source with a signal per scan as high as 0.3 K_{CMB} (see Figure 3.1) and a relatively well known spectrum [28]. Furthermore, at the resolution of Planck/LFI beams it can be considered a point-like source [24]. Being nearly point-like, Jupiter can be used to reconstruct the main beam pattern of the radiometers, in order to calibrate the simulated beam models.

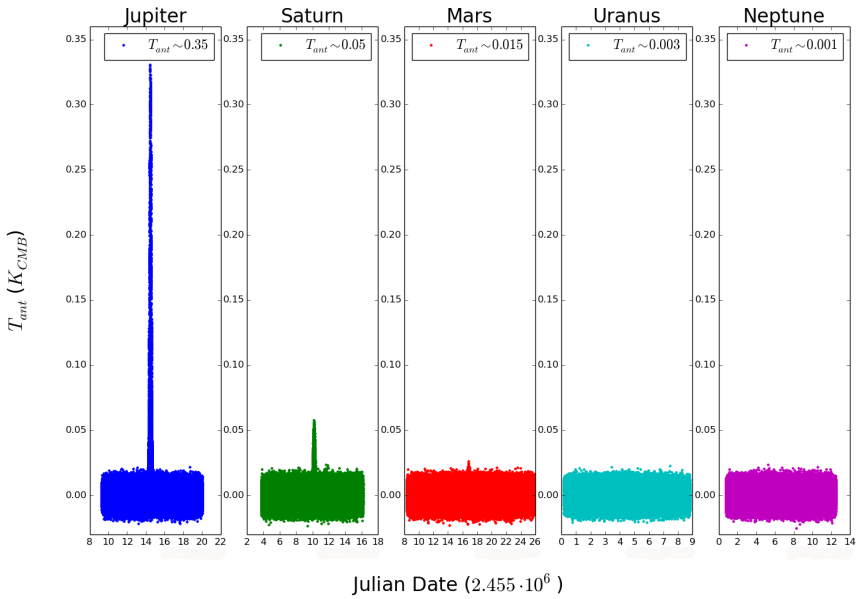

Figure 3.1: Antenna temperatures of planets detected by the 70 GHz Planck/LFI radiometer 18S. The figure shows the antenna temperature detected by the radiometer during the first transit of each planet on the Planck/LFI focal plane Compared with a confusion noise of some 10^{-3} K_{CMB} and a background of some 10^{-4} K_{CMB}, Jupiter is the brightest source with a $T_{ant} \sim 0.35$ K_{CMB} and a SNR greater than 300. Jupiter transits on the Planck/LFI in different epochs during the mission. Combining different transits we can imporve the SNR by a factor of $1 \setminus \sqrt{n}$, with n the number of transits, but we lose controll on time-dependent systematic effects. The same applies combining different radiometers in a channel. [29]

The analysis on the brightness temperature of Jupiter is not only important for the Planck/LFI calibration, but gives to the community results in order to reconstruct the microwave spectrum of the atmosphere of Jupiter, shown in Figure 3.2. Using Jupiter as a calibration source Planck, and WMAP, measure the brightness temperature T_b of the planet in different microwave bands. The microwave spectrum of Jupiter is dominated by an ammonia absorption band and it depends on the abundance and phase of this compound. Ammonia is present in a small amount in the Jupiter atmosphere, which is mostly made of molecular hydrogen and helium, but it affects strongly the spectrum seen by Planck and WMAP. Jupiter SED is hard to model since a good radiation transport model is required and few accurate measurements can be found in literature. In this picture, Planck and WMAP data fit within a multi-wavelength analysis of Jupiter SED, meant to improve our knowledge of the Jupiter atmosphere and to create a solid atmospheric model for this planet.

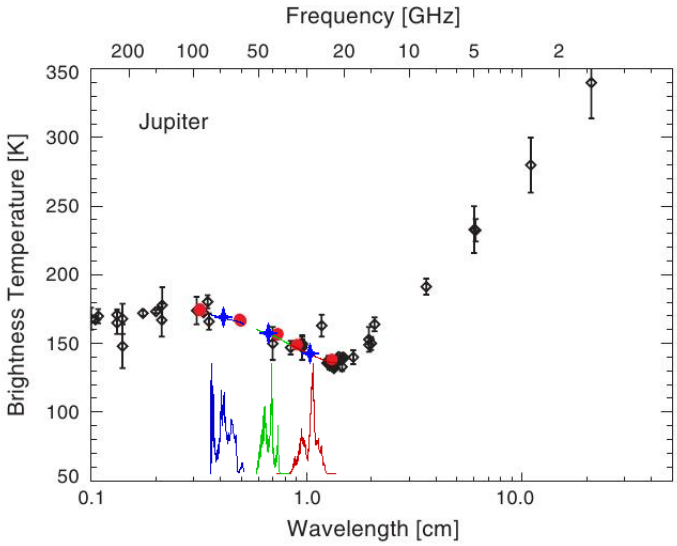

Figure 3.2: Microwave spectrum of Jupiter. Black diamonds represent selected observations compiled from literature. Red dots represent the seven-year mean WMAP temperatures, while the blue crosses represent the Planck 2013 Planck/LFI measurements. In figure, the spectral bands of the three Planck/LFI channels are reported. For each channel we report the average band of all radiometers. WMAP and Planck error bars are too small to be resolved in this plot.
Source: Weiland et al., 2010 [28].

3.2 Jupiter analysis

Planets transit the Planck focal plane when their angular distance from the Planck spin axis is about 85°. Figure 3.3 shows this angle as a function of the mission Operative Day (OD). Planck surveys are delimited by black lines. A planet crosses one or more horns when the corresponding line falls inside the dark gray band. Corresponding samples from calibrated timelines are extracted and processed. To better asses background removal, a larger acceptance (5° radius) is considered, shown in light gray. A typical transit lasts for 7-10 days, but each horn observes a planet for no more than a day. During the whole Planck mission, Planck/LFI scanned Jupiter seven times. Saturn, Uranus and Neptune have been observed eight times, while three useful observations of Mars have been collected.

Jupiter samples are considered valid if acquired in stable conditions during a pointing period, not flagged as *bad* by the calibration pipeline [27]. Samples of Jupiter transits have been first of all extracted from the Planck data timelines. We refer to a *timeline* (one for each of the 22 Planck/LFI radiometers) as the list of values $(t, \mathbf{x}_{p,t}, \mathbf{x}_t, \psi_t, T_{ant,t})$, with t the epoch of observation, $\mathbf{x}_{p,t}$ the istantaneous apparent planet position as seen by Planck (recovered from the

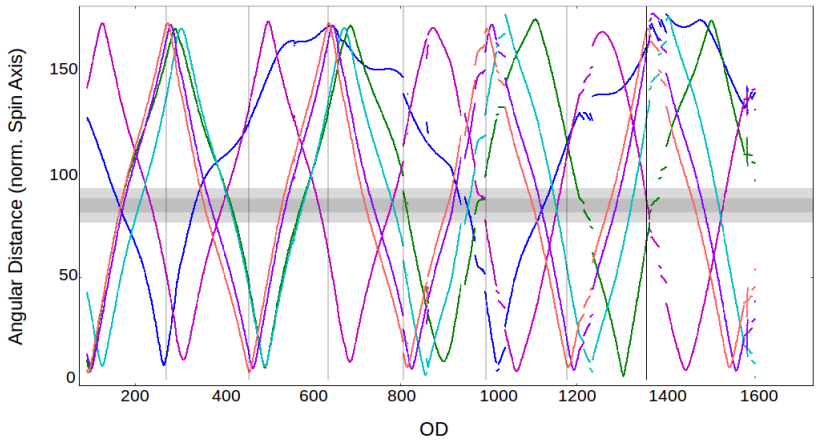

Figure 3.3: Angular distance of planets from the Planck spin axis as a function of the mission Operative Day (OD). The color code is: Blue = Mars; Green = Jupiter; Magenta = Saturn; Cian = Uranus; Violet = Neptune. Planck surveys are delimited by black lines. A planet crosses one or more horns when the corresponding line falls inside The dark gray band. To asses better background removal, a larger acceptance (5° radius) is considered, shown in light gray.

Horizons on-line service[1]), $\mathbf{x}_t$ and ψ_t the corresponding beam pointing directions and orientations, and $T_{ant,t}$ the measured antenna temperature. Samples from each radiometer timeline are used in this analysis only if their angular distance from the planet position at the time of the measurement is less than 5° and they are not affected by any anomaly or relevant background source. The last condition is visually checked by inspecting co-added micromapsof the selected samples.

The recovery of the instantaneous planet signal from a timeline is equivalent to the deconvolution of the planet shape from the beam pattern B_t at time t [29]. Since the planet can be considered a point source, the most practical way is to assume:

$$T_{ant,t} = T_{ant,p} B_t(\delta \mathbf{x}_{p,t}) + bkg \tag{3.3}$$

where $T_{ant,p}$ is the unknown planet antenna temperature, bkg the background, and $B_t(\delta \mathbf{x}_{p,t})$ the beam response for the planet at the time of observation. If a suitable beam model is available, B_t can be determined and $T_{ant,p}$ can be recovered fitting the beam model on the planet timeline. An elliptic Gaussian-beam shape centered on the instantaneous pointing direction has been chosen as a model for the beam, since it shows a very good match with the main beam of the simulated model [30].

We derive antenna T_{ant} for Jupiter fitting an elliptic Gaussian beam whose

[1] http://ssd.jpl.nasa.gov/horizons.cgi

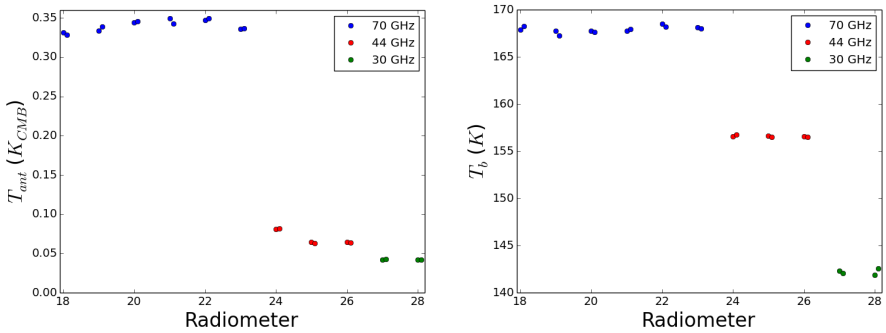

(a) Antenna temperature. **(b)** Brightness temperature.

Figure 3.4: Antenna temperature T_{ant} and brightness temperature T_b of Jupiter per radiometer. Points are coupled since for each radiometer we have two detectors with two orthogonal polarizations.

parameters are defined by the Instrument database. The brightness temperature T_b, describing the temperature of the planet assuming it as a black body, is computed from T_{ant} by means of the following formula:

$$T_b = B_{bb}^{-1}\left(T_{ant} f_{sl} \frac{\Omega_{beam}}{\Omega_{planet}} \frac{\partial B_{bb}}{\partial T}\bigg|_{T_{CMB}}\right) \tag{3.4}$$

where B_{bb} is the Black Body function, f_{sl} takes into account the beam efficiency, Ω_{beam} and Ω_{planet} are the beam and planet solid angles respectively and $T_{CMB} \approx 2.7$ K is the CMB mean temperature. In the convertion of T_{ant} to T_b through Equation 3.4, we are taking into account a number of small corrections, mostly related to the geometry of the observational scenario:

- Detector-to-detector differences in the beam solid angle Ω_{beam}. Each radiometer has a different Ω_{beam} that must be taken into account in the analysis. This is probably one of the most important effects, accounting for $\pm 6\%$ of T_b;
- Changes in the solid angle of the planet Ω_{planet}, due to the change of Jupiter–Planck distance. This is another important effect, introducing a correction factor up to 6.9%;
- Changes in the projected planet ellipticity, due to the planetocentric latitude of the observer and the oblateness of the planet, to reduce observations as if they were made at Jupiter's Pole;
- Blocking of background radiation by the planet. The planet blocks the CMB radiation, resulting in a loss of signal. This effect changes from about 0.7% to 1.5% depending on the ratio $\Omega_{planet}/\Omega_{beam}$;

At 70 GHz, Jupiter spectrum can be treated as that of a black body with mildly varying T_b in the 180 K range (see Figure 3.2). Thus, at Planck/LFI frequencies,

Jupiter spectrum can be described as that of a black body in the Ryleigh-Jeans approximation, where a ν^2 dependency applies. Dipole spectrum can be treated as well in Rayleigh-Jeans approximation, scaling down as ν^2. To take into account that Jupiter is not a real black body, the CMB spectrum deviates from the Ryleigh-Jeans approximation at higher frequencies and the detection beams are not monochromatic, we must consider second order photometric correction deriving T_b:

- A Color Correction (CC), taking into account the difference in SED between the CMB and Jupiter [31].
- A Band Average correction (BA), taking into account the bandpass of the beam.

Figure 3.4 shows the antenna temperature measured by each radiometer and the corresponding brigthness temperature. It can be seen that the values of T_b measured by radiometers in the same frequency channel have a small Radiometer-to-Radiometer (R2R) variation. This variation is independent on the transit: on a transit-by-transit base, T_b for a given radiometer is indeed quite stable. That can be seen in Figure 3.5, showing the 70 GHz channel case: the peak-to-peak variation is $\sim 1\%$ in the worst case. The R2R spread is of 0.6%, 1.0%, and 0.6% of the average signal at 30, 44 and 70 GHz, respectively. These observed dispersions are a factor of ~ 3 larger than the confusion noise,and cannot be ascribed to the background. The excess dispersion must be due to a small residual systematic effect such as pointing, beam model, or mismatch in the center frequency [24].

3.2.1 Central frequency

The determination of Jupiter T_b requires to evaluate functions in equation 3.4 at the central frequency ν_{cent} of each radiometer. This parameter is derived from:

$$\nu_{cent} = \frac{\int \tau(\nu)\nu d\nu}{\int \tau(\nu) d\nu} \tag{3.5}$$

where $\tau(\nu)$ is the detector bandpass, which is not known exactly. An uncertainty in the bandpass will reflect in a systematic error in ν_{cent}. It is possible to remove most of the differences among the 30 GHz and the 44 GHz radiometers by slightly changing the ν_{cent} of the radiometers by as little as ± 0.2 GHz. However, it is still not clear how band shapes would have to be modified to explain such changes in ν_{cent}.

At 70 GHz the situation is even more complicated. In the 30 and 44 GHz channels, the spread in ν_{cent} between each radiometer in the same frequency channel is small. On the contrary, the ν_{cent} values of the radiometers of the

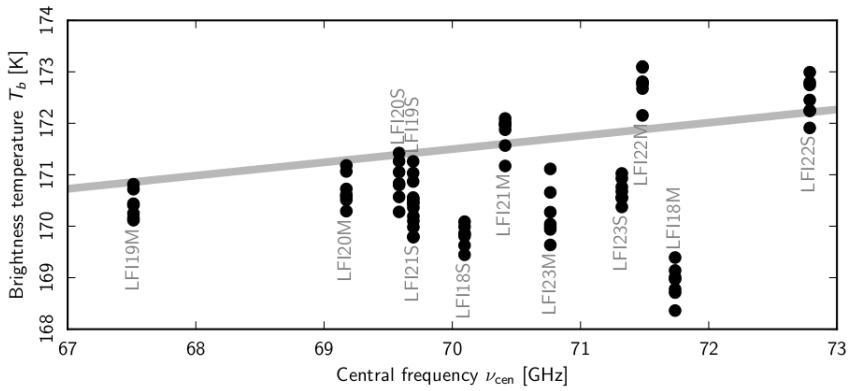

Figure 3.5: Distribution of the values of T_b for Jupiter at 70 GHz as a function of the central frequency ν_{cent} of each radiometer. For each radiometer, each black dot represents the value of a different transit. The spread among the single transits is still under investigation.
Source: Planck 2015 [24]

70 GHz channels are significantly spread over the channel bandwidth, so each of the 70 GHz radiometers samples a slightly different portion of the Jupiter spectrum. We make a comparison between T_b at 70 GHz from one transit to another after having ordered the radiometers for increasing ν_{cent}, as shown in Figure 3.5. It is possible to see a slope in the Jupiter spectrum at 70 GHz. The inferred slope $dT_b/d\nu_{cent}$=(0.2570 ± 0.0058) K/GHz matches very well with the one from WMAP data $dT_b/d\nu_{cent}$=(0.243 ± 0.025) K/GHz and can be partially responsible of the R2R scatter. To take this into account we derive, by a linear regression of the T_b against ν_{cent}, a new list of "cleaned" T_b values.

The same test is attempted in the 30 and 44 GHz channels, but the spread in central frequencies is to small to produce meaningful results [24].

3.2.2 Improvements to the fitting method

Since Jupiter can be considered a point-like object at Planck/LFI frequencies, it represent a good source in order to reconstruct the detector beam pattern. On top of that, possible dependencies of the R2R dispersion on the fitting method of the beam has to be investigated. Different tests, described below, are performed on the fitting method.

Free beam parameters

Instead of taking elliptical beam parameters from the mission database, those parameters can be left as free parameters in the fit. Fitting T_{ant} together with beam parameters, allows us to validate our model of the beam. The relative difference between the database parameter and the fitted parameters is shown

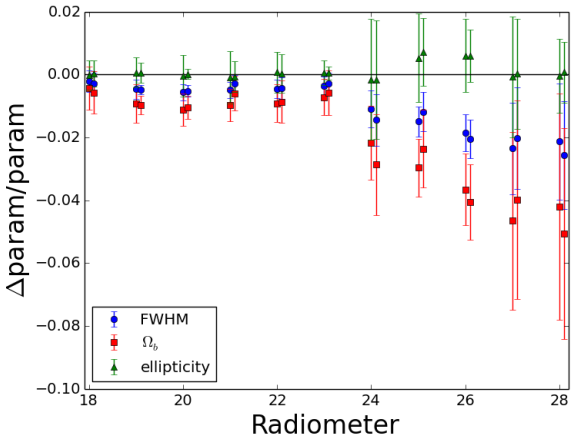

Figure 3.6: Relative difference between the database parameter and the transit averaged fitted parameters. The error bars represent the peak-to-peak variation of the values.

in Figure 3.6. Data are averaged over the seven transits and the error bars represent the peak-to-peak variation of the values. Differences of at most a few percent are found. The difference in Ω_{beam} reflects the dependency of the beam solid angle on the beam FWHM ($\Omega_{beam} \approx (FWHM)^2$). This analysis suggests that the detection beam can present small deviations from the model taken from the mission instrument database. This can be ascribed to different approaches to the beam reconstruction and different treatment of possible tiny deviations of the real beam from a perfect Gaussian profile.

Validation of the numerical fitting method

A lack of convergence in the numerical fitting procedure can be the source of the anomalies in Jupiter measures. To test this case we compared two methods of fitting beam parameters plus Jupiter T_{ant}:

- The elliptic Gaussian fit with free beam parameters described above;
- A closed form for the elliptical beam, based on the assumption of negligible background, that is a quite good approximation for Jupiter.

The closed form of an elliptical gaussian can be expressed as:

$$g(x,y) = \exp\left\{-\frac{1}{2}\begin{pmatrix} x \\ y \end{pmatrix}^T U \begin{pmatrix} 1/\sigma_x^2 & 0 \\ 0 & 1/\sigma_y^2 \end{pmatrix} U^{-1} \begin{pmatrix} x \\ y \end{pmatrix}\right\} \tag{3.6}$$

where:

$$U = \begin{pmatrix} \cos\phi & -\sin\phi \\ \sin\phi & \cos\phi \end{pmatrix}$$

is the rotation matrix, given a rotation angle ϕ. Equation 3.2.2 can be expressed in a parametric way in order to perform a linear fit on the data.

The two methods agree at the level of $6 \cdot 10^{-7}$ K for T_{ant} and at the level of $6 \cdot 10^{-4}$ K for T_b. The relative difference in beam parameters obtained rarely exceeds $5 \cdot 10^{-6}$. This fitting method can be considered equivalent to the previous one, validating the fitting method applied so far.

Fit on micromaps

Assuming a possible dependence on input data sampling, instead of applying fitting on timelines, the same fitting procedures is performed on micromaps. Micromaps are defined as squared grids of $10.32^\circ \times 10.32^\circ$ (1801×1801 pixels), regularly sampled, drawn in the beam reference frame and centered on the beam. Micromaps have a resolution of 0.34 arcmin/pixel. Micromaps are filled by taking filtered timelines and their pointing directions, rotating the pointing directions to the beam reference frame, averaging all the samples which fall inside a map pixel. In Figure 3.7 the relative differences between the transit averaged T_b inferred from micromaps and timelines, with respect to the timeline values, are shown. The differences are of the oreder of few 10^{-3} and the values inferred from micromaps and timelines fitting show the same pattern and the same R2R variability. The R2R spread, therefore, does not come from data sampling. Furthermore, the micromap analysis allows us to visually check if pixels are effected by background sources and, eventually, remove the affected pixels. This means that, if the R2R variation was due to a bad background or confusion noise removal, we should have solve it, at least partially. Since this is not the case, we can ascribe the R2R variation to some kind of systematics.

Fit within -3 dB limit

Performing the fit, an angular threshold equivalent to 1.3 FWHM of search radius is taken. This is equivalent at taking data on the shoulders of the main detection beam within -12 dB. This is much larger than -3 dB level used to define the parameters for gaussian beam stored in the mission database. A fit with mission database parameters is repeated by taking data rigorously within the -3 dB limit. The resulting T_b shows a deviation of at most 10^{-4}, as shown in Figure 3.8. Therefore those measures are not sensitive to the choice of the angular threshold.

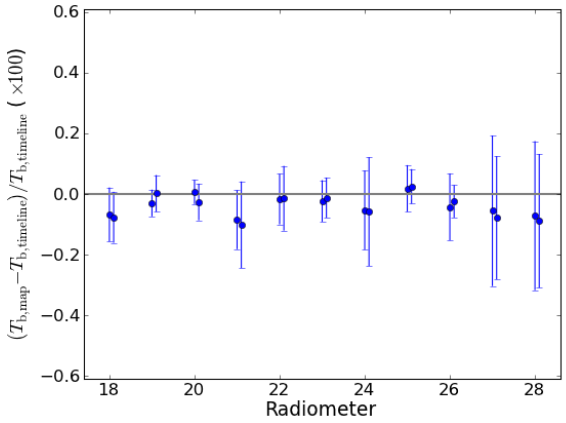

Figure 3.7: Relative differences between the transit averaged T_b inferred from micromaps and timelines with respect to the values inferred from timelines.

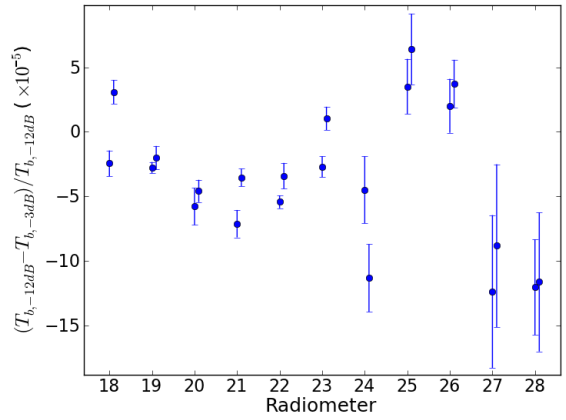

Figure 3.8: Relative differences between the transit averaged T_b inferred within the -3 dB limit and within the -12 dB commonly used in the analysis. The error bars represent the temperature rms.

3.3 Results and comparison with WMAP

Jupiter analysis provides a precise measure of Jupiter brightness temperature T_b per radiometer per transit. The extraction method corrects some features due to the geometry of the observational scenario. Some second order corrections are performed taking into account beam bandpasses and the small differences in Jupiter and cosmological dipole SEDs. The measured T_b shows a residual R2R deviation of 1% in the worst case (44 GHz). One possible cause of the observed dispersion can be a systematic effect in the estimation of the beam. A correction of the values of the radiometer central frequency ν_{cent} seems to remove this effect. However, it is still not clear how to modify the bandpass

shapes to explain these changes is ν_{cent}. Beam bandpasses are considered by the photometric calibration and we do not find any compliant result in previous steps of the calibration pipeline. For that reason correction treated in Subsection 3.2.1 has not been considered in the 30 and 44 GHz radiometer data. On the other end, the measures in the 70 GHz channel have been scaled taking into account the presence of a slope $dT_b/d\nu_{cent}$ in the spectrum at those frequencies. The inferred slope has a good agreement with that measured by WMAP.

In order to have three estimates of T_b at the three Planck/LFI nominal frequencies, 30, 44, and 70 GHz, the measurements of the 22 Planck/LFI radiometers have been averaged. Results are listed in Table 3.1. Errors, taking into account both confusion noise and statistical rms, are less than 1% in all the three channels at 30, 44, and 70 GHz.

Table 3.1: Brightness temperature of Jupiter [24].

Channel [GHz]	**Central Frequency [GHz]**	**Temperature** [K]
30	28.4	145.9 ± 0.9
44	44.2	159.8 ± 1.4
70	70.4	171.6 ± 1.0

The analysis of different fit methods shows that the real detection beam can present deviations of the order of a few percent from the elliptic Gaussian model reconstructed from the mission instrument database parameters. This is probably due to different approaches in the beam reconstruction and, together with the R2R scatter, can suggest some kind of systematic effet left in the beam model. In addition, the tests lead to the following conclusions:

- We can exclude a lack of convergence in the fitting procedure;
- The R2R variability is not related to data sampling;
- The measures are not sensitive to the choice of the angular threshold

This kind of analysis has an important role in the inter-calibration of different CMB experiments. In Figure 3.9 we compare Jupiter T_b averaged in each Planck/LFI band at the same frequency with the spectrum provided by WMAP. It must be noted that WMAP and Planck/LFI are calibrated using slightly different values for the dipole, as Planck/LFI assumes an amplitude of 3364.5 μK [2], while WMAP assumes an amplitude of 3355 μK [32]. In addition, WMAP central frequencies are different from Planck. WMAP measures are scaled and linearly interpolated to the averaged ν_{cent} of each Planck/LFI frequency channel. Furthermore, WMAP derives T_b assuming a Rayleigh-Jeans approximation of the Jupiter spectrum. This reduces Equation 3.4 to the simple product of T_{ant} for a factor $\Omega_{beam}/\Omega_{planet}$. Despite these considerations, the agreement is indeed quite good, with a difference which does not exceed 0.5%.

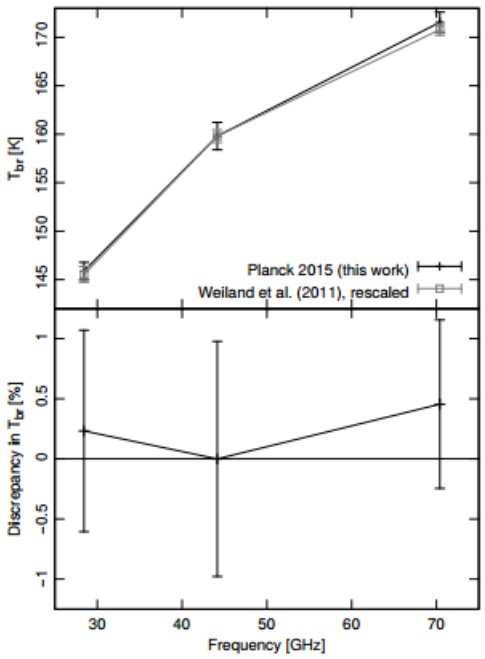

Figure 3.9: Top: brightness temperature of Jupiter (T_b) compared with the data from Weiland et al. (2011), linearly rescaled in frequency to match Planck/LFI central frequencies and corrected for thermal difference between Planck/LFI and WMAP dipoles.
Bottom: deviation from unity of the ratio between Planck/LFI estimate for T_b and Weiland et al. (2011). The agreement is excellent among the three frequencies.
Source: Planck 2015 [24]

3.4 Other planets

The same analysis can be performed on the other planets, taking into account that the SNR is not as high as it is for Jupiter. Jupiter is the only planet bright enough to be detected in the timeline without averaging on the different radiometers. On the other hand, averaging is needed for the other planets to enhanche the SNR, which is indeed quite low, expecially for Uranus and Neptune, in particular at 30 GHz. These planets, therefore are very sensitive to the confusion noise and the background, as reported in Table 3.2, showing the brightness temperature of Mars, Saturn, Uranus and Neptune, as reported in Planck 2013 results [33]. It must be considered that in this preliminary analysis different corrections have not been taken into account, such as the effect of the rings of Saturn or diurnal variability of Mars, due to the rotation of the planet.

Table 3.2: Brightness temperatures of planets. The first error represents the intra-transit difference, the second one the confusion noise [33].

Planet	T_b **[K] at 30 GHz**	T_b **[K] at 44 GHz**	T_b **[K] at 70 GHz**
Mars	$183.0 \pm 1.0 \pm 4.1$	$187.0 \pm 10.0 \pm 4.1$	$183.0 \pm 3.5 \pm 2.3$
Saturn	$121.0 \pm 3.5 \pm 0.9$	$128.0 \pm 3.0 \pm 1.0$	$131.0 \pm 2.5 \pm 0.5$
Uranus	$190.0 \pm 133.0 \pm 23.0$	$230.0 \pm 10.5 \pm 29.0$	$138.0 \pm 7.5 \pm 13.0$
Neptune	$79.0 \pm 5.0 \pm 74.0$	$74.0 \pm 22.0 \pm 76.0$	$101.0 \pm 11.0 \pm 32.0$

3.5 Lesson learned

The architecture of the Euclid end-to-end simulator reflects the lesson learned from the Jupiter analysis pipeline, in terms of software tools[2] and conceptual design. The most important inheritance of this pipeline is the idea of modularity, which is one of the key points of the simulator. The Jupiter analysis pipeline can be divided in three modules:

1 - Extraction of the Jupiter timelines;

2 - Fit to derive T_{ant} and, eventually, beam parameters;

3 - Calculation of T_b and application of photometric correction.

These three modules are independent from each other: the tests on the fitting method, for instance, are done at module 2 level, without influencing modules 1 and 3. This idea is one of the key points of the simulator architecture.

The I/O interface is another important inheritance of the Jupiter analysis pipeline, since both the Jupiter analysis and an end-to-end simulator deals with huge amounts of data and both the pipelines require an organized storing of the results and configuration parameters.

[2]Just to make an example, the fitting functions used to extract T_{ant} are the same used in the version 2.0 of the proto-E2ES to fit spectral lines.

Chapter 4

End-to-End Performance Simulators

End-to-End mission performance Simulators (E2ES) are tools which simulate the end-to-end performance of a mission, *i.e.* from the observed scene or object to the retrieved physical parameters. E2ES are used to support activities like:

- Assessment of the conceptual design and scientific preparation of the mission;
- Assessment of different system implementation options;
- Consolidation and fulfillment of technical and scientific requirements;
- Development of retrieval algorithms, higher-level products generation and data processing;
- Preparation and validation of instrument operations.

Once a mission is approved for implementation, such simulators can evolve to become supporting tools for the development and validation of the ground data processing.

An End-to-End mission performance Simulator can also be seen as a tool to support instrument operations. The simulation of synthetic data can also be used by scientists and engineers to consolidate the instrument configuration and to define operational strategies on such complex missions. Such simulator enables the generation of simulated output data for selected test scenarios to support the assessment of instrument configuration changes on the mission performance and to analyse the impact of such individual changes on the output of the system.

ESA is promoting several activities in order to reduce the re-engineering effort to generate E2E simulators, promoting reuse in the development of E2ES and to test the feasibility of a generic environment for Space Missions. One of these activities is supported within the ESA contract no. IPL-PTE/GLC/al/241.2014, in which a small team from "Universitá degli Studi di Trieste" is involved. This small team is composed by a supervisor, Anna Gregorio, and two Ph.D. students, Paola Battaglia and myself. I focus on the implementation and testing of the simulation pipeline, while Paola Battaglia is involved in the validation of the prototype.

This study develops along five steps:

1 Analysis of E2E simulators;

2 Requirements of an E2ES applied to the Euclid mission;

3 Definition of E2ES for Euclid;

4 Implementation of a prototype;

5 Validation of the prototype.

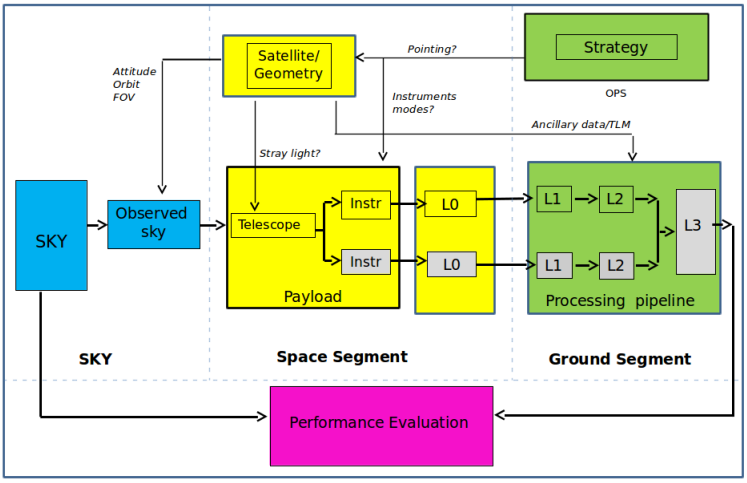

Figure 4.1: Generic high level reference architecture of an E2ES. Dealing with a space mission, modules can be divided in three blocks: Ground segment, Space segment and Sky. Once the observing strategy is defined, the simulated sky represent the input to the detection (telecope+instrument(s)) chain. The detected signal is then processed and compared with the simulated sky in order to assess the performance of the simulated observation./ *Credits*: Raffaella Franco, ESA-ESTEC, Netherlands

4.1 E2ES in space missions

E2E mission performance simulators are based on a reference architecture containing the basic modules for the simulator, providing the required flexibility to support extensive and evolutionary growth. Most E2ES are developed and used in Earth Observation (EO) programs (strongly driven by the fact that ESA is responsible for the instrument data processing), but there can also be a use for E2ES in space science and the framework, architecture and models defined in EO could be reused to a large extent.

Figure 4.1 shows a generic example of the reference architecture of an E2E simulator for a space mission. Each module covers a specific aspect of the simulated observation from the definition of an observing strategy to the extraction of processed data, going through the simulation of telescope optics and detection system.

Usually, the first release of the simulator is developed as a prototype tool to support the initial performance assessment of the mission in the early phases. For the E2ES to evolve and support the detailed mission design during later phases, its architecture has to allow growth along two possible directions. These two directions of potential growth are:

- Extensive growth, to include more effects and achieve a more complete simulation;
- Evolutionary growth, to achieve better accuracy in the simulator.

The rationale is to define a Reference Architecture that contains the basic modules for the E2ES, while providing the required flexibility to support both extensive and evolutionary growth. This, coupled to a simulator framework and a repository of models, will allow defining and implementing the E2ES faster and with less effort.

4.1.1 Criteria for Mission Categorization

In order to be in the position of defining a generic architecture suitable to different mission categories, and so apply this generic architecture to the specific case of the Euclid mission, it is necessary to perform a detailed review of past, current and planned space missions, in which such tools are commonly developed and used [34]. The following aspects, summarized in Figure 4.2, may affect the definition of the requirements and of a reference architecture for the E2ES:

- Number of satellites composing the mission. The fact that the mission consists of a constellation of two or more satellites instead of a single spacecraft may have an impact on the architecture of the E2E simulator. Dealing with a constellation means that we have to treat a system of systems: the behavior of each spacecraft must be simulated taking into account its synergy with the other components of the constellation. This is not the case of the Euclid mission, but different examples can be find of space missions involving more than one satellite, such as the solar observation mission STEREO (stereo.gsfc.nasa.gov) or the LISA mission (lisa.nasa.gov), dedicated to gravitational waves detection.

- Number of instruments on-board the spacecraft. The architecture of the E2E simulator will be definitely affected by the number of instruments on-board each satellite of the mission. There will be some architectural elements that will be unique and others will be specific of each instrument. This is true for Euclid in which the two on-board instruments are on the focal plane of the same telescope. Synergy between Euclid/VIS and Euclid/NISP must be taken into account since the beginning.

- Scientific objective of the mission. The scientific objective of the mission could be not unique. The mission could investigate one or more objectives and there is not a direct relation between the number of scientific objectives and the number of satellites or instruments on-board of a single spacecraft. Planck, for instance, investigated the same objective, the Cosmic Microwave Background, with the help of two instruments, while on Euclid each instrument is focused to investigate a specific cosmological probe (see Chapter 1), even if this anyway implies correlation between Euclid/VIS and Euclid/NISP observations.

- Orbit characteristics. It shall be investigated if the orbit characteristics impact the E2E simulator architecture. Orbit selection is constrained by the scientific objective of the mission and the instrumental setup. Euclid will orbit the Lagrangian point L2, like its predecessors WMAP, Planck and Herschel (see Chapter 2). In L2 Euclid will orbit the Sun together

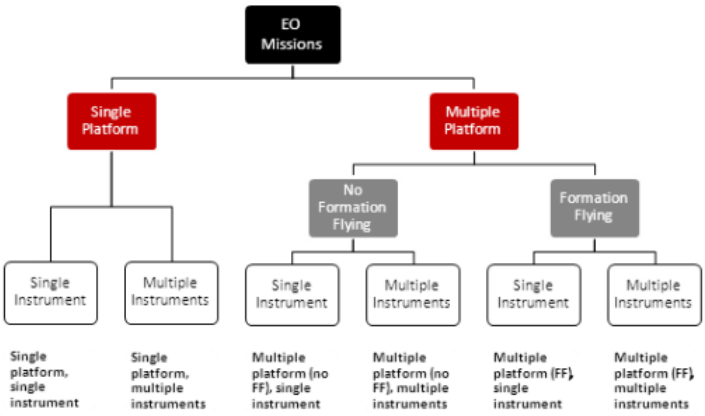

Figure 4.2: Categorization of EO Missions by number of satellites and number of instruments in the mission. In case of a generic space mission, this chart simplifies, since the multi-platform branch represents an unrealistic case. *Source*: GMV-ARCHEO-E2E-FR-001 Final Report [35]

with the Earth completing a revolution in one year. This means that for such an orbit we have to consider background sources that can vary on a seasonal scale, such as the Zodiacal Light.

- Observing Strategy. Depending on the instruments on board, but also on the scientific objective of the mission, it will be defined for the mission a determined observation strategy or scanning method. To cover the whole sky, the Planck satellite spun around its spin axis at ~ 1 revolutions per minute (rpm). In Euclid dithering is required to fill gaps between detectors. Simulating Euclid on-board instrumentation, a good knowledge of the dither pattern is required. Scanning methods provided directly by the instrument, like moving mirrors, are not considered in this categorisation.

It is also important to perform a detailed survey of the instruments flown on-board past, current and planned space missions in order to identify commonalities and define the optimum architecture for each case. In particular, those criteria that have an impact on the definition of the reference architecture have to be analyzed:

- Region of the spectrum at which the measures are taken;
- Passive vs active instruments;
- Scientific objective;
- Type of retrieval products;
- Calibration method;
- Scanning geometry.

The main differences between a space mission and an EO mission are the scientific objective, the calibration method and the scanning geometry. Typical objectives in EO missions are atmosphere, land, ocean, snow and ice, gravity and magnetic fields, while for Euclid, and for space missions focused on the large scale structure of the Universe, we have specific cosmological probes (see Chapter 1). Concerning the calibration, EO can have on-board or ground calibration, while in a space mission it is unrealistic the second case. Having different targets, it is trivial that the scanning geometry of an EO mission, looking at the Earth, is strongly different from that of a space mission, looking at deep space.

4.2 Euclid E2ES rationale

The implementation of a prototype Euclid E2E performance simulator has been supported by ESA contract IPL-PTE/GLC/al/241.2014. Scope of this contract is to make a feasibility study in order to create an E2E simulation environment similar to that already present for EO missions for a generic space mission.

The Euclid mission represents a suitable test case. As described in details in Chapters 1 and 2, Euclid represents a very complex mission, both from a scientific and a technical point of view. Due to the complexity of the Euclid mission an E2ES is highly desirable to test performance of the on-board instrumentation and Euclid scientific capabilities. Different groups on Euclid are working in this direction and the "Euclid E2E Performance Assessment" is one of the activities led by the Euclid Consortium. The work in this sense is aimed at defining and setup a simulation environment to assess the scientific performance of the Euclid mission and its final data products.

An End-to-End mission performance simulator can also be a tool to simulate test scenarios in order to assess the mission performance as a function of changes in the instrument configuration and to analyse possible error sources. Euclid instruments, NISP and VIS, are operated by the Instrument Operation Teams (IOTs), which shall play a crucial role in the successful execution of the Euclid mission; they are in charge of the monitoring, control and maintenance of the Euclid payload, from initial diagnostics of field quality to detailed trend analysis of instrument characteristics and calibration. The IOTs will be equipped with dedicated software tools to allow a quasi-automatic monitoring and manage operational activities. An End-to-End mission performance simulator can be a mandatory tool for the IOTs to assess the mission performance according to instrument configuration.

In its full version, the proposed Euclid E2ES is designed to include, both the NISP and VIS instruments. This will allow assessing the synergy between the two instruments, the observation strategy and the operations. Nevertheless, given the complexity of the Euclid mission, this work is aimed at a very specific science case: spectroscopic redshift determination for galaxy clustering, fundamental to BAO analysis (See Chapter 1). This will be achieved by simulating only the Euclid/NISP-S detection system and corresponding optical system.

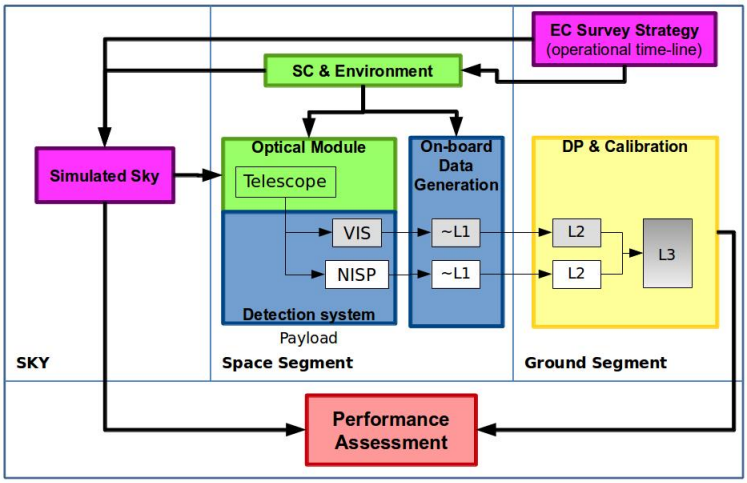

Figure 4.3: Euclid E2ES high level architecture scheme. Magenta modules represent the sky simulation (ECSS and SS). Green represents the spacecraft and telescope environment (SCE and OM). Light blue modules refer to the instrumental environment (DS and OBDG). Yellow represents the ground based environment (DPC), while red refers to the performance assessment (PA).
Source: Euclid E2E Design Definition [36]

4.3 Euclid E2ES Architecture

The proposed high-level architecture for the E2ES, described in this Section, is based on the global system description reported in the ESA internal reports: *EUCLID E2E Requirement Baseline* [37] and *EUCLID E2E Design Definition* [36].

The resulting scheme of the simulator level architecture and main components are shown in Figure 4.3. The structure of the simulator is modular, so that the different components of the simulator remain unaffected by required improvements or changes in one of the modules. Thanks to its modular structure, the simulator allows the user to run not only the whole chain, but also one or some of the modules, accordingly to his/her purposes. Eight different modules, shown in Figure 4.3, are defined:

1. Euclid Survey Strategy (ECSS): it defines an observing strategy according to the scientific scenario to investigate;
2. Simulated Sky (SS): it simulates a given region of sky according to the defined survey strategy;
3. Spacectaft and Environment (SCE): it handles the attitude of the S/C and its orbital status during the operations foreseen by the simulated survey strategy;

4. Optical Model (OM): it provides an optical model to be convolved with the simulated sky, taking into account possible attitude modifications;
5. Detection System (DS): it simulates the behaviour of the on board instrumentation and the effects of the detection chain;
6. On-Board Data Generation (OBDG): it handles the telemetry (both instrumental and S/C housekeeping) data and the on-board data compression;
7. Data Processing and Calibration (DPC): it runs a simplified version of the ground-based data processing pipeline;
8. Performance Assessment (PA): it checks the good functioning of the whole E2ES, comparing the input of the simulation chain, *i.e.* the simulated sky, with the output of the simulator.

The colour code is meant to divide the different modules in logical macro-areas. Magenta modules represent the sky simulation (ECSS and SS); green represents the spacecraft and telescope environment (SCE and OM); light blue modules refer to the instrumental environment (DS and OBDG); yellow represents the ground based environment (DPC), while red refers to the performance assessment (PA).

The high-level architecture is designed considering two different versions of the simulator: a prototype version, called proto-E2ES, described in detail in Chapter 5, and a complete version, the full-E2ES. The full-E2ES, which is thought to include both the Euclid NISP and VIS instruments, will be able to assess the synergy between the two instruments embarked on the mission, the observation strategy and the operations. The proto-E2ES has reduced features, is limited to spectroscopic simulations (NISP-S) and the modules are thought to be implemented in a simplified version, avoiding all the housekeeping data generation and, as a consequence, implementing the calibration chain in a simplified way.

4.3.1 General description

Given a scientific scenario, in the ECSS module the observing strategy is defined by means of an operational time-line. The operational time-line contains all the information about the planned observation sequences: the pointing coordinates, VIS and NISP exposure times, in agreement with the scanning time-line described in Section 2.3 and, in the NISP spectroscopic channel case, the spectral band in which the user wants to perform his/her simulation (Y, J or H). The operational time-line is meant to store also attitude parameters, such as the Solar Aspect Angle (SAA) of the satellite[1] and, since the Zodiacal Light Emission (ZLE) is one of the main contaminant for Euclid, the parameters needed for a ZLE simulation, such as the reference wavelength of the ZLE or the spatial (elongation) and temporal (days) ranges of the ZLE simulation. The operational time-line is designed to take into account the fact that Euclid observes the sky in two different ways: Wide Survey and Deep Survey. These two approaches are slightly different

[1]SAA is defined as the angle between the pointing direction and the vector to the Sun.

and require a different study of the observation strategy. The pointing sequence can be studied to mimic both the approaches.

The SS module is meant to provide a simulated region of sky, which is the main object of the simulated observation. The simulated sky is represented by catalogs of sources. The source catalog must contain the spatial coordinates and additional parameters related to the nature of the source, point-like or diffused, such as, for instance, the half-light radius of the source[2]. This module is meant to handle the simulation of possible background or foreground sources, focusing on ZLE as a major contaminat. On the catalogs, the simulator observes sky regions within a VIS or NISP field of view, taking as input pointing coordinates and exposure times from the ECSS operational time-line.

The SCE module simulates the attitude and control system and deals with micro-disturbances that can affect the pointings and can bring to thermal or mechanical perturbations on the payload. This module deals with telemetry and housekeeping. Attitude parameters are stored in the ECSS operational time-line.

Telescope and instruments optics are handled by the OM module. This module provides an optical model to be convolved with the simulated sky. The optical model is parametric: the values of the optical parameters, such as the Point Spread Function (PSF) or the Encircled Energy (EE) radius of the instruments, as designed for the mission, are stored in a configuration file, which is the input of the DS module. Deviations from ideal optics are treated modifying the values of the parameters via transfer functions. This module is strictly linked to the Euclid mission database and it is meant to evolve together with the mission database itself.

Catalogs from the SS module, together with the information contained in the ECSS operational time-line and the OM configuration file are the input of the DS module, which simulates the effects of the detection chain, *i.e.* the behaviour of the detectors. This module is split in two different chains: one for the VIS instrument and one for NISP. The NISP chain is divided in two sub-chains: NISP-P for the photometric simulations and NISP-S dealing with spectroscopy. This module treats instrumental noise and systematic effects, the readout and the instrumental timescales such as the opening/closing of the dithers and the exposure times.

A complete simulation of the on-board data generation is beyond the scope of an E2ES for performance assessment. For that reason the OBDG module is meant to simulate only simplified data structures, if required for the E2ES purpose. The module is split in two different chains: the housekeeping data chain and the science data chain. The housekeeping chain takes input data directly from the SCE as the housekeeping data are not affected by the optical environment and the detection system. The science data chain handles the proper scientific data and the housekeeping of the instruments. Not all the telemetry will be simulated. The OBDG should also handle the compression of data. Data compression for Euclid is mostly lossless and no major problems due to decompression of data

[2]The half-light radius of a galaxy is the radius at which half of the total light of the system is emitted.

are forseen. For that reason compression will not be implemented neither in the proto-E2ES nor in the full-E2ES.

The DPC module simulates the ground-based data processing and calibration. It takes simulated high level data from the DS and provides, as an output, processed data. Satisfying the calibration requirements corresponds to simulate a set of calibration observations and this is beyond the scope of an E2ES. For that reason, calibration in this module is treated in a simplified version. Instrument calibration, the measurements required for characterizing the response of the instrument response, makes use of data from ground-based tests and in-orbit measurements, such as the science frames themselves, dedicated calibration observations, and exposures of the onboard calibration source. These kind of measurements are out of the scope of the E2ES and are not considered. Processed data are then used by the PA module.

The PA module is meant to control the good functioning of the whole E2ES, comparing the input of the simulation chain, *i.e.* the simulated sky from the SS, with the output of the simulator. It takes the final product of the simulation chain and checks that these products fulfill the desired requirements, given defined metrics or a defined figure of merit. The performance assessment definition depends on the final goal of the E2ES, mainly on the science case considered for the specific simulation and cannot be defined in general. Taking the proto-E2ES as an example, the redshift measurement is the main parameter to be used for the performance assessment and to be compared with the input value given by the catalog. In the proto-E2ES case the other main scientific parameters to be used for the comparison with the input values (catalogues) are:

- Completeness, defined as the fraction of spectra measured above a given line flux limit;
- Purity, defined as the fraction of spectra correctly measured above a given line flux limit;
- Redshift errors and detection limit.

A summary of the eight different modules, together with their input and output files and parameters, is reported in Table 4.1. In the same table, the modules not implemented in the prototype are shown. A detailed description of the prototype version of the simulation is given in the next subsection.

4.3.2 Proto-E2ES

The Euclid E2ES simulator prototype has reduced capabilities with respect to the full version. As reported in Table 4.1, the Spacecraft & Environment, Optical Model and On-Board Data Generation modules are not implemented in the prototype. SCE and OBDG modules deal with telemetry and housekeeping,

Table 4.1: Summary of the eight modules of this E2ES.

Module	**Input**	**Output**	Proto-E2ES
ECSS	None	Operational time-line	yes
SS	Operational time-line Catalogs	TIPS compliant catalogs	yes
SCE	Operational time-line	Attitude parameters	no
OM	Attitude parameters	Optical parameters	no
DS	TIPS compliant catalogs Optical parameters	Slitless images	yes
OBDG	Attitude parameters	Telemetry	no
DPC	Slitless images	Final products	yes
PA	Catalogs Final products	Performance assessment	yes

that are not created by the prototype pipeline. The optical and instrumental setups are left to the Euclid/NISP simulator, TIPS, and a dedicated OM module has not been implemented yet. Possible operations on the optical model are left to some tests, described in Chapter 6. Below, it is described how the general architecture is implemented in the prototype pipeline [38].

The Euclid Survey Strategy module defines, through a given operational time-line, an observing strategy according to the scientific scenario to investigate. The operational time-line contains information on the pointing coordinates and exposition times.

The Simulated Sky module uses the information contained in the operational time-line to simulate, through source catalogs, a given region of sky according to the defined survey strategy.

The simulated sky is the input of the Detection System module, which simulates the behaviour of the on board instrumentation and the effects of the detection chain. In a future versionIn the proto-E2ES the simulation focuses on the NISP instrument alone. At this point the simulation of the space segment ends.

The output of the DS module are given to the Data Processing and Calibration where the simulator runs a simplified version of the ground-based data processing pipeline, providing wavelenght and flux calibration of the spectra through parametric functions.

At the end of the simulation chain, the Performance Assessment module checks the good functioning of the whole E2ES, comparing the input of the simulation chain, *i.e.* the simulated sky, with the output of the simulator. Furthermore it takes the final product of the simulation chain and checks if the mission requirements are fulfilled.

Chapter 5

Euclid E2ES Prototype

The Euclid E2E performance simulator is implemented and tested in a prototype version. This simplified version provides a basic but representative E2ES simulation focused on infrared spectroscopy and in particular on redshift measurements. The spectroscopic redshift parameter is one of the observables required to study one of the main Euclid cosmological probes: the *Baryonic Acoustic Oscillations* (BAO), described in detail in Subsection 1.5.2.

Two different versions of the proto-E2ES are implemented: a preliminary version, the proto-E2ES_v1.0, and a more mature version, proto-E2ES_v2.0. The version 1.0 of the prototype is the tool delivered to ESA as one of the final products of the work supported by contract IPL-PTE/GLC/al/241.2014. The second version closes a major software issue and is meant to be compliant with the software framework designed for Euclid. Furthermore, version 2.0 provides a more efficient and organized I/O interface, crucial for the modular design of the simulator.

5.1 Goals of the prototype

The reference architecture described in Chapter 4 is designed considering the whole simulation chain needed by Euclid. Nevertheless, the effort needed to implement a complete version of the simultor is demanding in terms of people and time. For this reason, this work is meant to be a preliminary study to assess the feasibility of such a tool. The proto-E2ES is aimed at a very specific science case, the spectroscopic redshift determination for galaxy clustering, by simulating only the EUCLID/NISP-S instrument.

The activity on the prototype is succesfully, since the simulator passes all the criteria reported in the *EULCID E2E Verification and Validation Plan* [37]. Scope of this document is to propose a set of test cases, repoted in the, to be simulated with EUCLID E2E in order to:

- Perform a software verification of the simulator. The goal of the software verification plan is to check the consistency and meaningfulness of the produced outputs along the entire simulation chain;
- Perform a scientific validation of the simulator. The goal of the scientific validation is to determine whether or not the simulator software complies with the scientific requirements established in the *Euclid E2E Requirements Baseline* document ([37]).

The prototype activity represents the first step towards the implementation of a full version of the simulator. The reference architecture proposed in this work, containing the basic modules for the simulator, provides the required flexibility to support extensive and evolutionary growth and allows defining and implementing the full-E2ES faster and with less effort.

The proposed operational usage of the E2ES imposes some requirements that are mostly linked to the reaction time. Implementing a complete Euclid simulation,

we must consider this possible usage: some modules, especially the optical model, shall be implemented accordingly. Implementing complex optical codes based on ray tracing is time demanding and not acceptable. Also the On Board Data Generation and the Data Processing modules should be simplified in order to optimize the amount of data to be managed and as a consequence the simulator processing time.

5.2 Proto E2ES v1.0

The first version of the prototype consists in a Python script, wrapping a set of dedicated Python libraries and three main different external software codes:

- **TIPS**: a simulation tool which produces the expected images of an observation for a given instrument. It is able to simulate the 16 detectors of the spectrometer of the EUCLID/NISP instrument;
- **aXe**: a software designed to extract spectra in a consistent manner from slitless spectroscopy images. It was designed for the Wide Field Camera 3 (WFC3) and the Advanced Camera for Surveys (ACS), which were installed on the Hubble Space Telescope (HST).
- **IRAF**: the Image Reduction and Analysis Facility. It includes a good selection of tool for general image processing and graphics, plus a large number of codes for the reduction and analysis of optical and IR astronomy data.

The code is open source, under the terms of the *GNU Lesser General Public License*, and can be downloaded from a Bitbucket repository.

At the beginning of the simulation, the environment must be configured to allow the script to find all the dedicated libraries and to allow the correct functioning of the external dependences. A dedicated file is provided in order to set the correct paths to the external libraries and to properly set IRAF configuration [39].

5.2.1 Description

The first step of the proto-E2ES_v1.0 working flow is to read the global configuration file (GlobalParameters.dat). In this version the global configuration file name is hardcoded, together with the operational timeline and the log file names. The configuration file contains the catalog and configuration file names, the storing directory name and some configuration flags to tell to the simulator which module to run. Once the configuration parameters are loaded, the simulator cleans, if selected, previous simulations, in order to avoid spourius output.

The proper simulation starts reading the pointing data. This is performed by the ECSS module, which exctracts from the operational timeline file (OperationalTimeline_lite.csv) the pointing index (a progressive integer number, starting from 1), the pointing coordinates (right ascension and declination) and the exposure time. Even if a zodiacal light simulation is not integrated in version 1.0, the operational timelines contains also parameters to simulate the Zodiacal Light Emission (ZLE), such as central frequencies, spatial (minimum and maximum elongation) and temporal (minimum and maximum day) coverage of the ZLE simulation.

The SS module is implemented in a simple version. It takes an input catalog and creates a TIPS-compliant version of the same catalog. TIPS requires both photometric and spectral data of the input sources. Two different input methods are allowed:

1 - Photometric and spectral catalogs;

2 - Coordinates catalog with thumbnails of images and spectra.

The SS module is designed to use both these input methods. The test catalog used in this work is designed to be read with the second method.

The TIPS-compliant catalog is interfaced, together with a TIPS configuration file, with the DS module, aimed to run the TIPS simulation.TIPS simulates a Euclid/NISP Field of View (FoV), given the pointing coordinates and exposure time. The TIPS configuration file contains the optical and instrumental parameters and it is meant to be the input file to the OM module in future versions of the simulator. Euclid/NISP focal plane consists of 16 detectors. For each detector TIPS simulates four dithers, according to the defined Euclid observing strategy. Each TIPS simulation produces 16×4 slitless images.

For each slitless image simulated by the DS module, the first step of the DPC module is the spectra extraction. This is done via the external software aXe[1]. Three input files are required by aXe:

- The slitless image;
- A configuration file, containing the instrumental configuration;
- A data file, containing the coordinates and some information on the sources, such as dimension, orientation and magnitude.

For each slitless image, aXe provides as output a list of spectra, one for each source identified in the image. For each source, the spectra of the four dithers are combined (averaged) and saved in an IRAF compliant format[2]. For each combined spectrum, IRAF identifies the spectral lines, then a very simple algorithm treats

[1]Since few aXe functions are required, the simpliest solution adopted, to avoid difficult installation procedures and ensure the software scalability, is to use the executables of those functions.

[2]Since it is quite old, IRAF is not very elastic from the point of view of the I/O.

each line as an Hα emission and a list of possible z of the spectrum is given. The error on z is given by propagation of the error on λ:

$$\sigma_z = \frac{\sigma_\lambda}{\lambda_{rest}} \tag{5.1}$$

where σ_λ is given by the FWHM of the best fit profile on the emission line. The redshift extraction algorithm makes also a cross-check on a list of reference lines, which can be given in an auxiliary file, in order to give a rough estimation of the real redshift. For each z, the reference lines are shifted to that value and compared with the list of detected lines. In principle, the z related to the most matches should be considered the more reliable redshift for that source. Since this is a quick and rough method, the redshift extraction algorithm still not allows us to assign a good reliability level to each measured z.

The last step is to display the simulation results. This is done by the PA module, which gives a visual representation of the results and computes some statistics which are compared with the mission requirements. The PA module yields the following parameters:

- Completeness: the ratio between the detected sources and the total number of sources in the simulated pointing;
- Purity: for a given z, it is the ratio between the number of sources and the number of detected sources;
- Redshift error: maximum, minimum and mean.

A source is considered detected if at least one spectral line is identified in its spectrum.

In some spectra just one spectral line is identified. In this cases the sources are related to a single redshift measure. We monitor the number of these sources to monitor the behaviour of the subset of the sources related to just one redshift measure.

5.2.2 First results on test scenario

The simulator is tested on a very simple catalog, in order to check the behaviour of the simulator pipeline. Such a simple test scenario does not represent a realistic case, but allows, thanks to its simplicity, to make a basic but representative simulation in order to test the correct functioning of the different modules. The test catalog consists in 320 copies of the same source of magnitude $m = 15$ and redshift $z \simeq 1.324$. The sources are distributed in a regular pattern as shown in Figure 5.1 and labeled by a sequential source ID number from 1 (the lower-left source in the pattern) to 320 (upper-right). The full test catalog described above is covered by four different pointings:

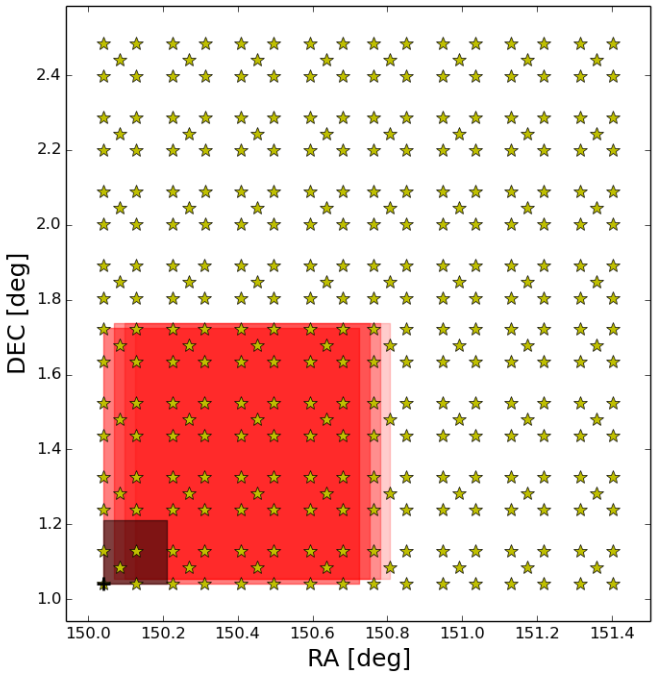

Figure 5.1: Structure of the simple test catalog used as input of the proto-E2ES_v1.0. The catalog consists in 320 sources, distributed in a regular pattern, all at the same redshift, $z = 1.324$, and at the same magnitude, $m = 15$. The black cross represent the pointing reference pixel (lower-left), the dark box represent a single detector FoV, while the red boxes represent the full detector array FoV, one for each dither.

- Pointing 1: RA = 150.04°, DEC = 1.04°;
- Pointing 2: RA = 150.72°, DEC = 1.04°;
- Pointing 3: RA = 150.04°, DEC = 1.76°;
- Pointing 4: RA = 150.72°, DEC = 1.76°;

The pointing coordinates represent the [0,0] pixel of the output image, *i.e.* the lower-left pixel. In Figure 5.1 the case of pointing 1 is shown: the black cross in the lower-left corner of the dark box represents the pointing coordinates, RA $\simeq$ 150.04° and DEC $\simeq$ 1.04° in this case; the dark box represents the FoV of a single detector, here detector 00; the four red boxes represents the full Euclid/NISP FoV during the observation. Each red box represents a different dither. The same scheme stands for pointing 2, 3 and 4.

Being clones of the same source, objects in the test catalog have the same spectrum, shown in Figure 5.2. The sample spectrum presents three lines at

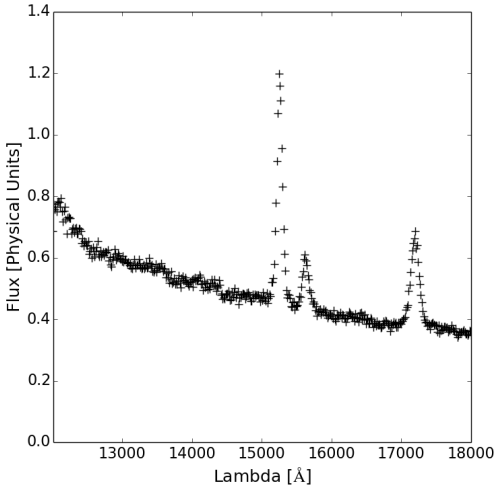

Figure 5.2: An example of the spectrum of one source in the test catalog. The spectrum presents three lines at 15252, 15665 and 17212 Å, which means that, ideally, three redshift measures (1.324, 1.387 and 1.623) are expected.

nearly 1525.2, 1566.5 and 1721.2 nm (15252, 15665 and 17212 Å). Each line is treated as an Hα line of the Balmer series, commonly used to measure the redshift parameter z, with a wavelength of 656.28 nm at rest. These three lines lead to redshift 1.324, 1.387 and 1.623 respectively. In the ideal case, for each source in the input catalog, the simulator shall provide these three redshift values as a result. The line at $\lambda \simeq 1525.2$ ($z \simeq 1.324$) is the real Hα line.

A simulation on the whole test catalog provides the following results:

- Completeness: 0.82
- Purity: 0.77
- $\sigma_{z,min}$: 0.002
- $\sigma_{z,max}$: 0.017
- $\sigma_{z,mean}$: 0.005

Statistics on the identified lines are reported in Table 5.2, in which we compare results of this version of the simulator with the results of an improved version, proto-E2ES_v2.0, described in Section 5.3.

A completeness of nearly 82% means that the great majority of the sources in the catalog is processed and leads to a redshift measure. This can be seen also in Figure 5.3, where the detected sources are denoted by crosses, colored according to the different pointings. The mission required value for completeness is 45% [43]. The mission requirement is tuned on the fact that Euclid aims at

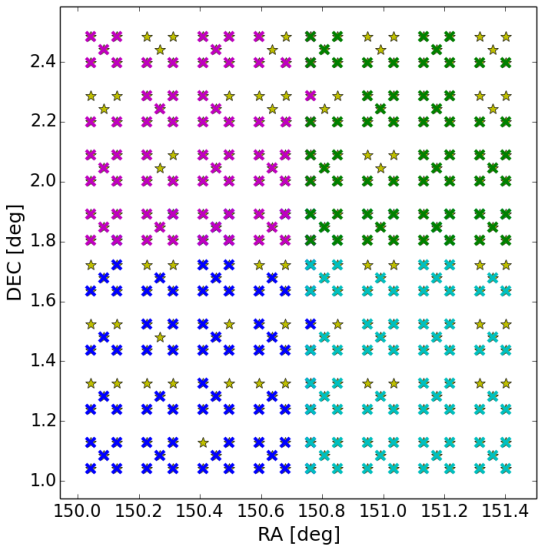

Figure 5.3: Sources detected by the simulator. The yellow stars are the sources in the catalog, the coloured crosses show the sources detected during the simulation. Each color represent a different pointing.

observing sources down to magnitude $m \simeq 24$, while sources in the test catalog have $m \simeq 15$. The high value obtained for the completeness parameter reflects the fact that we are considering a catalog of bright sources.

On the detected sources, we obtained a purity of nearly 77%, which is less than the required value of 80% [43]. Since the z extraction algorithm is still not able to assign a reliability value to the measured z of each source, purity is computed considering all the sources in which one of the identified lines corresponds to the real Hα line.

Results on the measured z are summarized in Figure 5.4, where the measured redshift parameters of each source are plotted versus the source ID numbers. It can be noted, that the line at $\simeq 1525.2$ nm ($z \simeq 1.324$) and the line at $\simeq 1721.2$ nm ($z \simeq 1.623$) are detected for the majority of the sources. This is not true for the line at $\simeq 1566.5$ nm ($z \simeq 1.387$), which is the faintest of the three. The scattered regions are due to spourious detections, which the algorithm is still not able to identify and remove. In the zoomed lower panel, showing the correct Hα line, we can note that the measured values are slightly higher than the input catalog value (red line in figure). This is probably due to how IRAF identifies the spectral line and, being a black box, we cannot further analyse any possible systematic error in this version of the simulator. The residual value, with respect to the reference value of $z \simeq 1.324$ is always below the 0.3%; nevertheless, a better control on the line identification algorithm is needed to avoid this systematic effect. This point is closed by the substitution of IRAF with a dedicated algorithm we developed (see Subsection 5.2.3).

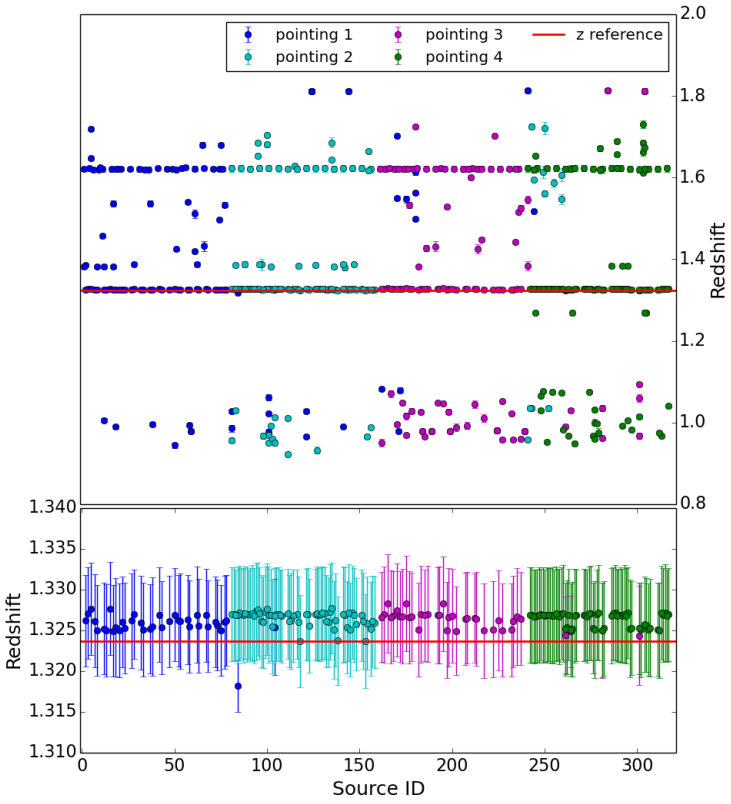

Figure 5.4: Top: redshift values measured for each source. The red line represents the reference redshift $z \simeq 1.324$. The correct value is measured in nearly every detected source.
Bottom: zoom on the correct values.

The 45% of the total detected sources corresponds to a single redshift measure. We compute the fraction of sources of this sub-sample related to each one of the redshift parameters related to the three spectral lines of our sample spectrum (1.324, 1.387 and 1.623). All the measures not related to one of these values are labelled as spurious. The best interpretation of these spourious values is that of false positives, left by the aXe spectral extraction, and then detected by IRAF. Since aXe represents a black box we cannot perform a finer analysis of this issue. Replacing aXe with a dedicated spectral extraction algorithm could lead to a better understanding of this feature. The replacement of the aXe software tool with a dedicated one is indeed one of the improvements foreseen for the future (see 5.2.3).

We summarize the results as follows:

- Fraction of sources related to a measure $z = 1.324$: 0.65;
- Fraction of sources related to a measure $z = 1.387$: 0.00;
- Fraction of sources related to a measure $z = 1.623$: 0.30;
- Fraction of sources related to a spurious measure: 0.05.

Most of the single redshift sources are related to the reference redshift. The value of 1.387 is never measured. This is probably due to the fact that the simulator misses the weakest spectral line. Just the 5% of the single redshift sources are related to spurious measures.

In this version of the simulator, the redshift error σ_z is computed by propagation of the error on the corresponding identified line σ_λ. This means that error on redshift contains the contribution of each contamination responsible for a spread in the spectral line. Since sky simulation and spectra extraction strongly depend on external software codes (TIPS and aXe), that represent black boxes on which we do not have a direct control, we cannot make second order corrections like we did, for instance, on the Jupiter flux analysis to improve the R2R deviation (Color Corrections, Band Average correction, see Chapter 3). Redshift error σ_z can be seen as an upper limit on the uncertainty of the redshift measurement. As a further development, with more control over the software components, a more detailed analysis of possible error sources could help in having a better redshift error evaluation and reach a value of the effective σ_z closer to the mission requirements.

5.2.3 Open points and issues

The first version of the proto-E2ES shows a series of open points and issues, which has been taken into account in order to upgrade the simulator to the proto-E2ES_v2.0:

- New test catalogs. The catalog used in the test scenario represents a very simple case. this has been useful during the implementation phase, since such a simple not realistic scenario allows a good control of the correct functioning of the different part of the simulator. It is trivial that a more realistic scenario must be taken into account and the simulator must be tested in more complex cases using wider catalogs, with a more realistic source distribution.
- Zodiacal Light (ZL) simulations. Zodiacal Light is the major contaminant at Euclid/NISP wavelengths. The ZEUS (Zody EUclid Simulator) package allows the integration of time dependent contamination from Zodiacal Light inside Euclid survey optimization codes which are designed for a static sky model [46]. The integration of this tool in the proto-E2ES is forseen in future versions of the prototype. Some preliminary work in this sense is reported in Subsection 6.2.1.

- Create transfer functions for the optical parameters. This is crucial expecially if the simulator is going to be used to define instrument operations.
- Persistence tests. Image persistence occurs whenever a pixel is exposed to light that exceeds more than about half of the full well of a pixel in the array. Persistence can occur within a single visit, as the different exposures in a visit are dithered, which is the Euclid scanning strategy case.
- Substitution of the software black boxes IRAF and aXe. The majority of the operations of the DPC module are done by two external software codes of which we do not have a complete control. In addition to that one of the goals of this work is to create a software which is compliant with the Euclid software environment. Neither aXe nor IRAF are part of the Euclid environment. Since aXe is run via a list of already compiled executables and being the extraction of spectra from a slitless images a very complex procedure, the substitution of aXe does not have a high priority. On the other hand, IRAF substitution priority is high, since a few IRAF functions are used and the effort to integrate this software in the pipeline is higher than the benefits.
- Improve the z extraction algorithm, in order to have an esteem of the reliability of redshift measures.
- Improve the PA module, implementing a better visualization of the results and improving our control on the measured parameters and their statistical meaning.

The open points and issuses arised from the proto-E2ES test are summarized, together with their priority level, in Table 5.1.

Table 5.1: Open issues of the protoE2ES_v1.0 and their priority level.

Issue	**Priority**	**Module**
Catalogs	High	SS
ZEUS integration	Medium	SS
Transfer Function	Medium-High	OM
Persistence	Medium	DS
IRAF	High	DPC
aXe	Low	DPC
z measure	Medium-Low	DPC
Better perfomance assessment	Low	PA

Some points, such as the usage of more realistic catalogs has not been treated in this work, despite of the high priority. This is due mainly to the fact that, since a quite big amount of work is required in order to integrate this point in the software pipeline and a catalog data model common to all the Euclid simulation groups is not yet defined, we preferred to focus on the line identification, which is mandatory for redshift measurements. For this reason, the highest priority has been assigned to the substitution of IRAF with a new algorithm in order to have a good control of the line identification.

Other issues are strictly linked to the progress of the whole mission implementation, such as the work on persistence and transfer functions, which requires more detailed information at mission database level, which are not available yet. The same holds for ZEUS, which is still under development. These points cannot be solved independently, but some tests has been made in order to propose possible solutions (See Chapter 6).

The open issue on aXe has a low priority, since spectra extraction seems to work well, even if aXe represent a black box and we do not have total control on its operations. Low priority is also assigned to the PA improvement, since it follows straightforwardly the implementation of a more mature simulation chain.

5.3 Proto E2ES v2.0

Version 2.0 of the proto-E2ES consists in a more mature version of the prototype, from the point of view of the software architecture. The main improvement of version 2.0 is the substitution of the IRAF software with a dedicated algorithm aimed at the spectral line identification. This closes one of the major issues of the version 1.0 and removes one of the software black boxes present in the previous version. Furthermore, the file structure has been reorganized and the input-output (I/O) interface has been reviewed from version 1.0 to version 2.0 in order to make the simulator compliant with the software framework defined for Euclid and with the Euclid coding rules.

The global configuration file has been redesigned in xml format. This allows us to have more information, such has descriptions of the configuration parameters and comments on their usage. In addition, not only the I/O file names can be configured, but also their path, allowing a complete control of the data flow of the simulator. The output products storage has been redesigned in order to store a smaller number of output files with more information for each file. Furthermore, the new algorithm allowed to rewrite the I/O interface of the DPC module, needing less intermediate products and implementing a more linear data flow with respect to the one required by IRAF. The environment settings are unchangend from the point of view of the user [42], but now the script provides just the correct paths to the external dedicated libraries, since IRAF is no more integreted in this version of the simulator.

The new line identification algorithm implements a simple procedure to identify and fit the spectral lines. The procedure can be divided in five main steps:

- Load the input spectrum;
- Perform a fast smoothing of the input spectrum;
- Calculate the derivative of the input spectrum (point by point);
- Select the spectral peaks via maxima selection over an adaptive threshold;
- Perform a Gaussian fit in a 20 pixels window centered on the peak position.

The algorithm takes as input spectra extracted from TIPS slit-less images by the aXe software. On the input spectrum the algorithm performs a smoothing in order to reduce the effect of the noise, applying on the spectrum a moving average filter. It operates averaging a number of points from the input signal to produce each point in the output signal as follows:

$$y_i = \frac{1}{N} \sum_{j=-(N-1)/2}^{(N-1)/2} x_{i+j} \tag{5.2}$$

Where x_i is the input signal, y_i is the output signal, and N is the number of points in the average. The algorithm performs a 3-points moving average smoothing, *i.e.* Equation 5.2 simplifies to:

$$y_i = \frac{x_{i-1} + x_i + x_{i+1}}{3} \tag{5.3}$$

The algorithm looks for the maxima of the smoothed spectrum taking the derivative of the smoothed spectrum itself and looking for which points the sign of the derivative changes from positive to negative. Maxima are selected only above an adaptive threshold in order to ensure that the selected maxima are good candidates to be flux peaks. To set the threshold the algorithm performs the following operations:

- Selects the points below the spectrum mean. For semplicity let us call this sub-sample $S(<)$;
- Performs a linear fit on $S(<)$ to identify the slope of the sample;
- Selects peaks only where the difference between the spectrum and the fitted slope is greater than the standard deviation of $S(<)$.

The algorithm provides a list of selected peaks and performs a Gaussian fit within a window of twenty pixels centered on the peak position. The Gaussian profile used for the fit is of the form:

$$G(x) = f \exp\left(-\frac{(\lambda - \lambda_c)^2}{2\sigma_\lambda^2}\right) + bkg \tag{5.4}$$

For each spectral line the fit provides the line central wavelength λ_c, the line peak flux f and the line sigma σ_λ. Results on a test spectrum are shown in Figure 5.5. For each line of the spectrum the red dot is the point (λ_c, f) representing the peak position and flux. In red, the best Gaussian fit on each line is reported.

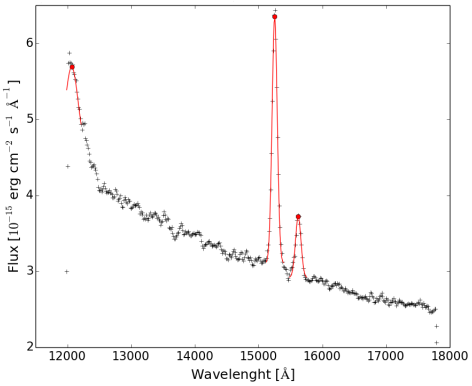

Figure 5.5: Results of the new algorithm on a test spectrum. In red the Gaussian fit of the identified emission lines. Red dots represent peak positions and fluxes. For each line, the best-fit Gaussian is reported.
Source: Gregorio et al. 2016 [38]

5.3.1 Results on test scenario

The proto-E2ES_v2.0 has been tested on the same test scenario of the proto-E2ES_v1.0. A simulation on the whole test catalog provided the following results:

- Completeness: 0.99
- Purity: 0.90
- $\sigma_{z,min}$: 0.003
- $\sigma_{z,max}$: 0.013
- $\sigma_{z,mean}$: 0.007

The differences of the values of the output parameters with respect to the first version can be ascribed to a better line detection of the new algorithm with respect to IRAF. A completeness of 99% means that basically all the sources have been correctly detected during the simulation, which is auspicable since the 320 sources in the test catalog are clones of the same test source. Purity has increased accordingly to the 90%, above the mission requirement, taking into account that we are dealing with very bright sources in this test.

The new detection line algorithm seems to provide a better detection of the line at $\simeq$ 1566.5 nm ($z \simeq 1.387$), which now is detected for the majority of the sources, as shown in Figure 5.6 comparing the results of the proto-E2ES_v1.0 (cyan dots) with the results of the proto-E2ES_v1.0 (black points). We have less sources in which just one line is identified. The number of single redshift sources drops to the 19% of the total detected sources. However, the statistics on this sub-sample of data changes with respect to the version 1.0:

- Fraction of sources related to a measure $z = 1.324$: 0.17;
- Fraction of sources related to a measure $z = 1.387$: 0.20;
- Fraction of sources related to a measure $z = 1.623$: 0.00;
- Fraction of sources related to a spurious measure: 0.63.

Most of the sources, 63% are related to spurious measures, while just a 17% of the sources are related to the reference redshift. On the other hand, the value 1.387 is now measured, in agreement with the general behaviour of the new algorithm, which provides a better detection of this line, as shown in Figure 5.6.

The new algorithm shows a good behaviour also if we consider the "correct" line at $\simeq 1525.2$ Å ($z \simeq 1.324$), which shows a more accurate detection with a negligible deviation from the catalog value. Furthermore, the scattered regions between the detected lines are less crowded, meaning that there are less spourious detection and the new algorithm is less "noisy" than IRAF. The redshift measured errors seems to be on average slightly larger than the ones measured by the proto-E2ES_v1.0, even if the maximum measured error is lower than the $\sigma_{z,max}$ measured by the previous version.

Looking at the proto-E2ES_v2.0 results, the scattered regions due to spourius measures are less crowded with respect to the results of proto-E2ES_v1.0, contrary to what suggested by the single redshift sources analysis. We perform an analysis on the total number of measured redshift parameters, *i.e.* considering all the points plotted in Figure 5.6. In this analysis we define as good all the measures related to one of the three possible redshift values of the sample spectrum (1.324, 1.387, 1.623). All the other measures are labeled as spurious measures. This analysis is summarised in Table 5.2. Both the datasets of version 1.0 and 2.0 are analysed and compared. On each resulting dataset we compute the total number of measures, the spurious and good measures and the ratio $\mathbb{R}$ between spurious measures and the total number of measures.

Table 5.2: Comparison of spurious and good measures between version 1.0 and version 2.0 of the proto-E2ES. The good counts are also given per redshift: z_1 is the reference redshift of 1.324, z_2 is 1.387 and z_3 is 1.623.

	Total	**Spurious**	**Good**	z_1	z_2	z_3	$\mathbb{R}$
Version 1.0	339	142	197	122	23	52	0.42
Version 2.0	758	127	631	256	273	102	0.17

The total number of measures in the proto-E2ES_v2.0 results is higher, due to the fact that this version of the simulator detects better the weakest line in the spectra. On the other hand the number of spurious measures is lower: in version 1.0 we have 142 spurious measures over a total of 339, the 42% of the total; in the second version of the simulator we count 127 spurious measures on 758, being the 17% of the total counts.

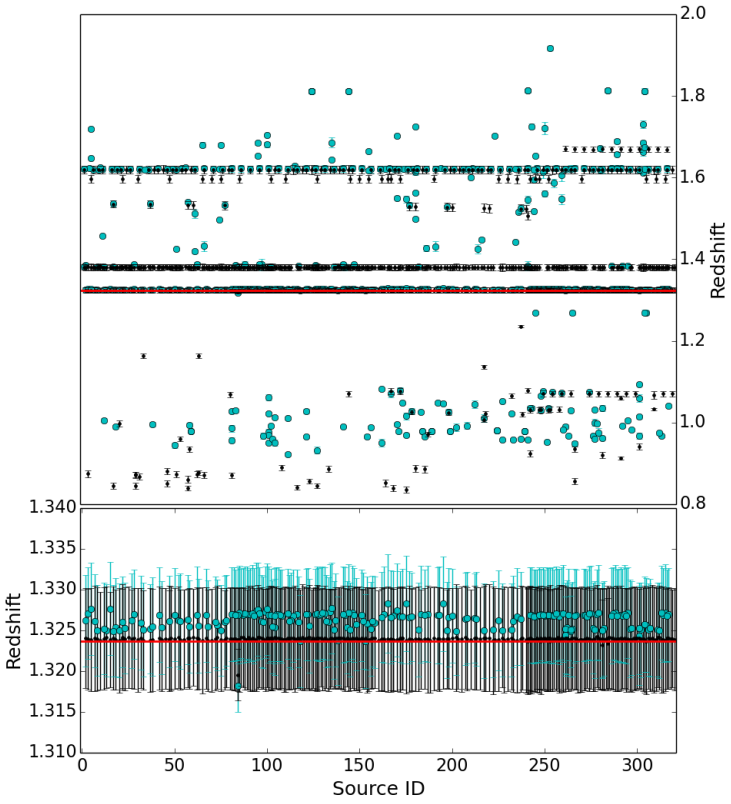

Figure 5.6: Top: Comparison between the results of the proto-E2ES_v1.0 and the proto-E2ES_ v2.0. Cyan dots refer to version 1.0, while the black points to version 2.0. The line detection of the new algorithm seems to behave better than IRAF: all the three spectral line are detected for the majority of the sources, there is a negligible scatter between the measured "correct" z and the catalog value and the scattered regions are less crowded, with a 17% of spourius detection against the 45% of the proto-E2ES_v1.0.
Bottom: zoom on the correct values.

5.4 Proto-E2ES Summary

Some open points arisen from the first version of proto-E2ES are still present in version 2.0. In order to obtain a realistic and reliable simulation the redshift extraction algorithm must be improved and the whole simulation chain must be tested on a more realistic catalog. Furthermore, integration of the ZEUS tool in the E2ES pipeline is mandatory in order to achieve good control on this background source. A complete control on optics and instrumental simulation is strongly related to the evolution of the mission database and to the proper instrument test campaign. For this reason the OM and DS modules must be

considered continously evolving. In addition, modules such as the OBDG and the SCE are thought to handle telemetry, which requires its own simulation chain and makes handling this information far from trivial.

Besides some open points still to be closed, the prototype shows also some strenghts. Dealing with the software design, for instance, the reference architecture proposed in this work, containing the basic modules for the simulator, provides the required flexibility to support extensive and evolutionary growth. Still, coupled to a simulator framework and building blocks, allows defining and implementing the E2ES faster and with less effort.

The presented work must be seen as a feasibility study. Nevertheless, some information can be infered even from its basic functionalities. Even with its basic functionalities, proto-E2ES can be used to make a rough but representative sensitivity analysis, as detailed in Chapter 6. Furthermore, the prototype represents a useful tool in order to understand where open points are still present and to test, in a simplified way, possible solutions.

Chapter 6

Sensitivity Analysis and Tests

The proto-E2ES provides a quick sensitivity analysis, aimed at understanding if and how the output results are affected by a possible deviation of the input parameters from nominal values. This can be estimated by slightly changing input parameters. This kind of analysis allows us to understand how sensible the simulator is to deviations in pointing coordinates or variations of the exposure time.

Some tests have been done in order to investigate different aspects: the Zodiacal Light background, the OM model development and the optical persistence treatment. The tests are very basic, based mostly on toy models, but they can be seen as a preliminary feasibility study towards substantial improvements in the simulator and to explore possible usage examples of the proto-E2ES.

6.1 Sensitivity Analysis

This kind of analysis is focused to understand how the simulation output changes if a deviation from the nominal value on one of the pointing coordinates is present and how far we can deviate from reference pointing parameters values, obtaining the same simulation output. The basic idea is to change the parameters one by one by a variable quantity and see when the changes affect the simulation results.

The critical point of this exercise is how to assess the potential impact of the uncertainties highlighted in the sensitivity analysis on the expected Euclid performance [**?**, VV] A model to assess instrument performance to size instrument requirements is already under deveopment for the photometric channel of Euclid/NISP (NISP-P). A similar model is required to compare the results of the sensitivity analysis with the mission requirements on the redshift mesurement on NISP-S:

- $0.7 < z < 2.0$
- $\sigma_z < 0.001(1 + z)$
- Completeness: 45 %
- Purity: 80%

Furthermore, the model shall take into account the mission requirements on the pointig stabilty reported in the Euclid System Requirements Document [**?**].

The development of such a model is beyond the scope of this work and represents a further development of the sensitivity analysis. The goal is to have, in the future, a model that allows us to take into account changes related to realistic pointing jitters and that considers thermo-mechanical perturbations on the instrumental setup.

Sensitivity analysis is performed on all the pointing parameters contained in the ECSS module operational time-line: pointing coordinates (RA and DEC) and exposure time.

6.1.1 Pointing coordinates

The first sensitivity analysis is made on pointing coordinates. The goal of this analysis is to estimate the minimum deviations Δ in right ascension RA or declination DEC which makes two pointings undistinguishable.

Starting from a reference pointing:

- $\mathrm{RA}_{ref} = 150.7°$, $\mathrm{DEC}_{ref} = 1.8°$

and given a deviation Δ on one of the coordinates, the test consists in the simulation of a triplet of pointings:

- Reference pointing;
- Reference pointing with on of the two coordinates shifted by $-\Delta$;
- Reference pointing with on of the two coordinates shifted by $+\Delta$;

The analysis is performed on RA and DEC independently.

RA Sensitivity Analysis

Assuming different values of the parameter Δ, we simulate, for each Δ, a triplet of pointings of the form:

- pointing 1: RA_{ref}, DEC_{ref}
- pointing 2: $\mathrm{RA}_{ref} - \Delta$, DEC_{ref}
- pointing 3: $\mathrm{RA}_{ref} + \Delta$, DEC_{ref}

We consider the following values of Δ: $0.1°$, $0.05°$, $0.01°$, $0.005°$, $0.001°$, $0.0005°$, $0.0001°$. These values are not directely related to the pointing precision achieved by Euclid..

Results are summarised with the help of two kinds of plot: one showing the sources detected in the catalog and the other one showing the measured redshift parameters over the source ID. In the detection plot, the black stars represent the sources detected simulating the reference pointing. The blue circles represent the sources detected simulating the $\mathrm{RA} - \Delta$ pointing, while the red circles represent

the detections in the RA + Δ case. In the z versus source ID plot, the color code is the same: in black the reference pointing results, in blue the RA − Δ results and in red the RA + Δ case. On top, we report the expected detected sources, **i.e.** the sources detected in the reference pointing simulation (analogue of the detection plot).

For each shifted pointing we computed a parameter, defined as:

$$\mathbb{H} = \frac{[\text{counts in } \Delta] \cap [\text{counts in ref}]}{[\text{counts in ref}]}$$

where the "counts in Δ" are the detected sources in the shifted pointing and the "counts in ref" are the detected sources in the reference pointing. The parameter $\mathbb{H}$ gives an estimation of how many sources are detected both in the reference pointing and in the shifted one, with respect to the reference pointing counts. The sources detected in the reference pointing are the sources we expect to detect in the shifted pointing. We provide a table with the values of the $\mathbb{H}$ parameter, together with the value of the relative shift Δ.

In Figure 6.1 the results of the analysis for $\Delta = 0.1°$ are reported. In the upper panel, the detection of the reference pointing are in black, while the blue and red circles represent the detection of the $-\Delta$ and $+\Delta$ cases respectively. In the lower panel the measured redshift for each pointing in the triplet are reported, together with a list of the sources detected in the reference pointing simulation. Roughly speaking, assuming a deviation of $\Delta \pm 0.1°$, we simulate three different pointings. This can be seen in both the plot in Figure 6.1, but also looking at the value of the $\mathbb{H}$ parameter, listed in Table 6.1. In both the RA − Δ and RA + Δ pointings we detect the 75% of the expected sources.

The discrepancy in the output decreases narrowing the deviation Δ. A good convergence between the three pointings is obtained for $\Delta = 0.0005$. In this case the agreement in the output of the three pointings can be seen qualitatively in Figure 6.2, but also quantitatively via the $\mathbb{H}$ parameter. In this case we detect the 100% of the expected sources in the RA − Δ pointing and the 99% in the RA + Δ pointing.

Table 6.1: Analysis of the hits on RA parameter.

Δ	$\mathbb{H}$	Δ	$\mathbb{H}$
-0.1	0.72	+0.1	0.75
-0.05	0.79	+0.05	0.93
-0.01	0.99	+0.01	0.94
-0.005	0.95	+0.005	0.95
-0.001	0.96	+0.001	0.99
-0.0005	1.00	+0.0005	0.99

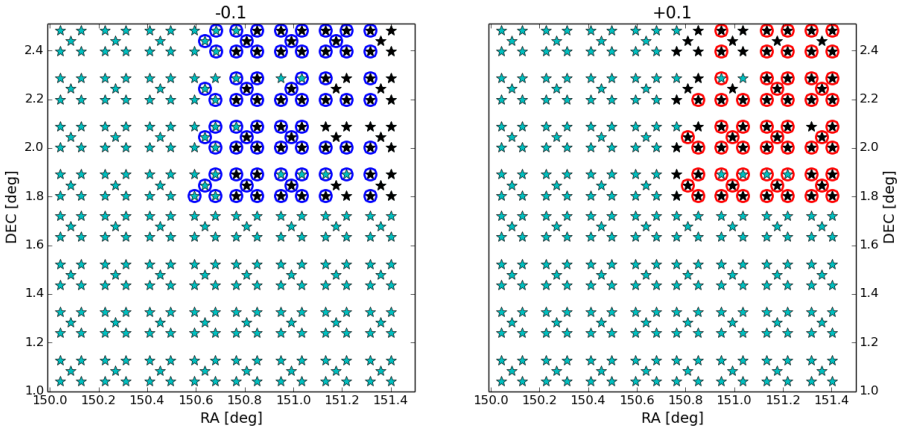

(a) *Detections.*

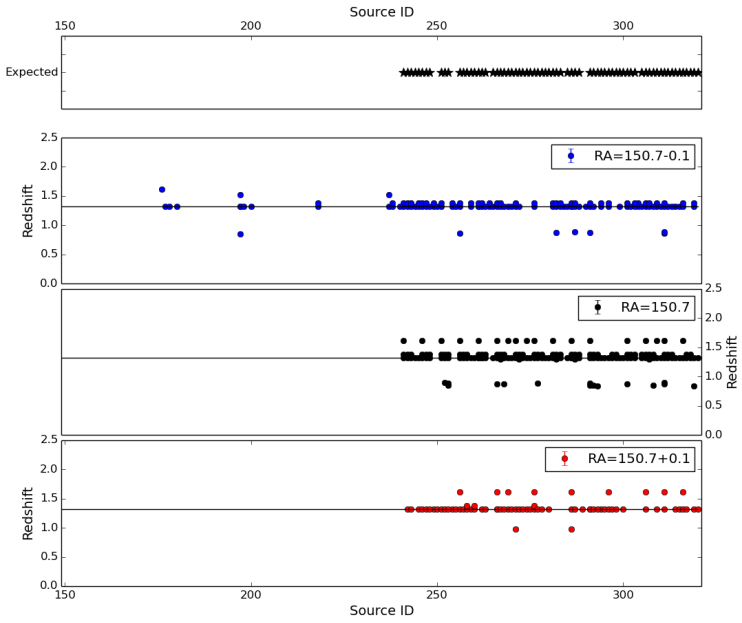

(b) *Measured redshift values.*

Figure 6.1: Sensitivity analysis on RA with $\Delta\text{RA} = 0.1^{\circ}$.

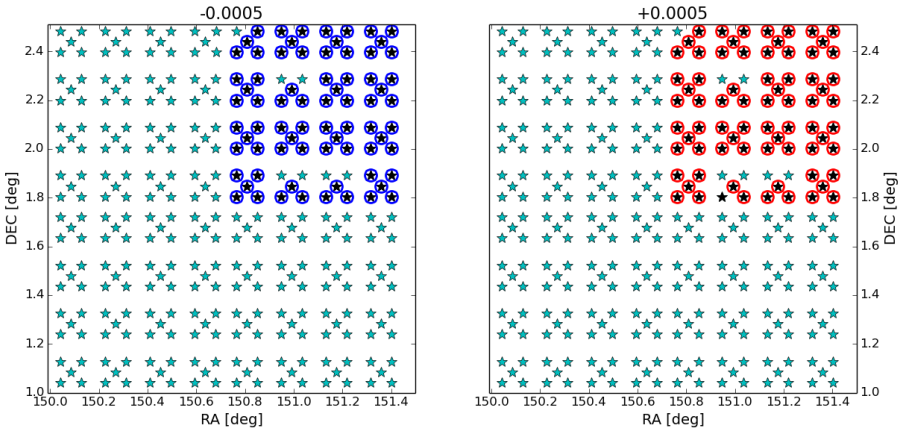

(a) *Detections.*

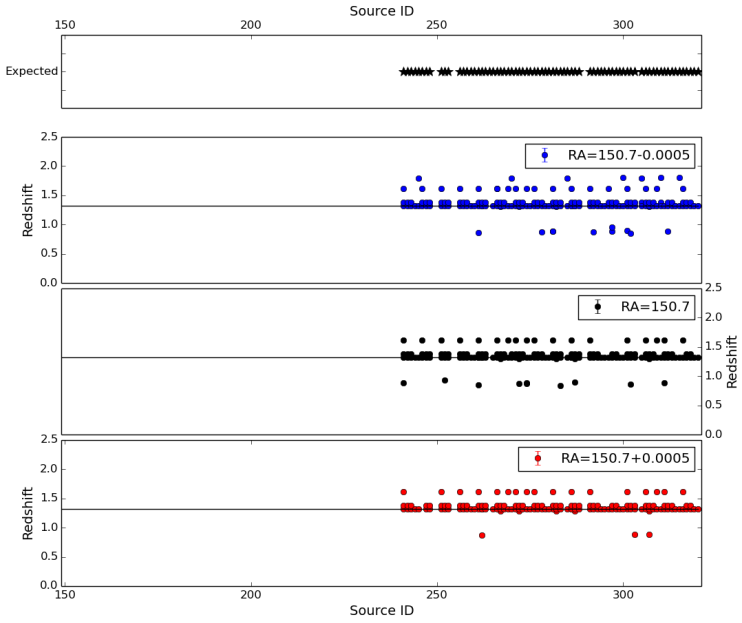

(b) *Measured redshift values.*

Figure 6.2: Sensitivity analysis on RA with $\Delta\mathrm{RA} = 0.0005°$.

DEC Sensitivity Analysis

The same analysis described for the RA case is performed on the DEC parameter. Assuming the same values of Δ used for the RA analysis, we simulate for each value of Δ a triplet of pointings of the form:

- pointing 1: RA_{ref}, DEC_{ref}
- pointing 2: RA_{ref}, $\mathrm{DEC}_{ref} - \Delta$
- pointing 3: RA_{ref}, $\mathrm{DEC}_{ref} + \Delta$

As for the RA analysis, results are summarised with the help of two kinds of plot: a detection plot and a z versus source ID one. The color code is similar to that used for the RA analysis: black represents the reference pointing, blue the $\mathrm{DEC} - \Delta$ results and red the $\mathrm{DEC} + \Delta$ case.

The results of the analysis are similar to the results obtained analysing RA. In Figure 6.3 the case of $\Delta = 0.1^\circ$ is reported, while in Figure 6.4 we show the case $\Delta = 0.0005^\circ$. Looking at Figure 6.3 it can be seen that, similarly to what we observe in the RA analysis, taking into account a deviation of $\pm\Delta = 0.1^\circ$ we are simulating three different pointings. This is quantitatively shown in Table 6.2, where the values of the $\mathbb{H}$ parameter are reported for each value of Δ. The $\mathrm{DEC} - \Delta$ simulation detects the 77% of the expected sources, while the $\mathrm{DEC} + \Delta$ only the 46%.

The best agreement between $\mathrm{DEC} - \Delta$, $\mathrm{DEC} + \Delta$ and the reference pointing is obtained for $\Delta = 0.0005$. In both $\mathrm{DEC} - \Delta$ and $\mathrm{DEC} + \Delta$ pointings the 99% of the expected sources are detected.

Table 6.2: Analysis of the hits on DEC parameter.

Δ	$\mathbb{H}$	Δ	$\mathbb{H}$
-0.1	0.77	+0.1	0.46
-0.05	0.74	+0.05	0.69
-0.01	0.86	+0.01	0.60
-0.005	0.83	+0.005	1.00
-0.001	0.97	+0.001	0.99
-0.0005	0.99	+0.0005	0.99

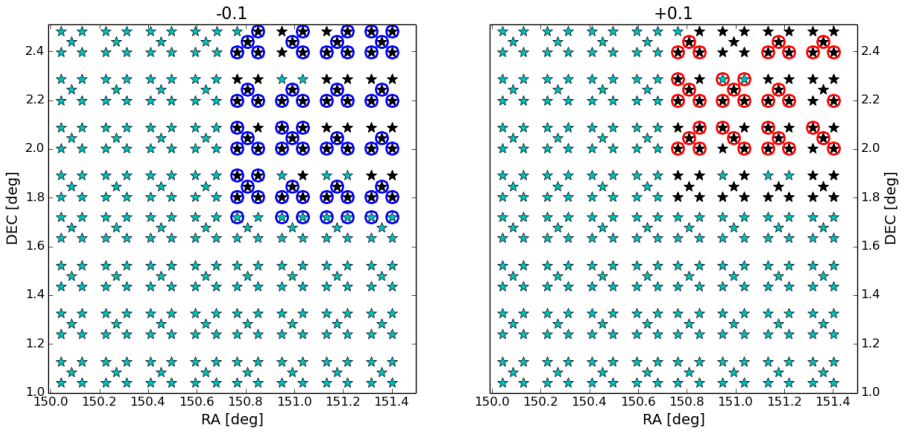

(a) *Detections.*

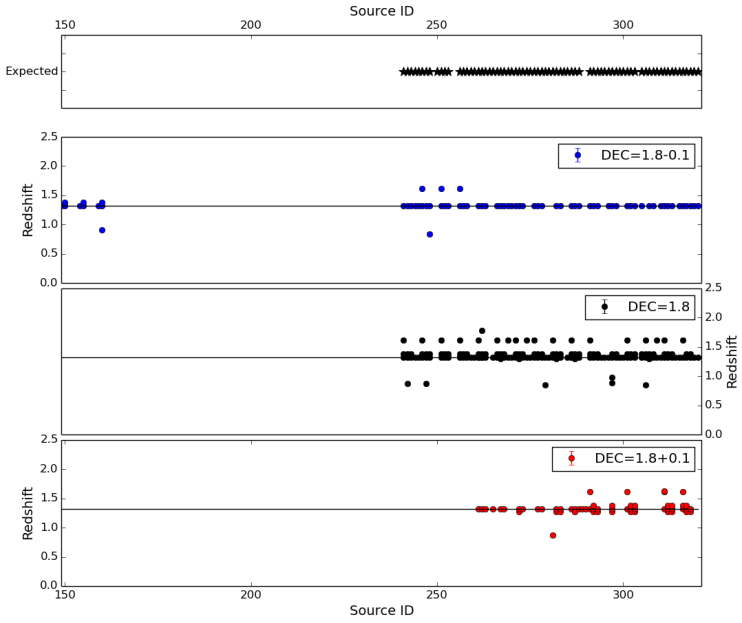

(b) *Measured redshift values.*

Figure 6.3: Sensitivity analysis on DEC with $\Delta\text{DEC} = 0.1°$.

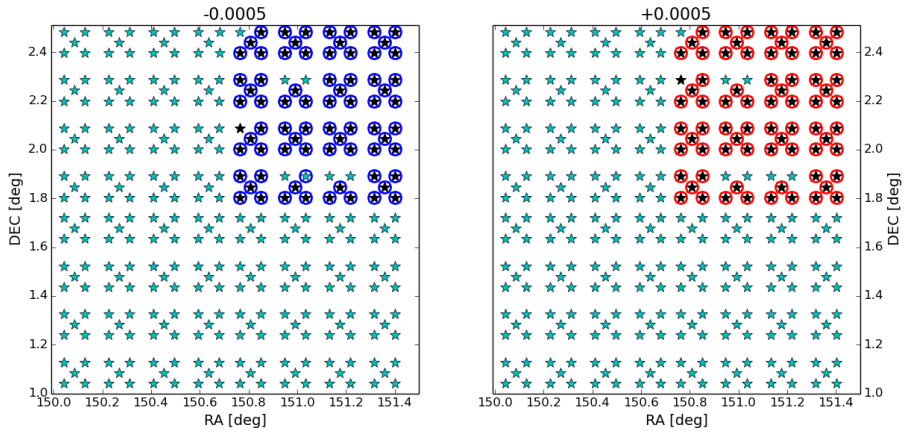

(a) *Detections.*

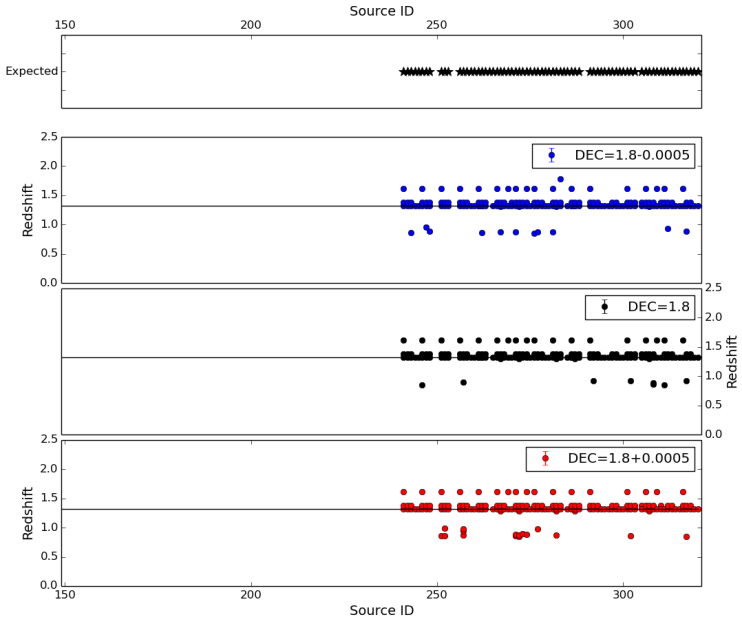

(b) *Measured redshift values.*

Figure 6.4: Sensitivity analysis on DEC with $\Delta\text{DEC} = 0.0005°$.

6.1.2 Exposure time

The second sensitivity analyses is aimed at testing how the simulation is affected by the variation of Euclid/NISP exposure time. The exposure time of 560 s considered so far allows to reach the flux limit, required for Euclid/NISP of $3 \cdot 10^{-16}$ erg cm^{-2} s^{-1} at 1600 nm with a SNR$>$ 3.5. This statement can be tested with an Exposure Time Calculator (ETC) software tool. To make this test, we select the ETC-42 tool.

ETC-42 is a generic pourpous ETC. It is designed to facilitate the integration of new sites, instruments and sources by the user. It is not instrument-specific and it is used in several project implementations, including Euclid, covering a wide wavelength range, from near IR to UV [44].

We setup the instrumental environment with the same Euclid/NISP instrumental parameters used as input by TIPS:

- Dark Noise: 0.1 e pixel^{-1} s^{-1}
- Readout Noise: 6.0 e pixel^{-1}
- Pixel Scale: 0.3 arcsec pixel^{-1}

We simulate the exposure time needed to detect a 1600 nm line with a flux of $3 \cdot 10^{-16}$ erg cm^{-2} s^{-1} with SNR$>$ 3.5. We find an exposure time of 561.88 s in accordance with Euclid/NISP instrument requirements. Spectra in our sample have lines with fluxes of some 10^{-15} erg cm^{-2} s^{-1}. We simulate the exposure time needed to see a line of 10^{-15} erg cm^{-2} s^{-1} obtaining a value of 125.12 s. To detect a flux of some units of 10^{-15} erg cm^{-2} s^{-1}, tens of seconds are needed. Going back to proto-E2ES, we expect to obtain an exaustive simulation for an exposure time EXPTIME $\simeq 100$ s.

Table 6.3: Analysis of the hits on EXPTIME parameter.

EXPTIME [s]	$\mathbb{H}$	**Completeness**
1	0.68	0.05
10	0.88	0.29
100	1.00	0.99
140	0.99	1.00
280	1.00	0.99
560	1.00	0.99

We simulate a reference pointing of RA = 150.7° and DEC = 1.8°, considering different exposure times: 1, 10, 100, 140, 280 and 560 s. In Figure 6.5 the produced TIPS slitless images are shown. It can be noted that for an exposure time of 1 or 10 s the image is dominated by noise. For values greater than 100 s, sources are detected. Furthermore, the greater the exposure time, the less noisy the image gets.

In Figure 6.6 the simulation output is reported for the different exposure times. Above 100 s the simulator is able to correctly extract the spectra and identify the spectral lines. This can be seen in Table 6.3 in which for each value of the EXPTIME parameter we report the values of $\mathbb{H}$ and purity. starting from EXPTIME $\simeq 100\ s$ we start to detect all of the expected sources with a purity of 99% or more, in the case of EXPTIME $\simeq 140\ s$. This is in agreement with our expectation.

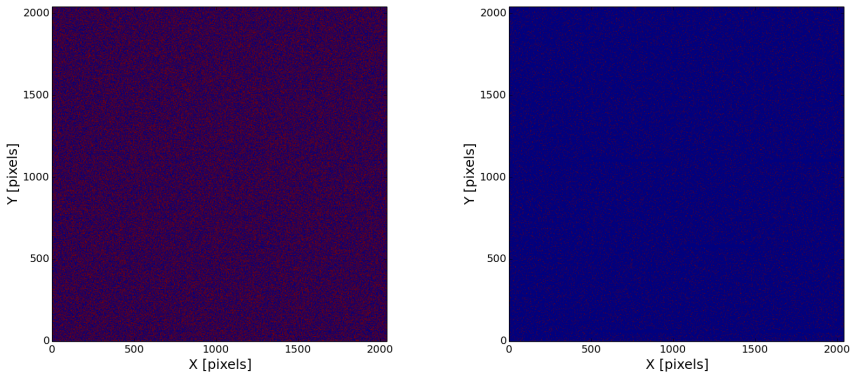

(a) *EXPTIME = 1 s.*

(b) *EXPTIME = 10 s.*

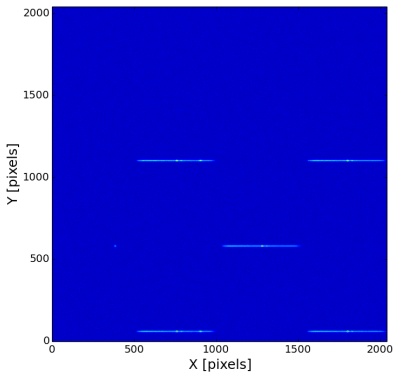

(c) *EXPTIME = 100 s.*

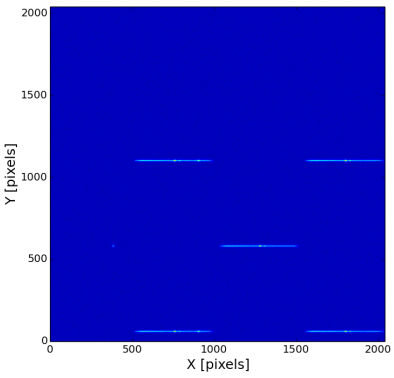

(d) *EXPTIME = 140 s.*

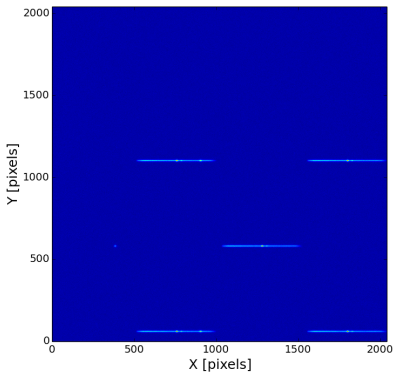

(e) *EXPTIME = 280 s.*

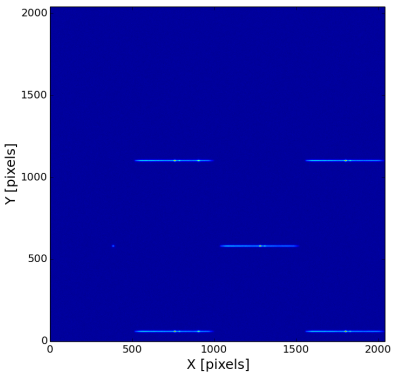

(f) *EXPTIME = 560 s.*

Figure 6.5: Slitless images simulated with different exposure times. For exposure times lesser than 100 s the image is dominated by noise.

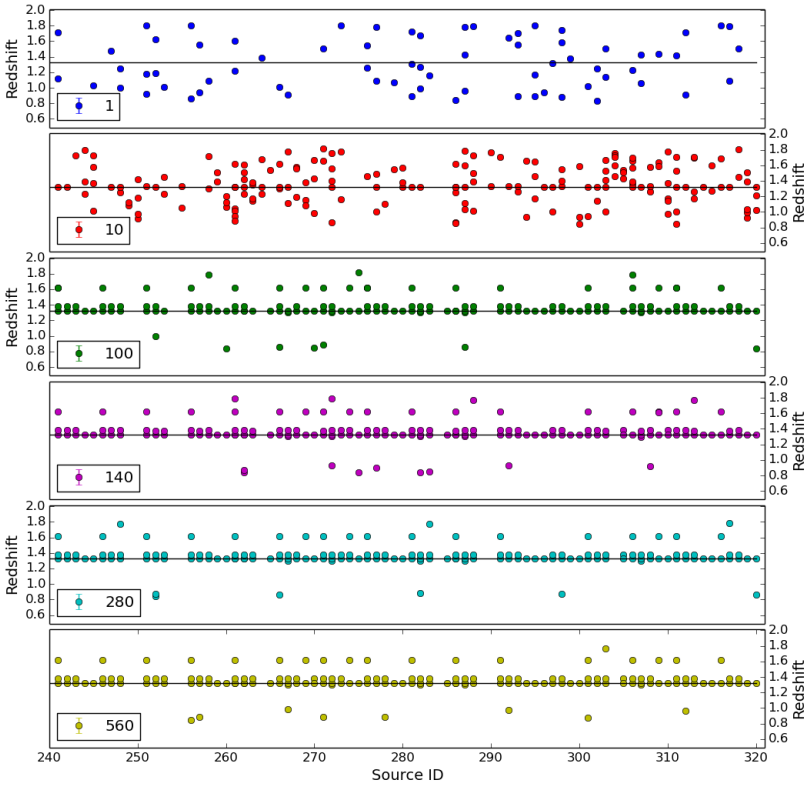

Figure 6.6: Simulation output for different values of exposure time. The spectra are completely treated for values greater than 100s.

6.2 Tests on Open Points

As seen in Chapter 5, a series of open points arose from version 1.0 of the prototype. Of the open points shown in Table 5.1, upgrading the simulator to its version 2.0 only closes the one related to IRAF. A series of issues are still present with a priority level above "Medium":

- Use of more realistic test catalog;
- ZEUS integration aimed at considering a good Zodiacal Light background model in the simulations;
- Definition of transfer functions in order to simulate a non ideal optical model;
- A persistence test.

The catalog open point has not been treated in this work, since we preferred to focus on a better implementation of the whole pipeline. The other three points have been investigated via a set of tests, aimed at giving a preliminary analysis of the problem. The reported tests, summarized in Table 6.4, represent "quick and dirty" exercises designed to give a rough idea on how to close the respective open points.

Table 6.4: Test summary: each module is related to the test which affect it the most.

Module	Test
ECSS	None
SS	**ZEUS Background Simulation**
SCE	None
OM	**Transfer Function Toy Model**
DS	**Persistence Toy Model**
OBDG	None
DPC	None
PA	None

6.2.1 Zodiacal Light background

The background of Zodiacal Light (ZL) is a major component to take into account the planned Euclid observations. ZL is the combination of scattered solar light and thermal emission due to Interplanetary Dust Particles (IDPs) forming a system of clouds approximately aligned with the ecliptic plane. In the Euclid wavelength range, the Zodiacal background is caused mainly by scattered sunlight from the dust cloud.

Assuming the observer E at a given position $\mathbf{r}_E$ with respect to the Sun, and being L the distance from the observer, as shown in Figure 6.7, the amount of

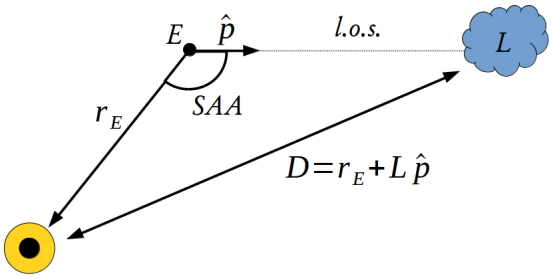

Figure 6.7: Geometry of the line integral in Equation 6.1.

light received is the line integral of the radiation scattered or emitted along the whole line of sight along the pointing direction $\hat{\mathbf{p}}$:

$$I_{ZL}(\hat{\mathbf{p}}, t) = \int_0^\infty dL \sum_c N_{ZL,c}\left(\mathbf{r}_E(t) + L\hat{\mathbf{p}}\right) F_{ZL}\left(\mathbf{r}_E(t) + L\hat{\mathbf{p}}\right) \tag{6.1}$$

where $F_{ZL,c}$ is the production of ZL in a given solar system location, $N_{ZL,c}$ the density of IDPs in that location, and c denotes the IDPs subcloud contributing to ZL. Since the observer is orbiting the Sun, $\mathbf{r}_E$ is a function of the observing time t, and I_{ZL} is a function of time too. For a periodic orbit ZL will present an important seasonal variability.

Both the spatial and temporal dependencies of the ZL, together with second order correction linked to the irregular distribution of dust in the cloud (accounting for fractions of %), are integrated in the so called COBE model [45], which represents the standad model for zodiacal light estimation.

In Euclid, as well as in many other surveys, operations are planned and optimized using one or more Survey Optimization Codes (SOCs). SOCs, which are generally based on static maps and catalogues, can hardly handle the inherent ZL time variability. The ZEUS project (Zody EUclid Simulator)[46], developed within the framework of the Euclid mission, attempts to answer the problem of decoupling the ZL model from the optimization code.

ZEUS is written in Python and needs the pyfits and healpy libraries. Given a possible survey, *i.e.* a list of couples $(t, \hat{\mathbf{p}})$, ZEUS computes the ZL contamination starting from a set of precomputed tables, which are representative of a particular combination of ZL model $\mathcal{M}_{ZL}$ and expected Euclid orbit $\mathcal{O}_{ZL}$. At first ZEUS assumes an Ecliptic corotating reference frame, whose longitudes originate from the Sun at the epoch of observation $\lambda_\odot$. In this reference frame any pointing direction has a fixed height above the ecliptic and a fixed Solar Aspect Angle (SAA). In Euclid a large number of observations are framed in time intervals so short that ZL can be considered a time constant. A single ZL corotating map can be used for many simulated observations compensating the computational cost for its derivation.

As a preliminary application to the proto-E2ES sky simulation, we provide a script aimed at simulating a set of ZL background map of the whole sky using the ZEUS tool. Figure 6.8 shows the minumum, maximum and mean flux over one year simulation. This kind of background maps are thought aiming at the creation of a realistic simulated sky. Work in this sense is still in a preliminary stage. From a preliminary analysis the following issues arise:

- A model to treat the ZL background is already implemented in TIPS. A tuning between the ZEUS and TIPS models is required in order to use ZEUS maps to create TIPS-compliant catalogs;
- ZL fluxes simulated by ZEUS must be scaled to source fluxes in order to convolve a ZL background map with the input catalog;
- ZL spectrum shows a strong dependence on the Fraunhofer component of the Solar spectrum[1]. This feature is still not treated by ZEUS but is mandatory in order to understand how source spectra are affected by ZL background.

These open points represent a starting point towards the integration of the ZEUS tool in a future version of the simulator.

[1] Fraunhofer absorption lines observed in the Sun photosphere

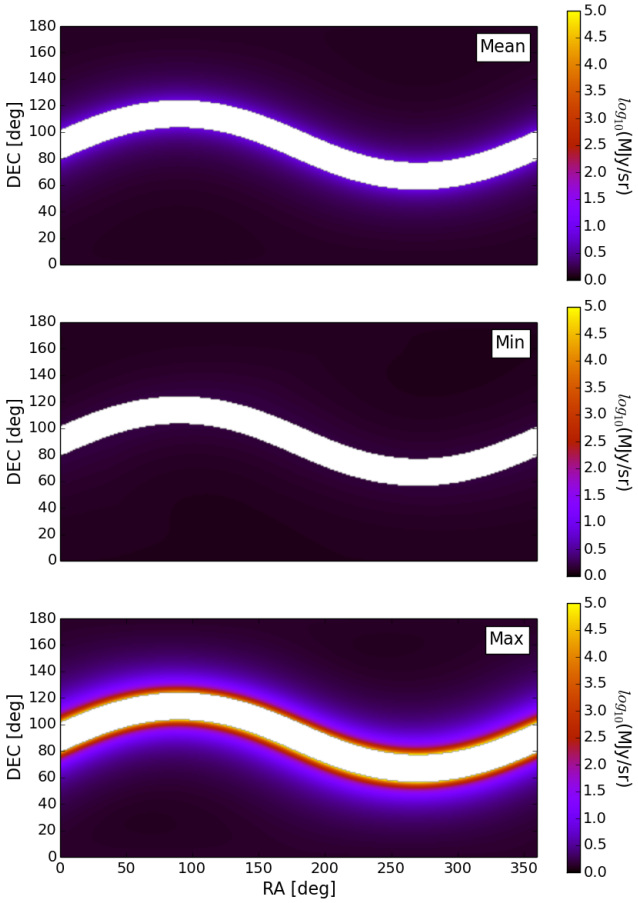

Figure 6.8: Maps of Zodiacal Light obtained using the ZEUS software, simulating one year. **Top**: mean. **Center**: minimum. **Bottom**: maximum.

6.2.2 Encircled Energy Radius Transfer Function

In this work, the proposed usage of the simulator is focused on instrument operations. An important thing to take into account during instrument operations is how to treat possible deviation from ideal optics. This requires an adaptable optical model and, in the specific case of this work further development on the Optical Model Module is needed.

The optical model is provided in a parametric way. In a future version of the simulator, including a complete OM Module, the optical parameters will be modified by a set of tranfer functions. This exercise is meant to represent a first analysis towards the implementation of this set of transfer functions. The goal is to integrate the transfer functions in the OM Module in order to assess how changes of the optical model impact the expected performance of the instrument. Work in this sense is strictly linked to the maturity level of the mission database. Since the database is still in its preliminary stages, in this work a simple toy model is proposed in order to show how the interesting optical parameters can be modified.

We investigate two different cases, taking into account two representative effects on the PSF due to a possible perturbation of the optical setup:

- A shift of the PSF
- Changes in the PSF ellipticity

A typical optical parameter used in spectroscopy is the radius from the center of the instrument PSF containing the 80% of the total energy of the PSF. This parameter is known as Encircled Energy (EE) radius at 80%. To compute the EE radius we calculate the EE, starting from the optical PSF, via the formula:

$$EE(r) = \int_0^{\pi} \int_0^{r} PSF(r) dr d\Omega \tag{6.2}$$

and select the radius $r_{EE}(80)$ at which the 80% of the PSF energy is encircled.

We investigate two different cases:

- A shift of the PSF
- Changes in the PSF ellipticity

A brief description of the adopted procedure is given below.

Shift

Let us consider PSF shift due to a systematic effect. The best Gaussian fit[2] (or combination of Gaussian functions) is shifted by a defined offset. The encircled energy is calculated before and after the shift, in order to define the parameter α_{trans} as the ratio between the values of the 80 % encircled energy radius $r_{\rm EE}(80)_g$ before and after the shift:

$$\alpha_{shift} = \frac{r_{\rm EE}(80)_{g,shift}}{r_{\rm EE}(80)_g} \tag{6.3}$$

The procedure is iterated in a range of offsets, in order to compute a rough transfer function, as reported in Figure 6.9. Panel **(a)** shows the values of the α_{shift} parameter as a function of the best fit Gaussian shift in pixels. To compute the encircled energy values we apply Equation 6.2, integrating the best fit Gaussian on a map of 2048×2048 pixels. Since we calculate the integral starting from the center of the map, which is fixed, we expect that the greater the shift the greater the value of $r_{\rm EE}(80)_{g,shift}$ with respect to the value of $r_{\rm EE}(80)_g$, *i.e.* we expect α_{shift} to be greater than one, increasing with the shift value.

Given the offset, the new value of the 80 % encircled energy radius is given by:

$$r'_{\rm EE}(80) = \alpha_{shift} \cdot r_{\rm EE}(80) \tag{6.4}$$

The new value for the EE radius is then stored and used at DPC level during the spectra extraction.

Ellipticity

Let us consider a change on the PSF ellipticity. The ratio between the major and minor axes of the best fitting Gaussian function (or combination of Gaussian functions) is changed. The encircled energy is calculated before and after the change, in order to define the parameter β_{trans} as the ratio between the values of the 80 % encircled energy $r_{\rm EE}(80)_g$ before and after this change:

$$\beta_{ell} = \frac{r_{\rm EE}(80)_{g,ell}}{r_{\rm EE}(80)_g} \tag{6.5}$$

The procedure is iterated in a range of axes ratios, in order to esteem a rough transfer function, as reported in Figure 6.9. Panel **(b)** shows the values of the β_{ell} parameter as a function of the ratio of the axes of the best fit Gaussian. The encircled energy is computed as in the previous case. The x axis of the best fit Gaussian is left unchanged, while the y axis is multiplied by an increasingly integer factor. An axes ratio of 2 means that the doublet (σ_x, σ_y) of the new Gaussian is $(\sigma, 2 \cdot \sigma)$ with respect to the reference best fit Gaussian. With this

[2]This is a rough approximation, but allows to work with a simple well known function.

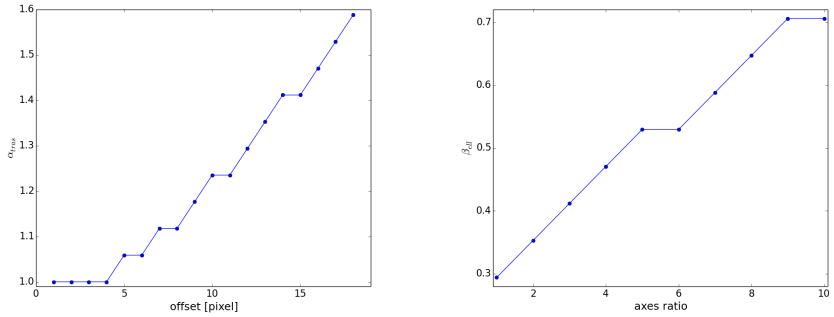

(a) α_{shift} *in function of the shift offset.* **(b)** β_{ell} *in function of the axes ratio of the best fitting Gaussian.*

Figure 6.9: Encircled Energy radius transfer functions for PSF shift end changes in PSF ellipticity. In panel **(a)** we report the values of the α_{shift} parameter as a function of the best fit Gaussian shift in pixels. In panel **(a)**, the values of the β_{ell} parameter as a function of the ratio of the axes of the best fit Gaussian.

assumption, stretching the best fit Gaussian, we expect the value of $r_{\rm EE}(80)_{g,ell}$ to be smaller than the value of $r_{\rm EE}(80)_g$. On the other hand the greater the axes ratio the greater the absolute value of $r_{\rm EE}(80)_{g,ell}$. Combining these two trends, we expect a value of $\beta_{ell} < 1$, increasing with the axes ratio of the modified Gaussian.

Given the axes ratio, the new value of the 80 % encircled energy radius is given by:

$$r'_{\rm EE}(80) = \beta_{ell} \cdot r_{\rm EE}(80) \tag{6.6}$$

The new value for the EE radius is then stored and used at DPC level during the spectra extraction.

In this simple toy model, the two transfer functions can be combined: if both a shift and a change in ellipticity are considered, the resulting EE radius can be computed as:

$$r'_{\rm EE}(80) = \alpha_{shift} \cdot \beta_{ell} \cdot r_{\rm EE}(80) \tag{6.7}$$

6.2.3 Persistence

The simulator can be used to perform a test on Euclid/NISP detector persistance. Detector persistance occures when electrons generated in previous exposures, expecially looking at very bright sources, are trapped at impurity sites

in the CCD. These electrons are released in subsequent exposures and appear as residual images, or "ghosts". Goal of this exercise is to test how a ghost image can affect the scientific result by using this simulation environment.

Looking at the sky, we obtain, for each detector, a slitless image of sources within its field of view, then the spacecraft dithers and another image is taken. If the detector points towards a very bright image during the first detection, a persistent ghost can be found in the second one. Transposing this idea in the simulator, the proposed procedure gives a preliminary estimation of the problem.

The 16 detectors of Euclid/NISP are labeled with a two digit number giving their position on the focal plane. The detectors are distributed in a 4×4 array: the first digit (from 0 to 3) gives the x position on the array, the second digit (again from 0 to 3) gives the y position. Let us consider the detector 00 (lower-left on the focal plane). The output of the DS module consists in four images, one for each dither (0, 1, 2, 3), of the detector 00 field of view: $\mathrm{I}(00)_0$, $\mathrm{I}(00)_1$, $\mathrm{I}(00)_2$, $\mathrm{I}(00)_3$. Starting from dither 1, we can find in the i-th dither image a ghost of the $(i-1)$-th dither image. A simple way to simulate this simulation is to combine the images as follows:

$$\mathrm{I}(00)_{(i+1)+i} = \mathrm{I}(00)_{i+1} + \alpha \mathrm{I}(00)_i \tag{6.8}$$

where $0 < \alpha < 1$. The combined image is then passed as an input to the DPC module and analysed by the simulator normally. A test source, labeled BEAM_5A, is taken into account to perform a sensitivity analysis using the described procedure in order to see at which level of persistence the output is significally affected.

Since the dispersion direction during the dither sequence, as shown in Chapter 2, is:

- Dither 0: 0°;
- Dither 1: 90°;
- Dither 2: 180°;
- Dither 3: 90°;

to make this usage example more clear, we simulate an unrealistic, case in which the image of dither 2 is combined with the image of dither 0, that has the same dispersion orientation. We create a combined image $\mathrm{I}(00)_{2+0}$ as:

$$\mathrm{I}(00)_{2+0} = \mathrm{I}(00)_2 + \alpha \mathrm{I}(00)_0 \tag{6.9}$$

This choice is due to the fact that the chosen test source, BEAM_5A, is clearly detected in dither 0 and 2, and the analysis is a bit easier since the orientation of dither 0 and 2 are parallel. Furthermore it must be said that this test

represents a worst case, since the input is simply a sum of the two slitless images without assuming a mask for the noise. This means that in $I(00)_{2+0}$ the noise is overestimated.

Different combinations $I(00)_{2+0}$ are processed. it must be noted that a realistic value of persistence is around the 1% [47]. Results of this test are given in Figure 6.10, showing the combination $I(00)_{2+0}$ for four different values of α (0, 0.01, 0.1 and 1), and in Table 6.5, listing the identified spectral lines in source BEAM_5A and its ghost extracted from $I(00)_{2+0}$ for different values of α. The naming convention is the following: "dither 0" refers to BEAM_5A spectrum as seen in $I(00)_0$; "dither 2" stands for BEAM_5A spectrum as seen in $I(00)_2$; "combination" is the BEAM_5A spectrum as seen in $I(00)_{0+2}$ and "ghost" is the ghost image of "dither 0" in $I(00)_{0+2}$.

In summary, the test brings to the following conclusions:

- For $\alpha = 0$, $I(00)_{2+0}$ corresponds to $I(00)_2$. Looking at the line identification, there is no difference between BEAM_5A seen in $I(00)_{2+0}$, "combination", and $I(00)_2$, "dither 2". This is expected since there is no ghost: the ghost of BEAM_5A is not detected and only noise is extracted in that slit by aXe;
- For $\alpha = 1$, $I(00)_{2+0}$ shows all the spectra present in $I(00)_2$ plus all the spectra present in $I(00)_0$, shifted accordingly to the defined shift between the considered dithers ($\Delta X = 50$", $\Delta Y = 200$", see Chapter 2. Line identification shows that both the spectra of BEAM_5A as seen in $I(00)_2$ and $I(00)_0$ are present in the extraction from $I(00)_{2+0}$ and "ghost" corresponds to "dither 0".
- For $0 < \alpha < 1$, the lower is α, the less is the impact of the ghost image. Looking at the slitless images, we can notice that a ghost image starts to be detectable from $\alpha = 0.1$. The line identification, otherwise, shows that the "ghost" image starts to be detected also by the line identification algorithm assuming $\alpha = 0.15$.

This is a preliminary result and a finer analysis is required on this point. The effective level of persistence can be measured only on the hardware, but this quick analysis suggests that persistence can be treated as a second order effect for spectra analysis.

Table 6.5: Detected lines, for different values of α, of: the sample source BEAM_5A in the input images $I(00)_0$ and $I(00)_2$; the same source as seen in the combined image $I(00)_{2+0}$; the ghost image.

$\alpha = 0$

Dither 0	**Dither 2**	**Combination**	**Ghost**
1525.09 ± 3.96	1524.97 ± 4.33	1524.97 ± 4.33	
	1704.32 ± 6.21	1704.32 ± 6.21	

$\alpha = 0.01$

Dither 0	**Dither 2**	**Combination**	**Ghost**
1525.09 ± 3.96	1524.97 ± 4.33	1524.97 ± 4.33	
	1704.32 ± 6.21	1704.32 ± 6.21	

$\alpha = 0.1$

Dither 0	**Dither 2**	**Combination**	**Ghost**
1525.09 ± 3.96	1524.97 ± 4.33	1524.97 ± 4.33	
	1704.32 ± 6.21	1704.32 ± 6.21	

$\alpha = 0.15$

Dither 0	**Dither 2**	**Combination**	**Ghost**
1525.09 ± 3.96	1524.97 ± 4.33	1524.96 ± 4.32	1524.92 ± 4.22
	1704.32 ± 6.21	1704.30 ± 6.21	

$\alpha = 0.1$

Dither 0	**Dither 2**	**Combination**	**Ghost**
1525.09 ± 3.96	1524.97 ± 4.33	1524.93 ± 4.29	1524.86 ± 3.96
	1704.32 ± 6.21	1704.20 ± 6.29	

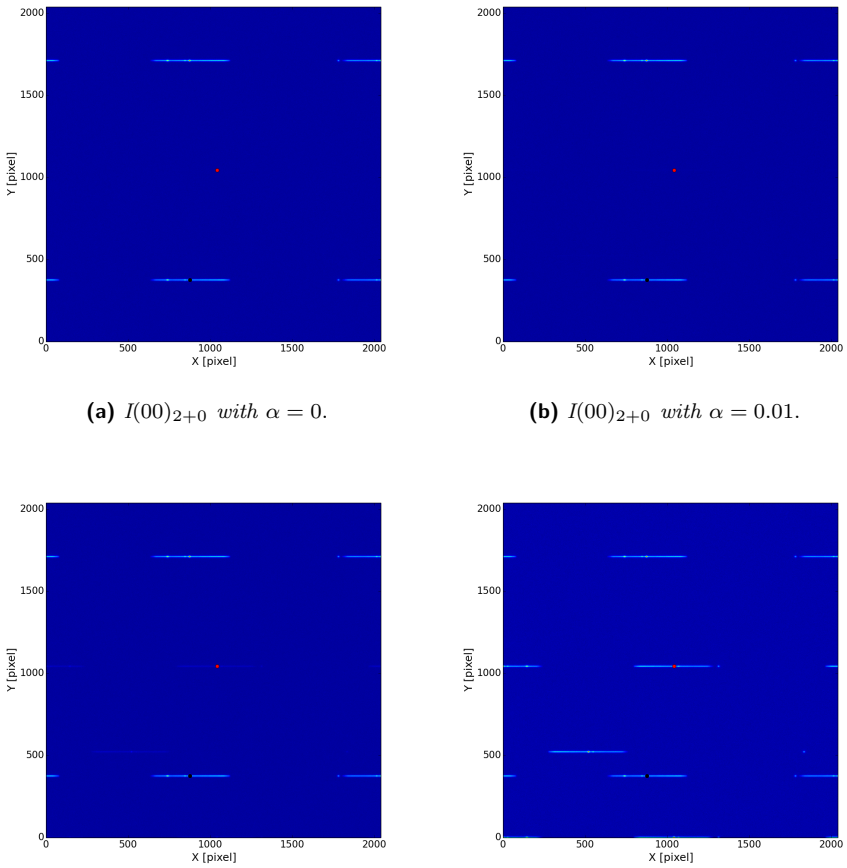

(a) $I(00)_{2+0}$ *with* $\alpha = 0$.

(b) $I(00)_{2+0}$ *with* $\alpha = 0.01$.

(c) $I(00)_{2+0}$ *with* $\alpha = 0.1$.

(d) $I(00)_{2+0}$ *with* $\alpha = 1$.

Figure 6.10: $I(00)_{2+0}$ obtained with different values of the α parameters. The black dot represents the position of BEAM_5A in $I(00)_2$, while the red dot represents the position of the same source in $I(00)_0$

6.3 Summary and Roadmap

The improvement of the prototype from version 1.0 to version 2.0 and the tests proposed above are meant to close, or at least suggest how to close, some open points arisen from the very first implementation of the simulator (see Chapter 5). The introduction of a dedicated line identification algorithm closes the IRAF open point, but other issues are still open, even if the reported tests suggest a roadmap to follow towards the implementation of a version 3.0.

The prototype allows us to perform a sensitivity analysis on the pointing parameters. This kind of analysis represent an application of the simulator which concerns instrument operations. The sensitivity analysis shows tha, in presence of an error on one of the pointing coordinates, the simulation output converges to that of the reference pointing starting from $\Delta = 0.0005$ both in RA and DEC. In addition, a sensitivity analysis on the exposure time can be performed in order to assess the exposure times expected for the instrumental setup to fulfill mission requirements.

Some improvements are direclty suggested by the reported tests. The SS module is one of the modules that must be strongly improved in a future version of the simulator. Realistic input catalog are needed in order to perform reliable simulations. Furthermore, aiming at the computation of a realistic simulated sky, integration in the SS module of ZL background, using the ZEUS tool is needed. In a mature version of the proto-E2ES is auspicable to have the possibility to create a simulated sky containing ZL contamination.

The proposed example on how to compute EE radius transfer functions represents a first step towards the simulation of non ideal optics. In addition, the proposed persistence test can be seen as a starting point in order to develop a reliable persistance analysis. Both this exercises evolve in parallel to the evolution of the mission data base from which information on the instrument optics are taken.

Another important point left open during the improvement from version 1.0 to 2.0 is the point related to redshift extraction algorithm. In future versions of the simulator work must be done towards a robust algorithm to define redshift reliability. This is also needed in order to have a reliable estimation of the purity parameter.

The reference architecture of the simulator provides the required flexibility to support tests and representative exercises also on the points not treated in this work. As an example, the DPC module allows to perform a test in order to obtain a redshift measurement and analysis directly on the single dither images, without combining the output of each dither simulation. Such a test is not meant to give any improvement to the redshift extraction, but it can represent a usefull test in order to assess the performance of each single dither simulation. Furthermore it can give a feedback on the goodness of the dithering strategy, showing possible error sources linked to grism rotation.

A set of more specific tests on the external software tools used in the prototype is needed to test the robustness of such tools. A test, for instance, can be performed

on aXe. A simulation of an empty slit can pinpoint possible systematics of numerical artifacts linked to aXe or to its integration in the prototype pipeline.

6.3.1 Towards a full E2ES

The roadmap for the future development of a full E2E simulation of Euclid aimed at an operational usage is defined in the ESA internal report *EUCLID E2E ROADMAP* [48]. The roadmap is divided in three milestones which foresee three different levels of implementation of the E2ES:

1. E2ES #1: full simulator with NISP S instrument;
2. E2ES #2: full simulator with NISP S , NISP P and VIS instruments;
3. E2ES #3: additional science cases applied.

In table 6.6 we provide a list of possible improvements to be applied to each module in future versions of the simulator.

Table 6.6: List of possible improvements towards a full E2ES.

Module	Improvement	Milestone
ECSS	• Analyse realistic fields	E2ES #1 E2ES #2
	• Analyse mission reference scenarions	E2ES #3
SS	• Integrate ZEUS	E2ES #1
	• Improve background models	E2ES #2
SCE	• Handle attitude, thermal status and telemetry.	E2ES #2
OM	• Integrate EE radius transfer functions	E2ES #1
	• Implement NISP-P PSF transfer functions	E2ES #2
	• Implement VIS PSF transfer functions	E2ES #2
DS	• Implement NISP-P chain	E2ES #2
	• Implement VIS chain	E2ES #2
OBDG	• Test data compression	E2ES #3
DPC	• Implement a dedicated spectral extraction algorithm	E2ES #1
	• Assign z reliability levels	E2ES #1
	• Implement NISP-P data processing and calibration	E2ES #2
	• Implement NISP-S/NISP-P cross calibration	E2ES #2
	• Implement VIS data processing and calibration	E2ES #2
	• Implement VIS/NISP cross calibration	E2ES #2
PA	• Assess performance on z measures	E2ES #1
	• Assess performance on main cosmological probes	E2ES #2
	• Assess performance on ancillary cosmological probes	E2ES #3

Conclusion

THIS work describes my Ph.D. project, which is based on two main activities: the analysis of Jupiter flux time-lines as seen by the Planck mission and the implementation of a prototype end-to-end simulator, using the Euclid mission as a test case, designed to asses instrument operations.

Besides the improvement of Jupiter SED results quoted in literature, Jupiter flux analysis is an important part of the Planck/LFI calibration procedure. Furthermore, Planck and WMAP data can be intercalibrated, comparing our results on the Jupiter spectral analysis with respect to the results of the same analysis performed on WMAP. Planck provided a good measurement of the brightness temperature for Jupiter, with an accuracy better than half a percent. The measured T_b shows a residual R2R deviation of 1% in the worst case (44 GHz). One possible cause of the observed dispersion can be a systematic effect in the estimation of the beam. The agreement with WMAP results is good, with a difference which does not exceed 0.5%

The analysis gives continuity to my involvement in the Planck LFI Data Processing Center (DPC) activities, and in general in the Planck mission, started during my MSc thesis [1]. This work, which contributed to Planck/LFI calibration activities and is reported in the Planck 2015 LFI Calibration Paper, concluded at the beginning of my second year of Ph.D. Since the Planck mission was at its conclusion as foreseen, I migrated to the Euclid mission which is still in its pre launch phases. The second part of my Ph.D. is aimed at developing a prototype of an End-to-End Simulator for the Euclid Mission.

The Euclid Mission has been selected as test case for the design and implementation of a reference architecture of an E2ES aimed at supporting instrument operations. Euclid is a medium class mission of the European Space Agency (ESA), aimed at investigating the distance-redshift relationship and the evolution of cosmic structures by means of two instruments: the Visual Imager (VIS) and the Near-Infrared Spectrometer and Photometer (NISP). The prototype simulates the Euclid/NISP instrument and uses the redshift measurement as reference scientific parameter. The structure of the simulator is modular, so that the different components of the simulator remain unaffected by required improvements or changes in one of the modules. Each module is designed to simulate a particular aspect of the measurement, from the definition of the pointing strategy to the extraction of the interesting parameter, passing through optics, detection chain and data processing pipeline simplified simulations. At the end of the simulation chain a cross-check between input and output results is performed in order to assess the correct functioning of the whole E2ES chain and the fulfilment of the mission requirements.

Two different versions of the proto-E2ES have been implemented: a preliminary version, delivered to ESA as one of the final products of the work supported by contract IPL-PTE/GLC/al/241.2014 and a more mature version, aimed at closing a major software issue and thought to be compliant with the software framework designed for Euclid.

The simulator is able to correctly simulate the spectral extraction and the correct redshift is always measured for each source of the selected test catalog. Even

with its basic functionalities, the prototype allows us to perform a sensitivity analysis on the pointing parameters and represents a useful tool in order to understand where open points are still present and to test, in a simplified way, possible solutions.

Appendix A

Redshift

Because of the expansion of the Universe, a photon emitted at a certain time t_e with a wavelength λ_e is received by an observer at a time t_0 with a wavelength λ_0. This phenomena is called *cosmological redshift* and it is defined as follows:

$$z \equiv \frac{\lambda_0}{\lambda_e} - 1 \tag{A.1}$$

Because the "dilatation" suffered by the wavelength is the same of the scale factor $a(t)$:

$$\frac{\lambda_0}{\lambda_e} = \frac{a(t_0)}{a(t_e)} \tag{A.2}$$

we can write:

$$z = \frac{a(t_0)}{a(t_e)} - 1 \tag{A.3}$$

From equation A.3 we can see that:

$$\begin{aligned} a(t_0) > a(t_e) \Rightarrow z > 1 \Rightarrow \lambda_0 > \lambda_e \\ a(t_0) < a(t_e) \Rightarrow z < 1 \Rightarrow \lambda_0 < \lambda_e \end{aligned} \tag{A.4}$$

so the change in wavelength is due to the difference in the scale factor at the two considered time and not to the relative motion of the source respect to the observer, *i.e.* cosmological redshift is not a simple Doppler effect. To understand that we can consider the example shown in figure A.1. Source and observer are at rest one respect to the other when the photon is emitted and received: there

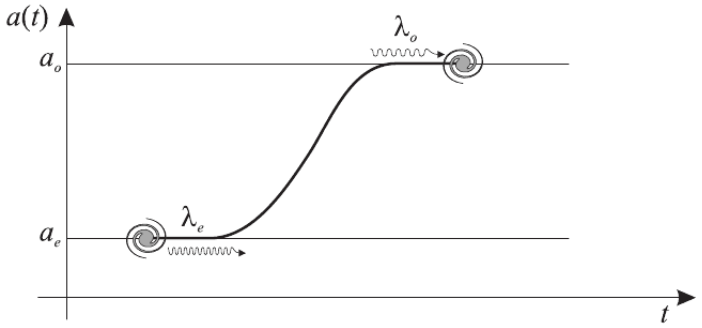

Figure A.1: To understand that redshift and Doppler effect are different concepts we can consider a model in which a photon is emitted when $a(t_e) = a_e = cost$, then an expansion from a_e to a_0 occurs and the photon is received at $a(t_0) = a_0 = cost$.
Source: Mezzetti, A.A. 2011-2012 [49].

is no Doppler effect, but $a(t_e) \neq a(t_0)$, which means that there is cosmological redshift.

From equation A.4 we can infer that redshift z can be used to measure time. Because the Universe expands, $a(t_0) > a(t_e)$ means that $t_e < t_0$, so the photon was emitted in the past respect to the observer. This means that the higher is z, the older is the object we are observing. This reasoning is quantitatively expressed by the expression:

$$t(z) = \int_0^z \frac{dz'}{(1+z')H(z')} \tag{A.5}$$

where the function:

$$H(z) = H_0(1+z)\sqrt{\Omega_r(1+z)^2 + \Omega_m(1+z) + \Omega_\Lambda(1+z)^{-2} + 1 - \Omega} \tag{A.6}$$

takes into account the particular cosmological model. From $t(z)$ we can also define the *lookback time* t_{lb}, the difference between the age t_0 of the Universe now (at observation) and the age $t(z)$ of the Universe at redshift z:

$$t_{lb} = t_0 - t(z) \tag{A.7}$$

The lookback time represent the age of the Universe at the time the photons were emitted.

Appendix B

Acronyms

ΛCDM	Lambda-Cold Dark Matter
AOCS	Attitude Orbit Control System
BA	Band Average
BAO	Baryonic Acoustic Oscillation
CC	Color Correction
CDM	Cold Dark Matter
CMB	Cosmic Microwave Background
DE	Dark Energy
DM	Dark Matter
DPC	Data Processing & Calibration
DS	Detection System
DS	Deep Survey
E2ES	End-to-End Simulator
ECSS	Euclid Survey Strategy
EE	Encircled Energy
EO	Earth Observatory
ESA	European Space Agency
ESTEC	European Space Research and Technology Centre
FoV	Field of View
FWHM	Full Width Half Maximum

GR	General Relativity
HFI	High Frequency Instrument
HIFI	Heterodyne Instrument for the Far Infrared
HST	Hubble Space Telescope
IAS	Institut d'Astrophysique Spatiale
IASF	Istituto Nazionale di Astrofisica e Fisica cosmica
IDP	Interplanetary Dust Particle
INAF	Istituto Nazionale di AstroFisica
I/O	Input/Output
IOT	Instrument Operation Team
IR	Infra-Red
IRAF	Image Reduction and Analysis Facility
IRAS	Infra-Red Astronomical Satellite
LFI	Low Frequency Instrument
LHC	Large Hadron Collider
NASA	National Aeronautics and Space Administration
NI-CU	Calibation Unit
NI-DPU	Data Processing Unit
NI-DS	Detection System Assembly
NI-FWA	Filter Wheel Assembly
NI-GWA	Grism Wheel Assembly
NI-ICU	Instrumental Control Unit
NI-OMA	Opto-Mechanical Assembly
NI-SCS	Sensor Chip System
NI-WE	Warm Electronic Assembly
NIR	Near Infra-Red
NISP	Near Infra-Red Spectrometer and Photometer
OBDG	On-Board Data Generation
OD	Operative Day
OM	Optical Model

OU	Operational Unit
PA	Performance Assessment
PACS	Photoconductor Array Camera and Spectometer
PSB	Polarization Sensitive Bolometer
PSF	Point Spread Function
R2R	Radiometer-to-Radiometer
ROE	Read-Out Electronics
RPSU	Read-Out Power Supply Units
SAA	Solar Aspect Angle
S/C	Spacecraft
SCE	Spacecraft & Environment
SED	Spectral Energy Distribution
SOC	Survey Optimization Code
SS	Solar System
SWB	Spider-Web Bolometer
TF	Transfer Function
TIPS	This Is a Pixel Simulator
VI-CDPU	Control & Data Processing Unit
VI-CU	Calibration Unit
VI-FPA	Focal Plane Assembly
VI-PMCU	Power & Mechanism Control Unit
VI-RSU	Shutter
VIS	VISual Imager
WL	Weak Lensing
WMAP	Wilkinson Microwave Anisotropy Probe
WS	Wide Survey
ZEUS	Zody Euclid Simulator
ZL	Zodiacal Light

Bibliography

[1] Romelli E. *Interplanetary Dust Particles (IDPs) dynamics for the Planck mission* MSc thesis, supervisor: Gregorio A., tutor: Maris M., A.Y. 2012/2013

[2] Planck Collaboration. *Planck 2015 results. I. Overview of products and scientific results.* Astronomy & Astrophysics, 594 A1, arXiv:astro-ph/1502.01582

[3] Coles P. and Lucchin F. *Cosmology - Origin and Evolution of Cosmic Structure.* Wiley, 2002

[4] Mo H., van den Bosh F. and White S. *Galaxies Formation and Evolution.* Cambridge University Press, 2010

[5] Bambi C. and Dolgov A.D. *Introduction to Particle Cosmology - The Standard Model of Cosmology and its Open Problems.* Springer, 2016

[6] Fixen D.J. *The Temperature of the Cosmic Microwave Background.* Ap.J., **707**(2): 916-920, 2009

[7] Mather *et al. Calibrator Design for the COBE Far-Infrared Absolute Spectrophotometer (FIRAS).* Ap.J., **512**: 511-520, 1999

[8] Corbelli E. and Salucci P. *The Extended Rotation Curve and the DM Halo of M33.* Monthly Noticec of the R.A.S. **311** (2): 441-447, arXiv:astro-ph/9909252

[9] Euclid Red Book Editorial Team. *Euclid Definition Study Report - revision 1.* January 2011

[10] Perlmutter S. *Supernovae, Dark Energy and the Accelerating Universe.* Physics Today, **56**, n° 4, 53, 2003

[11] Salopek D.S. and Bond J.R. *Non-linear Evolution of Long-wavelength Metric Fluctuation in Inflationary Models.* Phys. Rev. D, **42**, 3936, december 1990

[12] Wambsganss J. *Gravitational Lensing in Astronomy.* Living Reviews in Relativity, 1998

[13] Schneider P. *A New Formulation of Gravitational Lens Theory, Time Delay and Fermat Principle.* Astronomy & Astrophysics, **143**, 413-420, 1985

[14] Tyson J.A., Valdes F. and Wenk R.A. *Detection of Systematics Gravitational Lens Image allignments: Mapping Dark Matter in Galaxy Clusters.* Ap.J., **349**, L1-L4, 1990

[15] Kaiser N. and Squires G. *Mapping Dark Matter with Weak Gravitational Lensing.* Ap.J., **404**, 441-450, 1993

[16] Eisestein D.J., Seo H.-J. and White M. *On the Robustness of the Acoustic Low-Redshift Clustering of Matter.* Ap.J., **664**, 660-674

[17] Eisestein D.J. and White M. *Theoretical Uncertainty in Baryon Oscillation* Phys. Rev. D, **70**, 2004

[18] Planck Collaboration *Planck Explanatory Supplement.* v1.03, April 2013

[19] Bluebook-ESA-SCI *Planck-The Scientific Program.* ESA, 2005

[20] Bersanelli M. et al. *Planck pre-launch status: Design and description of the Low Frequency Instrument* Astronomy & Astrophysics, **520**, 2010

[21] Planck Collaboration. *Planck 2015 results. IX. Diffuse components separation: CMB maps.* Astronomy & Astrophysics, 594 A9, arXiv:astro-ph/1502.05956

[22] Planck Collaboration. *Planck 2015 results. X. Diffuse components separation: Foreground maps.* Astronomy & Astrophysics, 594 A10, arXiv:astro-ph/1502.01588

[23] Planck Collaboration. *Planck 2015 results. VIII. High Frequency Instrument data processing: Calibration and maps* Astronomy & Astrophysics, 594 A8, arXiv:astro-ph/1502.01587

[24] Planck Collaboration. *Planck 2015 results. V. LFI calibration.* Astronomy & Astrophysics, 594 A5, arXiv:astro-ph/1505.08022

[25] Cropper M. et al. *VIS: the Visible Imager for Euclid* August 2014, http://arxiv.org/pdf/1208.3369

[26] Maciaszek T. et al. *Euclid Near Infrared Spectro Photometer instrument concept and first test results at the end of phase B* SPIE 2014, https://www.duo.uio.no/

[27] Planck Collaboration. *Planck 2015 results. II. Low Frequency Instrument data processing.* Astronomy & Astrophysics, 594 A2, arXiv:astro-ph/1502.01583

[28] Weiland J. L. et al. *Seven-Year Wilkinson Microwave Anysotropy Probe (WMAP) Observations: Planets and Celestial Calibration Sources* December 2010, arxiv.org/abs/1001.4731v2

[29] Cremonese G. et al. *Asteroid detection at millimetric wavelengths with the PLANCK survey* New Astron. 7, 2002, 483-494, arXiv:astro-ph/0209373

[30] Planck Collaboration. *Planck 2015 results. IV. Low Frequency Instrument beams and window functions.* Astronomy & Astrophysics, 594 A4, arXiv:astro-ph/1502.01584

[31] Zacchei A. et al. *Planck early results. V. The Low Frequency Instrument data processing* Astronomy & Astrophysics, 536, A5, 1-19, (2011)

[32] Hinshaw G. et al. *Five-Year Wilkinson Microwave Anisotropy Probe (WMAP) Observations: Data Processing, Sky Maps, and Basic Results* Ap.J. Supplement 180, 2009, 225-245, arXiv.org/abs/0803.0732

[33] Planck Collaboration. *Planck 2013 results. V. LFI calibration.* Astronomy & Astrophysics, 571, A5, 1-29, (2014)

[34] Battaglia P. and Romelli E. *EUCLID E2E ANALYSES AND TRADE-OFFS* issue 1.0, November 2014,C.I.F.S. - Consorzio Interuniversitario per la Fisica Spaziale.

[35] ARCHEO-E2E Teams *GMV-ARCHEO-E2E-FR-001 Final Report* issue 1.1, February 2013.

[36] Battaglia P. and Romelli E. *EUCLID E2E DESIGN DEFINITION* issue 1.4, October 2015,C.I.F.S. - Consorzio Interuniversitario per la Fisica Spaziale.

[37] Battaglia P. and Romelli E. *EUCLID E2E REQUIREMENTS BASELINE* issue 1.6, October 2015,C.I.F.S. - Consorzio Interuniversitario per la Fisica Spaziale.

[38] Gregorio A. et al. *A dedicated End-to-End Simulator for Euclid Instrument Operations* SpaceOps 2016 Conference, 2016, 10.2514/6.2016-2567, arc.aiaa.org

[39] Romelli E. *proto-E2ES v1.0 User Manual* issue 1.1, September 2015.

[40] Battaglia P. and Romelli E. *EUCLID E2E VERIFICATION AND VALIDATION PLAN* issue 1.1, October 2015,C.I.F.S. - Consorzio Interuniversitario per la Fisica Spaziale.

[41] Euclid Consortium *Euclid Science Requirements Document* issue 7.0, ESA, Jenuary 2013

[42] Romelli E. *proto-E2ES v2.0 User Manual* issue 1.0, February 2016.

[43] Euclid Project Team *Euclid System Requirements Document* Issue 1, rev. 1, October 2013

[44] Gross A. et al. *ETC-42 Exposure Time Calculator: Evolution and New Functionalities* ADASS XXIV ,ASP Conference Series, Vol. 495

[45] Kellsall T. et al. *The COBE Diffuse Infrared Background Experiment Search for the Cosmic Infrared Background: II. Model of the Interplanetary Dust Cloud* Ap.J., **508**, 44-73, 1998

[46] Maris M. et al. *Modelling of Zodiacal Light Emission for Space Missions* ADASS XXVI, 2016, poster proceedings

[47] Rest A. et al. *Residual images in charged-coupled device detectors* Review Of Scientific Instruments,ASP Conference Series, Vol. 73, 5, May 2002

[48] Gregorio A. *EUCLID E2E ROADMAP* issue 1.1, October 2015,C.I.F.S. - Consorzio Interuniversitario per la Fisica Spaziale.

[49] Mezzetti M. *Appunti del corso di Cosmologia 1 - University of Trieste.* Academic Year: 2011-2012

Aknowledgements

This song is ending, but the story never ends.

The End of Time

Poco più di otto anni fa varcavo, per la prima volta, la soglia del Dipartimento di Fisica. Non ero pronto, ma ho cominciato comunque a camminare. Oggi, alla fine di quel cammino, smetto di essere uno studente, almeno formalmente. Per la terza volta, mi ritrovo a guardarmi alle spalle e mi godo uno dei momenti che mi piacciono di più: i ringraziamenti.

Mi sia concesso di fare uno strappo all'etichetta e di ringraziare per prima la mia compagna Cristina. Solo io e lei sappiamo davvero la deriva da cui mi ha strappato e gli equilibri che con amore e pazienza ha ricostruito. Non basteranno queste poche righe ad esprimerle la mia gratitudine e quello che provo, ma spero di riuscirci sempre nelle piccole cose di tutti i giorni e nei periodi positivi e negativi della nostra convivenza. Un granchio cerca il suo scoglio per ripararsi, ma anche lo scoglio ha bisogno del suo granchio.

Tre anni dopo la mia laurea magistrale, mi ritrovo a ringraziare la mia supervisor Anna Gregorio e il mio tutor Michele Maris, con cui in questi anni ho instaurato un rapporto di amicizia oltre che lavorativo. Scadrò nel banale, ma se ho imparato qualcosa in questi anni, lo devo anche alla loro guida e alla loro pazienza.

Sono convinto da sempre che la prima squadra in cui si gioca sia la famiglia. La mia è una squadra piccola ma affiatata, che nelle vittorie e nelle sconfitte è sempre rimasta unita. Anche se a volte non lo dimostro a pieno, non smetterò mai di ringraziare mamma Alba ("Se diventi famoso, per prima la mamma!", giusto?!), papà Sandro e mio fratello Georgy. In una semplice parola: grazie!

Un sacco di persone sono passate dalla mia vita in questi tre anni. Alcune ci sono entrate per restare, alcune sono tornate, altre si sono allontanate senza perdere i contatti, altre si sono allontanate e basta. Colgo l'occasione per ringraziarle tutte, a partire dai colleghi, che sono prima di tutto "compagni di merende", passando per Science Industries, la WP Trieste e tutti gli altri personaggi che hanno arricchito questa storia.

Voglio dedicare una menzione speciale a quel Bonetta, che un bel giorno di fine estate ha presentato a una persa Cristina un persissimo Erik. Resto dell'idea che facesse tutto parte di un tuo piano malvagio, ma non ti ringrazierò mai abbastanza del bel regalo.

Per finire, voglio dedicare questo lavoro al me stesso bambino. Lui non avrebbe mai mollato inseguendo la sua strada. A volte, lungo il percorso, me ne sono dimenticato. Per nostra fortune, nei momenti più bui, lui mi ha ricordato dove volevamo andare. Piccolo Erik: da oggi ci chiamano "Dottore" ed è anche merito tuo.